Technical Physics Letters, Vol. 28, No. 6, 2002, pp. 445–447. Translated from Pis'ma v Zhurnal Tekhnicheskoĭ Fiziki, Vol. 28, No. 11, 2002, pp. 1–7.
Original Russian Text Copyright © 2002 by Gitlin, Zelenogorsky, Perminov.

Microwave Beam Imaging by Recombination Continuum from the Positive Column of Gas Discharge in a Cesium Vapor–Xenon Mixture

M. S. Gitlin, V. V. Zelenogorsky, and A. O. Perminov
Institute of Applied Physics, Russian Academy of Sciences, Nizhni Novgorod, Russia
e-mail: gitlin@appl.sci-nnov.ru

Received January 14, 2002

Abstract—A new sensitive method for imaging of the spatial distribution of microwave intensity is proposed. The method is based on the imaging of the 6*P*-recombination continuum of cesium, emitted from a nonequilibrium plasma of the positive column of gas discharge in a cesium vapor–xenon mixture. It is demonstrated that the spatial distribution of intensity of 35-GHz microwave radiation measured by this method in a focal plane of a lens well coincides with the pattern obtained with the aid of a movable microwave detector. The time resolution of the proposed microwave imaging system reaches 1 ms. © *2002 MAIK "Nauka/Interperiodica".*

For solving problems encountered in the development of microwave sources and transmission lines, microwave nondestructive imaging in opaque media, etc., it is necessary to determine the spatial distribution of microwave intensity [1, 2]. Methods widely used at present for investigation of the spatial structure of microwave fields are based on the thermal microwave action upon various materials such as films with special phosphors, liquid-crystalline or impregnated paper screens, etc. [1–4]. Examination of the pattern of screen heating by means of an IR imager or by measuring changes in the light emission or absorption allows the spatial structure of a microwave field to be imaged.

The main disadvantages significantly restricting possible applications of the thermal methods of investigation of the spatial structure of microwave fields are slow response (with a characteristic time in most cases not smaller than 0.1 s) and low sensitivity (with the energy flux threshold about 10^{-2} J/cm^2 for most versatile techniques). Because of the low sensitivity, the thermal detection methods cannot be used, for example, to study the spatial structure of radiation from low-power and pulsed microwave generators such as magnetrons, gyroklystrons, and relativistic microwave sources.

This study is devoted to the development of methods for imaging of the microwave beams with the aid of the 6*P*-recombination continuum of cesium (6*P*-RCC) [5–7] emitted from a layer of nonequilibrium plasma in the positive column of gas discharge in a cesium vapor–xenon mixture (Cs–Xe discharge) [8]. We believe that this imaging technique can be used to create an imager of millimetric and centimetric waves combining high sensitivity and good time resolution. Emission in the 6*P*-RCC falls within a convenient blue region of the visible spectrum (corresponding to wavelengths below 504 nm), possesses sufficiently large luminosity, and is not distorted by reabsorption effects [5–7]. The intensity of continuum is directly proportional to the densities of electrons and cesium ions which are extremely sensitive to changes in the electron temperatures under the action of microwave radiation. In addition to being the source of recombinant radiation, cesium plays an important role in the formation of charged particles in nonequilibrium plasma of the positive column of the Cs–Xe discharge [5, 6, 9], where the inert gas acts as a buffer medium.

We have studied the possibility of using 6*P*-RCC for imaging of the microwave beams on a setup schematically depicted in Fig. 1. A planar layer of nonequilibrium plasma in the positive column of the Cs–Xe discharge was created in a special discharge tube (DT). The middle part of the DT accommodated a rectangular parallelepiped glued from quartz plates. Two parallel flat quartz windows *1* with a 10 × 10 cm square aperture and a spacing of 2 cm allowed a microwave beam to be introduced in and extracted from the DT without distortions. Two flat rectangular anodes *2* and two heated cathodes *3* were arranged inside glass cylinders (*4* and *5*) with a diameter of 10 cm, which were glued to opposite edges of the quartz cell. The anodes and cathodes were spaced by 30 cm. Each pair of electrodes was connected to a separate source of electric current. The discharge tube was provided with side fingers containing cesium droplets. For creating a required cesium vapor pressure, the DT was placed into thermostat *6* and heated to 80–110°C by blowing with hot air. The tube was filled with xenon at a pressure of 45 Torr. This relatively high gas pressure is necessary to provide for a local character of the additional heating of plasma electrons under the action of microwave radiation. The lon-

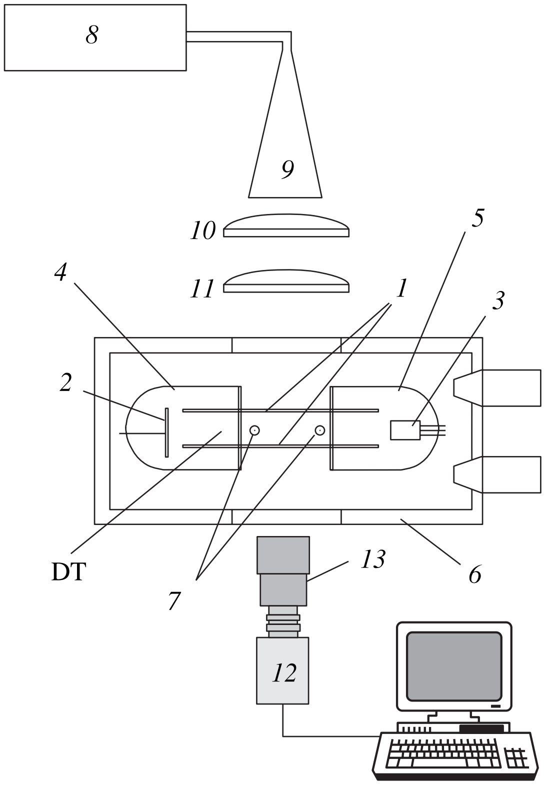

Fig. 1. A schematic diagram of the experimental setup (see the text for explanations).

gitudinal electric field strength E in the positive column was determined by measuring a potential difference between electric probes *7*. The electron temperature in the positive column of the Cs–Xe discharge was determined from the 6P-RCC spectrum [5–8].

Investigations of microwave action upon the positive column of the Cs–Xe discharge plasma were performed at a current of 1.5 A and a DT temperature of 368 ± 2 K. Under these conditions, the positive column of the Cs–Xe discharge represents a flat homogeneous plasma layer occupying the whole working aperture of the tube [8]. In the absence of microwave radiation, the positive column was characterized by a longitudinal electric field strength of $E_0 = 0.9$ V/cm, an electron temperature of $T_{e0} = 0.42$ eV, and an electron density of $N_{e0} = 4 \times 10^{12}$ cm^{-3}. Microwave radiation with a frequency of 35 GHz was generated by magnetron *8* (Fig. 1) with a maximum output power in the pulsed mode of about 20 W (for a pulse duration of 0.1 s). The radiation was emitted from a horn antenna *9* and focused by spherical teflon lenses *10* and *11* (with a diameter of 20 cm and a focal length of 60 cm) into the center of the positive column of the Cs–Xe discharge.

Dependence of the 6P-continuum emission intensity I on the microwave intensity W incident upon the discharge plasma was studied with the aid of a photomultiplier equipped with a set of input interference optical filters transmitting only 6P-RCC.[1] The results of these measurements showed that a change in the 6P-RCC intensity $\Delta I = I - I_0$ (I_0 is the intensity of 6P-RCC emission in the absence of microwave radiation) was proportional to the incident microwave intensity in the range from 0 to 5 W/cm^2. A greater incident microwave power led to breakdown of the plasma layer.

The spatial distribution of the 6P-RCC intensity was studied using a monochrome KS-381 CCD camera *12* (Fig. 1) with an SE-1212 lens. The aforementioned set of filters *13* (see footnote 1) was placed in front of the lens. The output signal from the CCD camera was fed to a FlyVideo EZ98 framgrabber installed in a computer. The spatial distribution of the microwave intensity was restored from the image of the spatial distribution of the microwave-induced 6P-RCC intensity $I(x, y)$ upon subtraction of the background distribution $I_0(x, y)$ of the intensity of 6P-RCC emission from the positive column of the Cs–Xe discharge measured during a frame preceding to the microwave pulse front (here, x and y are the longitudinal and transverse coordinates relative to the discharge current direction).

In order to verify the proposed imaging technique, we have compared the spatial distribution of the microwave intensity $W(x, y)$ in the focal plane of lens *11*, measured with the aid of a movable calibrated microwave diode, to the pattern of spatial variations of the 6P-RCC intensity $\Delta I(x, y)$ measured using the CCD camera as described above. The curves of the relative intensity $W/W(0, 0)$ of the microwave beam (thick solid curves) and the relative variation of the 6P-RCC intensity $\Delta I/\Delta I(0, 0)$ (thin solid curves) measured along the coordinates x and y are presented in Figs. 2a and 2b, respectively. These profiles were measured using the microwave intensity at the beam center $W(0, 0) \approx 3$ W/cm^2, for which the relative variation of the continuum emission intensity was $\Delta I(0, 0)/I_0 \approx 1$. As can be seen from Fig. 2, the distributions measured by the two methods coincide to within the experimental error everywhere except for the beam periphery. Elucidation of the reasons for discrepancy between the results of measurements in the peripheral region requires additional investigation.

The characteristic time of variation of the 6P-RCC intensity upon fast switch-on of the microwave source, which was measured by the photomultiplier response, coincided with the electron heating time and amounted to a several microseconds. Thus, the time resolution of the method proposed for imaging of the microwave beams can be on the order of ten microseconds, while the energy flux sensitivity threshold can be as low as

---

[1] The set of filters ensured a transmission of 40 ± 10% in a wavelength range from 400 to 500 nm and below 0.1% outside the 390–510 nm interval. In addition, the transmission was below 0.1% in the 450–460 nm interval containing lines of the second resonance transition ($7P_{3/2} \longrightarrow 6S_{1/2}$, $7P_{1/2} \longrightarrow 6S_{1/2}$) in Cs atoms [5].

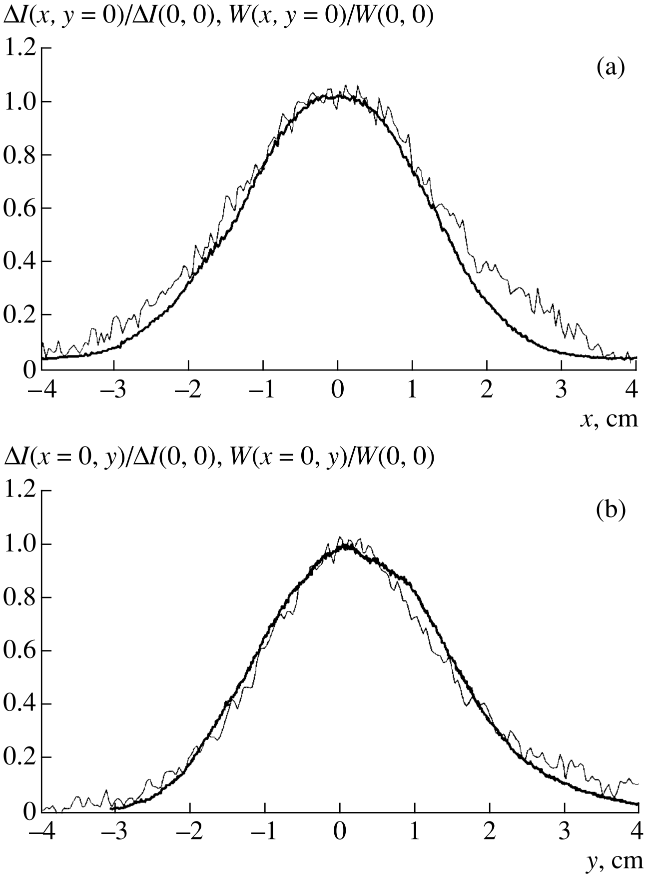

Fig. 2. The profiles of the relative intensity $W/W(0, 0)$ of the microwave beam (thick solid curves) and the relative variation of the $6P$-RCC intensity $\Delta I/\Delta I(0, 0)$ (thin solid curves) measured in the (a) longitudinal (x) and (b) transverse (y) directions relative to the discharge current direction.

10^{-5} J/cm^2. Under the conditions of our experiments, the time resolution was limited by the sensitivity of the KS-381 CCD camera. At a fully opened diaphragm and maximum gain, the minimum duration of exposure that allowed the $6P$-RCC emission to be measured was 1 ms, while the energy flux sensitivity threshold was about 10^{-3} J/cm^2.

Acknowledgments. The authors are grateful to S.V. Golubev, A.G. Litvak, and V.E. Semenov for their interest in this study.

This study was partly supported by the Russian Foundation for Basic Research, project no. 00-02-17757.

REFERENCES

1. S. O. Kuznetsov and V. I. Malygin, Int. J. Infrared Millim. Waves **12** (11), 1241 (1991).
2. J.-C. Bolomey, IEEE Trans. Microwave Theory Tech. **37** (12), 2109 (1989).
3. Yu. P. Timofeev and S. A. Fridman, Izv. Akad. Nauk SSSR, Ser. Fiz. **43** (6), 1303 (1979).
4. M. Pereyaslavets, T. Idehara, I. Ogawa, *et al.*, Int. J. Infrared Millim. Waves **20** (6), 1195 (1999).
5. L. Agnew and W. H. Reichelt, J. Appl. Phys. **39** (7), 3149 (1968).
6. *Thermionic Converters and Low Temperature Plasma*, Ed. by B. Ya. Moĭzhes and G. E. Pikus (Nauka, Moscow, 1973).
7. J. M. Wetzer, Physica C (Amsterdam) **123**, 247 (1984).
8. N. A. Bogatov, M. S. Gitlin, D. A. Dikan, *et al.*, Phys. Rev. Lett. **79** (15), 2819 (1997).
9. L. M. Biberman, V. S. Vorob’ev, and I. T. Yakubov, *Kinetics of Nonequilibrium Low-Temperature Plasmas* (Nauka, Moscow, 1982; Consultants Bureau, New York, 1987).

Translated by P. Pozdeev

Technical Physics Letters, Vol. 28, No. 6, 2002, pp. 448–449. Translated from Pis'ma v Zhurnal Tekhnicheskoĭ Fiziki, Vol. 28, No. 11, 2002, pp. 8–10.
Original Russian Text Copyright © 2002 by Trigub, Plotnov.

A Change in the Structure of an Ultrasonically Processed MMA–MAA Based Photoresist

V. I. Trigub and A. V. Plotnov
Nizhni Novgorod State Technical University, Nizhni Novgorod, Russia

Received November 20, 2001

Abstract—The structure of a photoresist based on a MMA–MAA copolymer was modified by exposure to an ultrasound with a frequency of 21 kHz and a power density of 300 W/m^2. The results of the UV and IR spectroscopic measurements show that the ultrasonic processing leads to the formation of C=O double bonds and to the growth of absorption in the 260–360 nm wavelength range. *© 2002 MAIK “Nauka/Interperiodica”.*

The development of microelectronics led to the need for a lithographic process ensuring increased lateral resolution, which can be provided by using UV radiation with a shorter wavelength (260–360 nm) as compared to that employed in the conventional process (350–420 nm [1]). For realization of the new lithographic process, it is also necessary to create photoresists possessing increased sensitivity with respect to the UV radiation employed, which would provide for a sufficiently high efficiency of the exposure stage. As is known, methyl methacrylate–methacrylic acid (MMA–MAA) copolymers are highly sensitive to UV radiation in the 260–360 nm range, which is due to the presence of C=O carboxy groups [2].

The purpose of this study was to investigate the possibility of carbon–oxide double bond formation in an MMA–MAA copolymer photoresist under the action of ultrasound in air. The C=O bonds account for the absorption of electromagnetic radiation in the UV spectral range from 260 to 360 nm [2]. Below we report on the results of modification of a MMA–MAA copolymer by exposure to ultrasound with a frequency of 21 kHz. The ultrasound was generated by a GZ-33 oscillator and radiated by a magnetostrictive vibrator. The power supplied to the vibrator was 1.2 W. The samples of resist were deposited by dropping a copolymer onto the surface of a sapphire or silicon (KDB-4 grade) substrates. After a 15-min ultrasonic processing, the copolymer was spread over the substrate surface by centrifuging at 2500 rpm. Then the resist films were heat-treated in a convective furnace at 160°C for 30 min [3]. The intensity of the ultrasonic irradiation of the resist samples was estimated at 300 W/m^2.

Changes in the structure of the ultrasound-modified polymer resist were revealed by measuring the UV and IR transmission spectra of the film samples. The spectra were recorded on an IKS-22 double-beam spectrometer (Russia) in the wavenumber range from 1900 to 700 cm^{-1} and on an SF-26 spectrophotometer in the wavelength range from 200 to 400 nm. The film thickness was ~1 μm ± 15 nm as determined with the aid of a MII-4 microinterferometer (Russia). Typical UV and IR transmission spectra are presented in Figs. 1 and 2, respectively. The effect of processing was determined by comparing the spectra recorded before and after exposure of a sample to the ultrasound.

The structure-related changes in the optical properties of MMA–MAA copolymer films were observed in the IR range (Fig. 2) containing absorption bands corresponding to the vibrations of C=O and C–O bonds. As can be seen from the IR transmission spectra, the modified film is characterized by a an increase in the optical absorption in the region of 1700 cm^{-1}, which is probably indicative of the increasing content of C=O groups in the ultrasound-processed copolymer [4]. Indeed, the IR absorption in the region of 1700 cm^{-1} is attributed to the vibrations of carbonyl groups C=O [5].

In addition, the spectra presented in Fig. 1 show evidence that the exposure to ultrasound led to an increase in sensitivity of the MMA–MAA resist in the wavelength range from 260–360 nm, which can be also related to the formation of C=O bonds.

Thus, ultrasonic processing of an MMA–MAA copolymer resist at a frequency of 21 kHz and a power

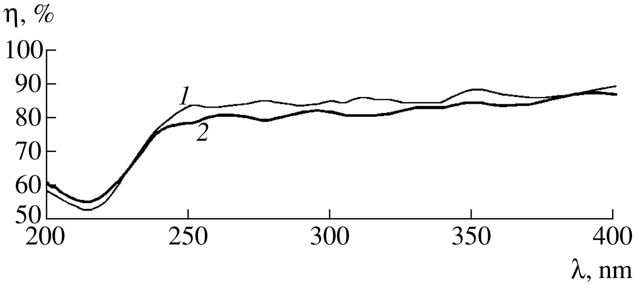

Fig. 1. The UV transmission spectra of a MMA–MAA copolymer film measured (*1*) before and (*2*) after ultrasonic processing.

1063-7850/02/2806-0448$22.00 © 2002 MAIK “Nauka/Interperiodica”

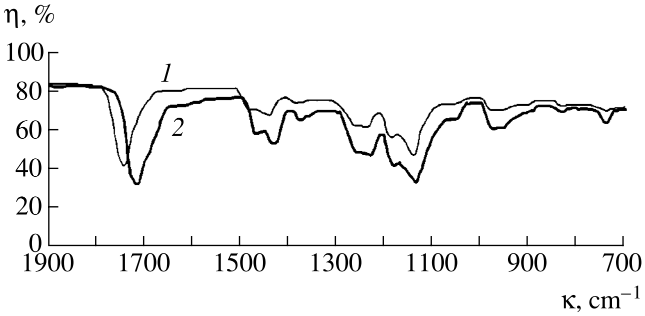

Fig. 2. The IR transmission spectra of a MMA–MAA copolymer film measured (*1*) before and (*2*) after ultrasonic processing.

density of 300 W/m^2 in air leads to oxidation of the polymer, which results in increasing sensitivity to UV radiation in the 260–360 nm wavelength range.

REFERENCES

1. Y. Tarui, *VLSI Technology: Fundamentals and Applications* (Springer-Verlag, Berlin, 1986; Radio i Svyaz’, Moscow, 1985).
2. A. Ya. Vaĭner, A. N. Yakimenko, V. F. Limanov, *et al.*, Mikroélektronika **13** (4), 311 (1984).
3. W. M. Moreau, *Semiconductor Lithography: Principles, Practices, and Materials* (Plenum, New York, 1988; Mir, Moscow, 1990), Part 1.
4. L. I. Tarutina and F. O. Pozdnyakova, *Spectrum Analysis of Polymers* (Khimiya, Leningrad, 1986).
5. F. F. Komarov, A. V. Leont’ev, and A. P. Novikov, Mikroélektronika **18** (3), 212 (1989).

Translated by P. Pozdeev

Technical Physics Letters, Vol. 28, No. 6, 2002, pp. 450–453. Translated from Pis'ma v Zhurnal Tekhnicheskoĭ Fiziki, Vol. 28, No. 11, 2002, pp. 11–20.

On the Increase in the Charge Carrier Mobility in Fullerene-Containing Conjugated Organic Systems

M. M. Mikhailova[a], **M. M. Kosyreva**[b], **and N. V. Kamanina**[c,*]

[a] *St. Petersburg State Technical University, St. Petersburg, Russia*
[b] *St. Petersburg State Electrotechnical University, St. Petersburg, Russia*
[c] *Vavilov Optical Institute, State Scientific Center of the Russian Federation, St. Petersburg, 190164 Russia*
** e-mail: kamanin@ffm.ioffe.rssi.ru (Dr. Natalie V. Kamanina)*

Received December 4, 2001

Abstract—The effect of fullerenes C_{60} and C_{70} on the mobility of charge carriers in conjugated organic systems are studied. It was established that the carrier mobility in photoconducting fullerene-containing polyimide films exhibits a tenfold increase as compared to fullerene-free polymer films. A correlation between fullerene-induced changes in the spectral and photoconducting properties of these films is considered. *© 2002 MAIK "Nauka/Interperiodica".*

Photosensitive media based on conjugated organic structures occupy an important place in a broad class of light-controlled systems used in devices for data recording, storage, and processing—electrically and optically controlled spatiotemporal light modulators, including those based on liquid crystals. Advantages of such organic photoconducting layers are good spatial resolution and high sensitivity [1].

Considerable attention of researchers engaged in this field is devoted to the use of heterocyclic polymers, in particular, polyimides (PIs). This is explained by the advantageous combination of photoelectric and physicochemical characteristics offered by these polymers. Unfortunately, PIs are characterized by a low mobility of charge carriers, which is manifested by certain features in the electric conductivity of PI-based structures and is one of the factors limiting the operation speed of PI-based liquid-crystalline spatiotemporal light modulators. Therefore, the study of processes making it possible to increase the mobility of charge carriers in such polymer media is important both for basic investigations of light-controlled optical structures and for practical applications in the optical data processing systems [2], where an effective increase of one characteristic must be provided without significantly impairing other characteristics: for example, an increase in the operation speed must be achieved with retaining high sensitivity and spatial resolution.

This study was devoted to determining the possibility of increasing the charge carrier mobility in polymer systems by introducing fullerenes in conjugated organic structures such as polyimide 6B (PI-6B) [3]. As a result, we established a correlation between changes in the photoconductivity and spectral characteristics of these photosensitive polymers modified (doped) by fullerenes C_{60} and C_{70}.

The experiments were performed with thin films prepared from 3–6.5% PI solutions in tetrachloroethane or chloroform by the method of centrifugal casting. The films were modified by adding fullerenes C_{60} and C_{70} with the concentrations varied from 0.1 to 2.5 wt % relative to the photosensitive polymer component. The film thicknesses were varied within 2–4 μm. Note that both polymer and fullerenes [4] are well soluble in tetrachloroethane, which provided for the obtaining of sufficiently homogeneous films possessing high stability under laser irradiation. The polymer films were cast onto glass substrates above preliminarily deposited transparent conducting layers; for the electric measurements, gold contacts were applied to the polymer films. The bias voltage applied to the photosensitive polymer layers was varied from 5 to 70 V. The current–voltage (*I*–*V*) characteristics were measured for the samples with various concentrations of fullerene additive under conditions of variable illumination intensity. The spectral dependence of the photoconductivity was measured in a range of wavelengths up to the near IR region. The absorption spectra were measured on a SPEX Model 1403 spectrometer.

The main experimental results are summarized in the table and in Figs. 1–4. Data in the table represent the experimentally measured *I*–*V* characteristics of plain and fullerene-modified PI films. Figure 1 shows a plot of increase in the charge carrier mobility (calculated from data of the *I*–*V* measurements) of a fullerene-containing thin PI-6B film (relative to the nonmodified sample) versus bias voltage in the dark (plot *1*) and under illumination with the light from an incandescent lamp (plot *2*). The PI sample was modified by introducing

0.2 wt % of fullerene C_{70}. The inset in Fig. 1 shows a relative increase in the photoconductivity σ versus fullerene concentration in the samples biased to 10 V and illuminated with pulses of a flash lamp with an energy of 36 J and a pulse duration of 0.5 ms.

It should be noted that, in studying the photoconductivity of conjugated organic structures, we concentrated mostly on the role of charge carrier mobility rather than on their concentration. This is explained by the following circumstances. As is known, the conductivity activation energy of some conjugated organic systems, including polyimides [1, 5], coincides with the mobility activation energy: plotted in a double logarithmic scale, the values of conductivity and mobility (measured at equal temperatures and electric field strengths) fit to the same straight line inclined at 45° relative to the coordinate axes. The constant slope of the $\log\sigma$ versus $\log\mu$ plot is indicative of the constant concentration of charge carriers, suggesting that a change in the conductivity σ with the temperature and field strength is completely determined by changes of the carrier mobility μ as a function of these parameters. Taking these considerations into account and using the results of measurements of the current–voltage characteristics of plain and fullerene-modified PI films, the charge carrier mobility can be qualitatively estimated using the Child–Langmuir current–voltage relationship by the formula [6]

$$\mu \approx 10^{13}\frac{Id^3}{\varepsilon V^2}. \tag{1}$$

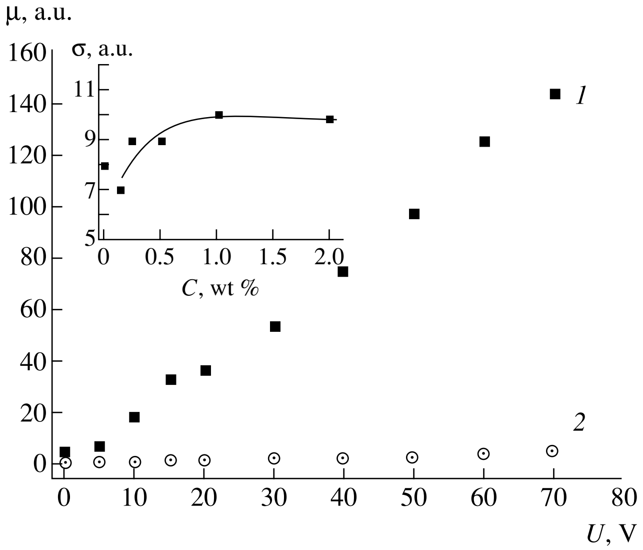

Fig. 1. The plot of increase in the charge carrier mobility of a thin PI-6B film containing 0.2 wt % of fullerene C_{70} (relative to the nonmodified samples) versus bias voltage measured (*1*) in the dark and (*2*) under illumination from an incandescent lamp. The inset shows a relative increase in the photoconductivity σ versus fullerene concentration in the samples biased to 10 V and illuminated with pulses of a flash lamp with an energy of 36 J and a pulse duration of 0.5 ms.

The results of calculations of the relative changes in the carrier mobility presented in Fig. 1 reveal a considerable (by almost one and a half orders of magnitude) increase in the mobility when the bias voltage increases from 0 to 70 V. As can be seen, the increase in mobility is much more significant in the dark than in the samples illuminated with light at a relatively low power. The increase in photoconductivity (and, following the above considerations, in the carrier mobility) with increasing

Current–voltage characteristics of the films of pure and fullerene-modified polyimide 6B

Bias voltage, V	Current, A			
	Pure PI		PI + 0.2 wt % C_{70}	
	dark	light	dark	light
0	5.00×10^{-14}	2.77×10^{-12}	2.50×10^{-13}	4.33×10^{-12}
5	2.40×10^{-13}	2.98×10^{-11}	1.80×10^{-12}	5.00×10^{-11}
10	3.97×10^{-13}	6.96×10^{-11}	7.6×10^{-12}	1.10×10^{-10}
15	5.05×10^{-13}	1.01×10^{-10}	1.70×10^{-11}	2.30×10^{-10}
20	6.65×10^{-13}	1.44×10^{-10}	2.50×10^{-11}	3.70×10^{-10}
30	9.72×10^{-13}	2.50×10^{-10}	5.30×10^{-11}	8.00×10^{-10}
40	1.19×10^{-12}	3.80×10^{-10}	9.00×10^{-11}	1.40×10^{-9}
50	1.53×10^{-12}	5.70×10^{-10}	1.50×10^{-10}	2.40×10^{-9}
60	1.70×10^{-12}	7.01×10^{-10}	2.15×10^{-10}	3.90×10^{-9}
70	2.00×10^{-12}	8.60×10^{-10}	2.90×10^{-10}	6.20×10^{-9}

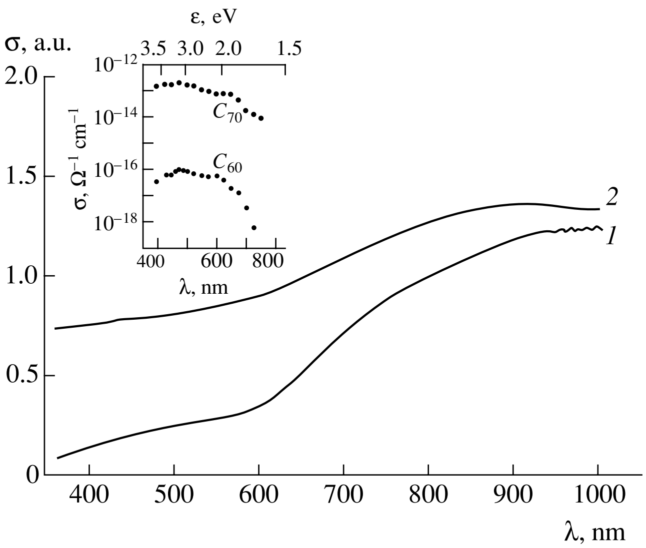

Fig. 2. The spectral dependences of photoconductivity of thin films of (*1*) pure PI-6B and (*2*) the same polymer modified with fullerene C_{70}. The inset shows the spectra of photoconductivity of the films of pure fullerenes C_{60} and C_{70} [11].

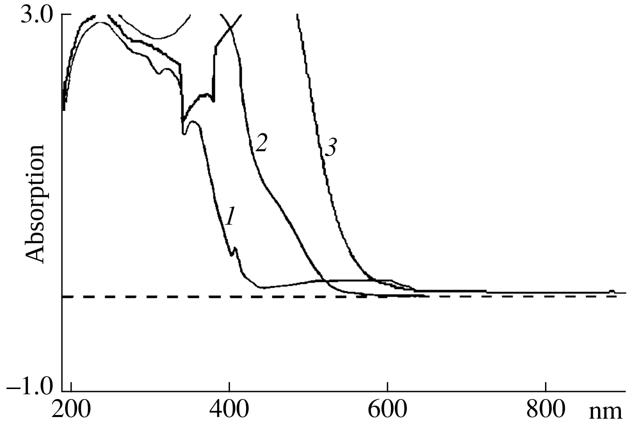

Fig. 3. The absorption spectra of 0.3% chloroform solutions of (*2*) pure PI-6B, (*3*) PI-6B containing 0.5 wt % C_{60} and (*1*) pure fullerene C_{60}.

intensity of illumination suggests that a similar behavior will be manifested under laser irradiation as well.

We have calculated the absolute values of the charge carrier mobility in plain and fullerene-modified samples. The results of these calculations show that the introduction of fullerenes leads to a tenfold increase in the mobility. The absolute values were estimated for a bias voltage of 10 V, a film thickness of $d = 2$ μm, a dielectric constant of $\varepsilon \sim 3.3$, a fullerene content of about 0.2 wt % C_{70}, and an upper electrode contact area with a diameter of 2 mm. Under these conditions, the carrier mobility in a fullerene-modified polyimide PI film is $\sim 0.3 \times 10^{-4}$ cm^2/(V s), while an analogous value for pure PI is $\sim 0.17 \times 10^{-5}$ cm^2/(V s). These values agree well with the data reported in [1, 7], where it was demonstrated that the carrier mobility in pure PI films ranges in the interval from 10^{-7} to 0.5×10^{-5} cm^2/(V s). Relationship (1) used for the estimation of charge carrier mobility is valid in the case of currents limited by the space charge. This situation is characteristic of most of the conjugated organic structures (in particular, PIs) in which the charge transfer processes are determined by traps, although formula (1) contains no terms dependent on the illumination intensity. However, taking into account the aforementioned equality of the activation energies of conductivity and mobility in PIs, the results of calculations of the relative changes in the carrier mobility probably adequately reflect the general trends in mobility variations. This behavior does not contradict the pattern of changes in the mobility observed for the other conjugated organic system (fullerene–carbazole) [8].

The above analysis is consistent with the process of complex formation in the polyimide–fullerene system considered previously [9, 10] and agrees with the spectral dependence of photoconductivity presented in Fig. 2 for thin PI-6B films modified with the fullerene C_{70}. The inset in Fig. 2 shows the spectra of photoconductivity for the films of pure fullerenes C_{60} and C_{70} [11].

There is a quite good agreement between the results described above and the absorption spectra of fullerene-containing PI films. Indeed, the absorption spectra exhibit a bathochromic shift and an increase in the intensity of absorption in the visible spectral range. Note that the absorption peak of pure PI occurs in the region of 380–400 nm. Figure 3 compares the absorption spectra of pure and fullerene-modified PI in chloroform. As demonstrated above, the introduction of fullerenes leads to a tenfold increase in the mobility of PI. As is known [5], an increase in the carrier mobility by one order of magnitude may lead to a twofold growth in the polyconjugation chain length. This circumstance does not contradict the notions about complex formation in polyimide systems and can be explained by an increase in the nonbarrier charge transfer pathlength related to the electron transition to fullerene, rather than to an intramolecular acceptor fragment of a polyimide molecule.

Thus, the system studied may feature a transition from intramolecular charge transfer between donor (triphenylamine) and acceptor (diimide) fragments to the intermolecular charge transfer between triphenylamine fragment and fullerene molecule, which is precisely what accounts for the bathochromic shift in the absorption spectrum. Note that the absorption spectra of thin films must also reveal this behavior (bathochromic shift), but we failed to obtain sufficiently thin films (below 0.5 μm) for measuring separate absorption peaks. The overall shift toward longer wavelength in

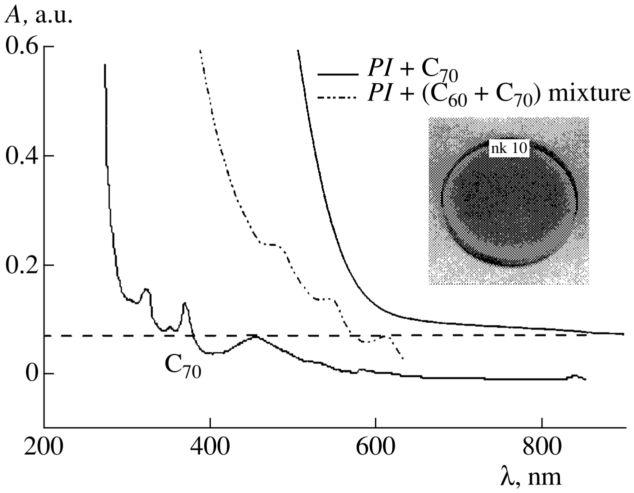

Fig. 4. The absorption spectra of fullerene-containing PI-6B films cast from tetrachloroethane solutions in comparison with the spectrum of fullerene C_{70}. The inset shows the general view of a sample of PI-6B containing fullerene C_{70}.

the spectra of fullerene-containing PI films is demonstrated in Fig. 4.

Conclusion. We have observed a tenfold increase in the mobility of charge carriers in films of polyimide 6B as a result of modification with fullerenes C_{60} and C_{70}. It is suggested that this can be related to a change in the charge transfer pathway: from the intramolecular process between donor (triphenylamine) and acceptor (diimide) to the intermolecular charge transfer between triphenylamine fragment and fullerene molecule. There is a correlation between fullerene-induced changes in the photoconductivity and spectroscopic properties of the polymer films. The observed behavior is also correlated with the trends in nonlinear optical properties of photosensitive fullerene-containing conjugated PI-based structures studied previously [10].

Acknowledgments. The authors are grateful to T.I. Vasil'eva (Vavilov Optical Institute) for depositing transparent conducting coatings and to V.I. Il'ina (Ioffe Physicotechnical Institute, Russian Academy of Sciences, St. Petersburg) for depositing gold contacts onto fullerene-containing organic films. Special thanks to N.A. Vasilenko (Karpov Institute of Physical Chemistry, State Scientific Center of the Russian Federation, Moscow), and to N.M. Shmidt and S.O. Kognovitskiĭ (Ioffe Physicotechnical Institute) for their help.

This study was performed within the framework of the Presidential Program "National Technological Basis" and partly supported by the Federal Program "Integration." M. M. Mikhailova is a graduate student of the Experimental Physics Department of St. Petersburg State Technical University; M. M. Kosyreva is a graduate student of the Department of Physical Optics and Optoelectronic Devices of St. Petersburg State Electrotechnical University.

REFERENCES

1. V. S. Mylnikov, in *Advances in Polymer Science*, Vol. 115: *Photoconducting Polymers/Metal-Containing Polymers* (Springer-Verlag, Berlin, 1991), pp. 3–88.
2. N. V. Kamanina and N. A. Vasilenko, Opt. Quantum Electron. **29**, 1 (1997).
3. P. I. Dubenskov, T. S. Zhuravleva, A. V. Vannikov, *et al.*, Vysokomol. Soedin., Ser. A **30** (6), 1211 (1988).
4. R. S. Ruoff, D. S. Tse, R. Malhotra, and D. S. Lorets, J. Phys. Chem. **97**, 3379 (1993).
5. N. A. Bakh, A. V. Vannikov, and A. D. Grishina, *Electric Conductivity and Paramagnetism of Polymeric Semiconductors* (Nauka, Moscow, 1971).
6. F. Gutman and L. E. Lyons, *Organic Semiconductors* (Wiley, New York, 1967).
7. G. M. Sessler, B. Hahn, and D. Y. Yoon, J. Appl. Phys. **60**, 318 (1986).
8. Y. Wang and A. Suna, J. Phys. Chem. B **101**, 5627 (1997).
9. N. V. Kamanina, I. V. Bagrov, I. M. Belousova, and A. P. Zhevlakov, Izv. Akad. Nauk, Ser. Fiz. **65** (4), 484 (2001).
10. N. V. Kamanina, Opt. Spektrosk. **90** (6), 960 (2001) [Opt. Spectrosc. **90**, 867 (2001)].
11. M. Hosoya, K. Ichimura, Z. H. Wang, *et al.*, Phys. Rev. B **49**, 4981 (1994).

Translated by P. Pozdeev

Technical Physics Letters, Vol. 28, No. 6, 2002, pp. 454–456. Translated from Pis'ma v Zhurnal Tekhnicheskoĭ Fiziki, Vol. 28, No. 11, 2002, pp. 21–27.
Original Russian Text Copyright © 2002 by Bokhan, Zakrevsky.

On the Mechanism of Electron Beam Generation in an Open Discharge with Anomalously High Efficiency

P. A. Bokhan and D. E. Zakrevsky

Institute of Semiconductor Physics, Siberian Division, Russian Academy of Sciences, Novosibirsk, 630090 Russia
e-mail: zakrdm@isp.nsc.ru

Received December 12, 2001

Abstract—The parameters of an open discharge operating without anode grid at elevated beam current densities are studied. It is demonstrated that the discharge is characterized by an almost 100% efficiency of electron beam generation in both pulsed and continuous regimes. A mechanism is proposed that accounts for such a high efficiency, according to which a zone of low potential gradient formed near the cathode blocks the ion current to cathode, while the electron emission proceeds by the photoemission mechanism. © *2002 MAIK “Nauka/Interperiodica”.*

In the preceding paper [1], we demonstrated that an open discharge without anode grid possesses in practice a significantly greater efficiency of continuous electron beam generation as compared to other types of gas discharge. In order to elucidate the mechanism of electron beam generation and determine the limiting characteristics of the open discharge without anode grid, we have studied operation of this discharge at high current densities in a quasi-continuous regime.

The experiments were conducted in a cell analogous to that described previously [1], with a working cathode area of ~1 cm^2. It should be recalled that the ion current to the cathode in this cell is suppressed by a special grid placed at a distance of δ = 1 mm from the cathode, which consists of dielectric plates spaced by h = 2 mm from each other. This grid decreases the ion-induced electron emission from the cathode. The experimental system employed a capacitor with C = 3.3 nF discharging through a thyratron and the discharge gap; the scheme was powered either in a pulsed regime (using rectangular pulses with a duration of 0.5–2 ms) or in a continuous regime (switched for a time of ~ 15 s). The discharge operation was stabilized by a ballast resistor connected in series to the discharge circuit.

Figure 1 shows typical oscillograms of currents to the anode (I_a) and to the electron collector (I_{ce}). As can be seen, there are three clearly distinguishable stages of discharge operation: (i) initiation, (ii) open discharge development, and (iii) quasistationary operation. The initiation stage (t ~ 0–6.5 μs) is characterized by a large anode current and low efficiency of electron beam generation. In the time interval from 6.5 to 12 μs, the anode current exhibits a sharp drop, while the electron beam generation efficiency increases (up to ~95%). Subsequently, despite a gradual decrease in the discharge voltage, the system features a significant increase in the discharge current and the electron beam generation efficiency.

These results can be interpreted as follows. In the stage of initiation taking place at a relatively low voltage (U < 1.5 kV), the system features a usual “anomalous” discharge with an electron beam generation efficiency of η = 20–40%. Similar to other types of a high-voltage glow discharge [2], this stage is characterized by a gradual increase in η with increasing discharge current density and voltage. As the voltage grows, an increasing proportion of electrons pass to the runaway regime and, hence, an increasing number of ions are formed outside the anode unit and recombine before reaching the cathode. By the time t ~ 10 μs, the major proportion of ions produced in the initiation stage within the region between the cathode and dielectric plates have already reached the cathode and, hence, electrons are mostly supplied to the discharge current due to photoemission under the action of radiation generated in the drift space. This stage is characterized by an extremely high electron beam generation efficiency (up to 99.8% for I_{ce} ~ 25 mA at t = 150 μs), which is only possible for the photoelectron emission mechanism.

As can be seen from Fig. 1, the conditions of maximum electron beam generation efficiency do not coincide with the regime of maximum electron beam current. Indeed, the maximum efficiency (irrespective of the initial voltage and the maximum electron beam current) takes place in the interval of currents about 20–25 mA. An increase in the working gas (helium) pressure to p_{He} > 8 Torr shifts the region of maximum electron beam generation efficiency toward greater currents, which is accompanied by a gradual decrease in η. The voltage of the open discharge operation initially exhibits a sharp drop, but then increases again (Fig. 2). The maximum electron beam generation efficiency observed in the experiment was η = 99.88% at p_{He} = 8 Torr.

In the system powered by millisecond rectangular pulses, the region of maximum efficiency shifts toward greater currents (30–40 mA at p_{He} = 7–8 Torr) and also reaches a level of η = 99.8%.

In the continuous regime, considerable power (up to ~100 W) is dissipated in the drift space and on the electron collector. This leads to a rapid heating of the cell which results, in particular, in a change of the working gas pressure (concentration) in the electron acceleration region. Since the current in the discharge gap and the voltage across the gap strongly depend on the concentration of gas molecules, the electron beam parameters remain unchanged only for 10–15 s. The results of measurements of the discharge characteristics in this regime are presented in Fig. 3. As can be seen, the discharge operation voltage in the continuous regime is somewhat higher and the maximum electron beam generation efficiency is lower (~99.5%) than those in the quasi-continuous case.

The above results are well consistent with the photoemission mechanism of the electron beam generation. An excess of the electron beam current over the anode current I_a compensating the ion current to the cathode is so large (up to 500 times) that this can by no means be explained by the ion-induced electron emission such as that in the usual open discharge. In practice, this implies that the cathode sputtering is very small and the working life of electron accelerators based on the open discharge without anode grid can be significantly longer as compared to that of systems implementing a high-voltage anomalous discharge [2, 3] or the usual open discharge.

On the other hand, the fact of stronger suppression of the ion current in the open discharge without anode grid indicates that the mechanism of electron acceleration and ion neutralization processes in this case is significantly different from that operative in the usual open discharge. Indeed, the electron beam generation efficiency (with neglect of the grid losses) is given by the formula [4]

$$\eta = \frac{1}{(1 + \Theta\delta(dw/dx)/w_0)}, \qquad (1)$$

where dw/dx and Θ are the energy losses of fast electrons and the fraction of such losses spent for the ionization, respectively, and w_0 is the energy required for the production of one ion. For helium, Θ = 0.51 and w_0 = 49 eV [5], dw/dx = 47 eV/cm for p_{He} = 8 Torr and w = 3 keV for a single electron [6]. Assuming that all ions formed over a gap length of δ = 1 mm (cathode–dielectric grid spacing) strike the cathode, we obtain an estimate of η = 95.3% and I_{ce}/I_a = 20, rather than η = 99.8% and I_{ce}/I_a = 500 as in the experiment.

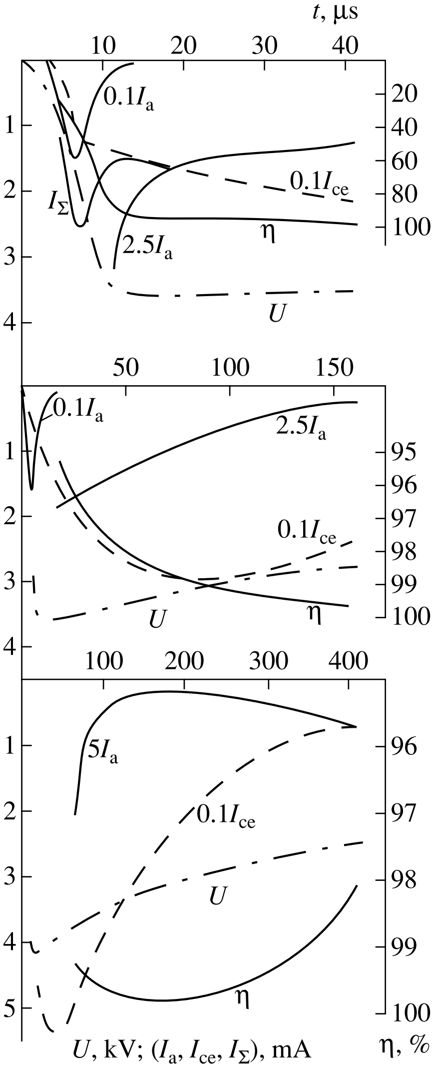

Fig. 1. Typical oscillograms of the discharge voltage (U), currents to the anode (I_a) and the electron collector (I_{ce}), total current (I_Σ), and the electron beam generation efficiency (η) observed at various initial voltages in an open discharge without anode grid at p_{He} = 8 Torr.

A key to understanding the mechanism of high-efficiency electron beam generation in the discharge studied is provided by data on the electron trajectories in the near-cathode region. Examination of the cathode surface showed that ion etching takes place within a narrow central zone in the region between the neighboring plates, rather than over the entire area exposed. The total width l of the ion-etched zone is much smaller than the spacing between plates (h = 2 mm): in the system studied, l ~ 0.5 mm. Since intense etching takes place only in the central part of this zone, the effective width of the etched area is still smaller, l_0 ~ 0.25 mm. This is indicative of the fact that the ion current to the greatest part of the exposed cathode surface is suppressed.

In our opinion, the mechanism of the ion current suppression is as follows. Since the shielded part of the

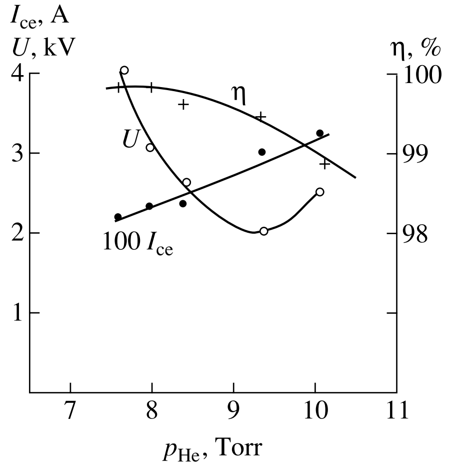

Fig. 2. Plots of the discharge parameters versus helium pressure: U, discharge voltage; I_{ce}, current to electron collector; η, electron beam generation efficiency.

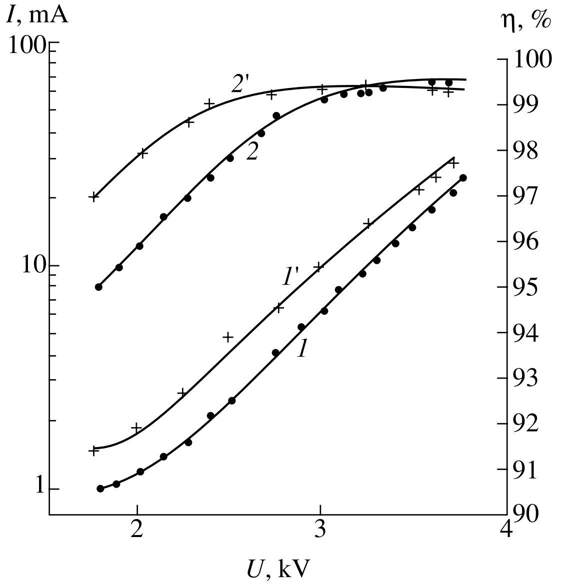

Fig. 3. Plots of the discharge parameters versus voltage U in a quasi-continuous operation regime at p_{He} = 8 (*1*, *2*) and 9 Torr (*1*', *2*'): (*1*, *1*') total current I_Σ; (*2*. *2*') electron beam generation efficiency η.

cathode surface (i.e., that under the plates) can be irradiated from the regions between plates and from the cathode–plate gap, the emitted and accelerated electrons strike the plates and charge them to a potential corresponding to the operative voltage. As a result, the field strength in the cathode–plate gap sharply decreases and the region of high potential gradient (in which electrons are effectively accelerated) moves away from the cathode by a distance of ~δ. Only in the central triangular zone of width ~l and height ~δ does the applied field sag into the gap between cathode and plates to produce a current of fast ions to the cathode surface. Outside this zone, ions are neutralized in the course of ambipolar diffusion not contributing to the current. As a result, the total ion current to cathode decreases in proportion to ~$0.5l_0/h$.

Taking into account the above considerations, formula (1) for the open discharge without anode grid must be modified as

$$\eta = \frac{1}{1 + \dfrac{\Theta\delta(dw/dx)}{w_0}\dfrac{0.5l_0}{h}}. \qquad (2)$$

The calculation using this formula for p_{He} = 8 Torr and U = 3 kV yields η = 99.8%, in agreement with the experimental data.

Thus, we have demonstrated that the open discharge without anode grid, operating with a current of 20–30 mA/cm^2, can provide for an electron beam generation efficiency of η = 99.8%. A mechanism is proposed that is responsible for such a high η value. According to this mechanism, photoelectrons emitted from the cathode are accelerated for the most part at a certain distance from the cathode, rather than in the near-cathode region. As a result, fast ions are prevented from striking the cathode and are mostly neutralized in the course of ambipolar diffusion, so that the ion current to the cathode is almost completely suppressed.

REFERENCES

1. P. A. Bokhan and D. E. Zakrevsky, Pis'ma Zh. Tekh. Fiz. **28** (2), 74 (2002) [Tech. Phys. Lett. **28**, 73 (2002)].
2. J. J. Rocca, J. D. Meyer, M. Farrell, *et al.*, J. Appl. Phys. **56** (3), 790 (1984).
3. M. A. Zav'yalov, Yu. E. Kreĭndel', A. A. Novikov, and L. P. Shanturin, *Plasma Processes in Electron Guns* (Énergoatomizdat, Moscow, 1989).
4. P. A. Bokhan, Zh. Tekh. Fiz. **61** (6), 61 (1991) [Sov. Phys. Tech. Phys. **36**, 620 (1991)].
5. S. V. Arlantsev, B. L. Borovich, V. V. Buchanov, *et al.*, J. Russ. Laser Res. **16** (2), 99 (1995).
6. J. A. La Verne and A. Mozumder, J. Phys. Chem. **89** (20), 4219 (1985).

Translated by P. Pozdeev

Technical Physics Letters, Vol. 28, No. 6, 2002, pp. 457–460. Translated from Pis'ma v Zhurnal Tekhnicheskoĭ Fiziki, Vol. 28, No. 11, 2002, pp. 28–36.
Original Russian Text Copyright © 2002 by Rakcheeva, Kamanina.

Prospects of the Use of Fullerenes for the Orientation of Liquid-Crystalline Compositions

L. P. Rakcheeva[a] **and N. V. Kamanina**[b,*]
[a] *St. Petersburg State Technical University, St. Petersburg, Russia*
[b] *Vavilov Optical Institute, State Scientific Center of the Russian Federation, St. Petersburg, 190164 Russia*
** e-mail: kamanin@ffm.ioffe.rssi.ru (Dr. Natalie V. Kamanina)*

Received December 26, 2001

Abstract—The dynamic characteristics of liquid crystal (LC) structures containing fullerenes C_{60} and C_{70} were studied, and the effect of fullerenes on the reorientation capacity of liquid crystal molecules was assessed. It is established that fullerenes C_{60} and C_{70} influence the operation time of polymer-dispersed LC cells containing photosensitive 2-cyclooctylamine-5-nitropyridine molecules. A possible mechanism of reorientation in the system is considered, and it is shown that fullerenes can provide for effective switching of the electrooptical response in such LC cells. Fullerenes have good prospects for use in orienting coatings of various types employed in the LC technology. *© 2002 MAIK "Nauka/Interperiodica".*

Introduction. The use of liquid crystals (LCs) in electrooptical switches, laser gates, light modulators, and some other devices for real-time-scale operation requires taking measures providing for fast response, high contrast, and good modulation properties. As is known, this complex problem cannot be solved by merely adjusting separate parameters of LC system design, since an increase in one characteristic usually leads to a decrease in some other property. For example, an increase in sensitivity is achieved at the expense of decreased spatial resolution, while attempts at increasing the resolution lead to a loss in the response speed, etc.

This interplay is well illustrated and explained within the framework of investigations of LC structures using holographic methods. As is known, the resolving power of a holographic grating can be determined using the dependence of the diffraction efficiency on the spatial frequency. The former characteristic is determined by the phase relief profile depth and by correspondence of this relief to the intensity distribution in the grating created in a photosensitive medium. For a signal written in the photosensitive structure of a grating with sinusoidal variation of the transmission, the intensity I_i of the ith order diffraction peak can be described (using a criterion proposed in [1]) by the expression

$$I_i = J_1^2(\Delta\Phi_{\max} - \Delta\Phi_{\min})/2, \quad (1)$$

where $\Delta\Phi_{\max} - \Delta\Phi_{\min}$ is the phase modulation depth and J_i is the ith order Bessel function of the first kind. The phase modulation depth is directly proportional to the LC layer thickness [2]:

$$\Delta\Phi = 2\pi d\Delta n/\lambda. \quad (2)$$

Here, d is the LC layer thickness, Δn is the LC birefringence, and λ is the wavelength of light acting upon the electrooptical medium.

As can be seen from relationships (1) and (2), an increase in the LC layer thickness leads to a corresponding increase in the phase modulation depth and, hence, in the electrooptical response. At the same time, the conventional way to increasing time characteristics is to reduce the LC layer thickness. Thus, the possibility of increasing the operation speed while retaining high resolution by means of changes in the system design is problematic. Therefore, alternative ways to optimization of the dynamic and modulation characteristics of LC devices have to be developed.

A complex approach to solving the problem of optimization stipulates both selecting a proper operation mode and the use of special orienting coatings at the boundaries between layers of the electrooptical device structure. The first way implies, for example, the use of a pulsed mode of writing data in the LC layer or a pulsed supply voltage. The pulsed techniques reduce polarization processes in the system and prevent LC molecules from dissociation. Another important factor is the time delay between the optical and bias voltage pulses, which has to be matched so as to minimize the charge relief spreading and, hence, the system response time. The second way to optimization consists essentially in modification of the physical conditions at the solid–LC layer boundary. In the case of using the orienting oxide coatings, an important factor is the surface relief geometry, while in using polymeric orienting films the dominating role belongs to physicochemical processes at the interface between media with different electrooptical parameters.

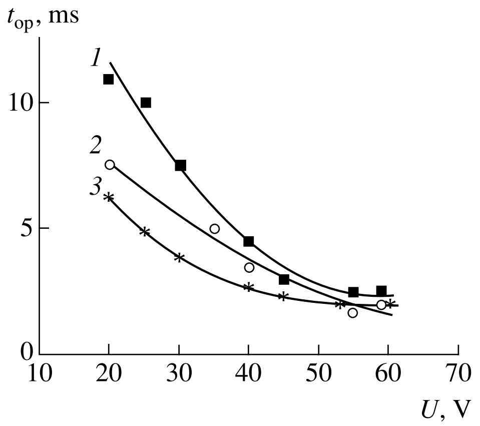

Fig. 1. The plots of operation time (t_{op}) versus amplitude of the supply voltage pulses for of the polymer-dispersed LC structures with orienting films (*1*) free of fullerenes and (*2*, *3*) containing fullerenes C_{60} and C_{70}, respectively. The measurements were performed using voltage pulses with a duration of τ_{sup} = 30 ms and a repetition frequency of $1/T$ = 0.5 Hz.

Below we consider the effect of fullerene-containing orienting coatings on the dynamic characteristics of polymer-dispersed photosensitive LC systems. It will be demonstrated that fullerenes C_{60} and C_{70} have good prospects for effective switching agents in electrooptical LC devices.

Experiment. The investigation was performed in LC cells of the *S* type with 10- to 12-μm-thick LC layers possessing the initial planar orientation. A photosensitive component in the polymer-dispersed system was 2-cyclooctylamine-5-nitropyridine (COANP), the room-temperature refractive index of which is close to that for an ordinary ray of the LC compositions employed. The ratio of photosensitive and LC components in the composition was 1 : 2. The composition was plasticized by a nonphotosensitive polyimide of grade 81A (PI-81A). The structure of COANP was preliminarily sensitized by adding 1–5 wt % fullerene C_{70}, which shifted the absorption edge of COANP into the region of wavelengths of the radiation source employed [3]. The electrooptical component was based on a standard nematic LC possessing positive optical and dielectric anisotropy: NZhK 1282 (Δn = 0.164, $\Delta\varepsilon$ = 9.9); NZhK 1289 (Δn = 0.168, $\Delta\varepsilon$ = 10); and E7 BDH (Δn = 0.224, $\Delta\varepsilon > 0$).

Orienting films with a thickness of ~0.5 μm were applied onto the surface of a glass substrate, over a preliminarily deposited transparent conducting film of indium and tin oxides (ITO). The orienting layer was applied using 2.5 to 3% solutions of PI-81A or PI-81B in tetrachloroethane. The concentration of the fullerene (C_{60} or C_{70}) additive in this layer was 0.1–0.5 wt % (relative to the dry polyimide weight). Tetrachloroethane is a good solvent both for polyimides and for fullerene clusters [4], which provided for the obtaining of homogeneous orienting coatings. The fullerene-modified PI films were applied onto the substrates by centrifuging and dried for 8–12 h until complete solvent removal. During the experiments, this layer was oriented by rubbing with flannel according to a special procedure.

The electrooptical cells were powered with rectangular pulses possessing an amplitude of A = 10–60 V, a duration of τ_{sup} = 5–100 ms, and a repetition frequency of $1/T$ = 0.5–50 Hz. The system was studied by measuring the transmission of the radiation of a He–Ne laser (λ = 633 nm) through a cell placed between crossed polarizers. The scheme of measurements was analogous to that reported elsewhere [5]. The electrooptical response rise time was determined for the first transmission oscillation, in which a transition to the adjacent extremum on the *S* curve could be clearly detected that corresponded to a change by π in the phase delay.

Results and discussion. Figure 1 shows the plots of operation time (t_{op}) of the polymer-dispersed LC cells versus amplitude of the supply voltage pulses, measured for τ_{sup} = 30 ms and $1/T$ = 0.5 Hz. The cell operation time was determined as the time required for the electrooptical response to change from 0.1 to 0.9 of the maximum level. As can be seen, all sample structures exhibit a decrease in the operation time with increasing amplitude of the voltage pulse (from 15–20 to 60 V). In practice, this parameter varies within 20% for the cells with fullerene-containing orienting coatings (cf. curves *1* vs. *2* and *3*, which refer to sample cells with the same numbers). The experiment revealed the influence of the structure of fullerene molecules (C_{60} vs. C_{70}) on the interval of operation times: the structures with fullerene C_{70} provide for somewhat better operation characteristics as compared to that with C_{60}. Apparently, both C_{60} and C_{70} significantly influence the packing of molecules in the LC layer by changing the cohesive energy of LC dipoles on the surface, but the elongated shape of C_{70} probably provides for a higher ordering of the LC structure already in the initial state, before application of the electric field.

We can consider the effect of fullerenes on the surface cohesion in terms of the free surface energy density F_s, the physical meaning of which is equivalent to the phase boundary surface tension. In the Rapini approximation [6],

$$F_s = 1/2 W_s \sin^2\theta. \qquad (3)$$

In this model, the orientation of LC molecules on the substrate surface is characterized by two parameters: θ, the average angle of tilt relative to the surface, and W_s, the surface cohesive energy. In our experiments, cell 3 exhibited a virtually planar orientation of the polymer-dispersed LC composition, which was confirmed both by analysis of the initial transmission portion of the *S* curve and by a better contrast observed for this structure. Thus, a smaller tilt of LC molecules relative to the substrate surface coated with a film containing fullerene C_{70} corresponded to minimization of the surface energy under otherwise equal conditions, including a constant absolute value of W_s. The latter parameter has a characteristic value for each particular orienting film, which requires further detailed investigation of the fullerene-containing orienting coatings for application in the LC display technology.

It is necessary to point out the following fact. Some investigations of the rotation ability of fullerenes C_{60} and C_{70} showed that the rotation frequency is temperature dependent and amounts to $\sim 10^{12}$ s^{-1} at 300 K. For C_{60} molecules excited at 528 nm, the characteristic rotation times in various solutions were as follows: toluene, 7 ± 1.5 ps; *o*-dichlorobenzene, 10.3 ± 1.5 ps; *o*-xylene, 13 ± 2 ps; and decalin, 3.5 ± 1.5 ps [7]. The rotation of C_{70} in chlorobenzene is characterized by 8 ± 2 ps [8]. Thus, fullerene molecules can follow changes of the electric field vector in the light wave at a sufficiently high rate. In our experiments with the sample structures excited by radiation of a He–Ne laser, the boundary conditions at the interface between a fullerene-containing orienting film and electrooptical layer may vary at a rather high rate, which is followed by accelerated reorientation of the LC director upon application of the voltage pulse. Note that this time variation of the boundary conditions should probably be taken into account in the analysis based on formula (3), for example by, introducing an additional term describing more adequately the complicated character of reorientation of molecules in a given polymer-dispersed LC composition.

An analysis of the presented in Fig. 1 shows that the light action upon the reorientation ability of the structures studied probably prevails over the electric field action. As the voltage pulse amplitude exceeds ~40 V, there is no difference in time characteristics of the systems containing fullerene additives of various types in the orienting film. This circumstance is not at variance with the previously established fact [9] that better switching characteristics were observed for polymer-dispersed LC structures sensitized by fullerenes in comparison to the usual nematic LC cells with the electrooptical layer not sensitized by fullerenes. The ability of fullerene molecules to follow the orientation electric field vector in the light wave (or the electric field strength variations) at a high rate is directly manifested in the experiments with cells containing fullerenes both in the orienting film and in the electrooptical layer.

Figure 2 illustrates the possible mechanism of reorientation in an LC composition, which takes into account the rotation ability of fullerene molecules. Here, the system characterized by the reorientation time t_1 corresponds to probing the cells without fullerenes introduced into the bulk of the polymer-dispersed LC composition, while the case of t_2 refers to a fullerene-sensitized composition. Based on the time characteristics observed in this study and the results reported previously [9], we may ascertain that $t_2 < t_1$. It should be noted that, in order to simplify the drawing, fullerenes present in the orienting coating are not depicted in Fig. 2. The proposed mechanism can be also operative in LC structures with fullerene-free orienting coatings and fullerene-containing electrooptical layers. Nor do we consider the possible cases of more complicated patterns of molecular alignment. For example, fullerenes may form charge-transfer complexes with the donor fragment of a π-conjugated photosensitive molecule (COANP) [10], thus orienting the molecule, after which the π-conjugated molecule–fullerene complex aligns the LC dipoles along the walls.

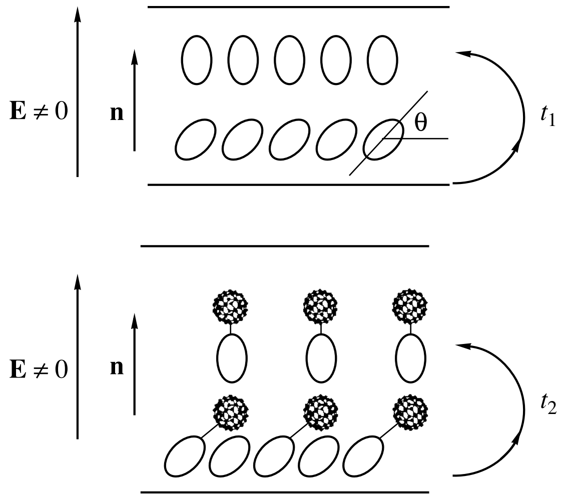

Fig. 2. The possible mechanism of reorientation in a polymer-dispersed LC composition, which takes into account the rotation ability of fullerene molecules: **n** is the orientation of LC director; **E** is the electric field vector of a light wave or an applied field; t_1 and t_2 are the characteristic rotation times (see the text for explanations).

Conclusions. Thus, the results of our experiments and model considerations demonstrate the following:

1. Fullerenes significantly influence the process of reorientation of polymer-dispersed LC compositions in the bulk of the electrooptical structure. A possible mechanism of this reorientation, which takes into account the rotation ability of fullerene molecules, has been considered on a qualitative level.

2. A difference in the time characteristics of the polymer-dispersed LC compositions with variable content of fullerenes C_{60} and C_{70} in the orienting film has been demonstrated. The presence of C_{60} or C_{70} molecules significantly activates processes at the phase boundaries.

3. The results of this investigation can be used for the creation of LC-based devices of a new type, operating in a real time scale, and for the development of technological processes related to the synthesis of orienting polymer and oxide coatings.

Acknowledgments. The authors are grateful to T.I. Vasil'eva (Vavilov Optical Institute) for depositing transparent conducting coatings and to N.A. Vasilenko (Karpov Institute of Physical Chemistry, State Scientific Center of the Russian Federation, Moscow) and L.N. Kaporskiĭ (Vavilov Optical Institute) for their help. L.P. Rakcheeva is a graduate student of the Experimental Physics Department of St. Petersburg State Technical University. This study was performed within the framework of the Presidential Program "National Technological Basis" and partly supported by the Federal Program "Integration" and the Russian Foundation for Basic Research (project no. 01–03-33162).

REFERENCES

1. Yu. D. Dumarevskiĭ, T. V. Zakharova, N. F. Kovtonyuk, *et al.*, Opt.-Mekh. Prom-st., No. 12, 9 (1989) [Sov. J. Opt. Technol. **56**, 729 (1989)].
2. A. A. Vasil'ev, D. Casasent, I. N. Kompanets, and A. V. Parfenov, *Spatial Light Modulators* (Radio i Svyaz', Moscow, 1987).
3. N. Kamanina, A. Barrientos, A. Leyderman, *et al.*, Mol. Mater. **13** (1-4), 275 (2000).
4. R. S. Ruoff, D. S. Tse, R. Malhotra, and D. C. Lorents, J. Phys. Chem. **97**, 3379 (1993).
5. N. V. Kamanina and V. I. Berendyaev, Proc. SPIE **3292**, 154 (1998).
6. G. M. Zharkova and A. S. Sonin, *Liquid Crystal Composites* (Nauka, Novosibirsk, 1994).
7. I. V. Rubtsov, D. V. Khudiakov, V. A. Nadtochenko, *et al.*, Chem. Phys. Lett. **229** (4-5), 517 (1994).
8. I. V. Rubtsov, D. V. Khudiakov, A. P. Motavskii, and V. A. Nadtochenko, Chem. Phys. Lett. **249** (1-2), 101 (1996).
9. N. V. Kamanina and L. N. Kaporskiĭ, Pis'ma Zh. Tekh. Fiz. **26** (19), 30 (2000) [Tech. Phys. Lett. **26**, 864 (2000)].
10. N. V. Kamanina, J. Opt. A **3** (5), 321 (2001).

Translated by P. Pozdeev

Technical Physics Letters, Vol. 28, No. 6, 2002, pp. 461–463. Translated from Pis'ma v Zhurnal Tekhnicheskoĭ Fiziki, Vol. 28, No. 11, 2002, pp. 37–43.
Original Russian Text Copyright © 2002 by Vendik, Gashinova, Deleniv.

The Effect of a Thin Ferroelectric Film on the Propagation Characteristics of a Microstrip Transmission Line

O. G. Vendik[a],*, M. S. Gashinova[a], and A. N. Deleniv[b],**
[a] *St. Petersburg State Electrotechnical University, St. Petersburg, 197376 Russia*
** e-mail: ogvendik@mail.eltech.ru*
[b] *Chalmers University of Technology, SE-41296, Göteborg, Sweden*
*** e-mail: anatoli@ep.chalmers.se*

Received January 18, 2002

Abstract—The properties of a microstrip line (MSL) on a bilayered substrate containing a thin ferroelectric layer are theoretically studied. The propagation parameters are calculated using an approach based on a two-dimensional full-wave electrodynamic model. The influence of the fringing electric field in the ferroelectric layer on the MSL characteristics is studied. It is shown that correct modeling of microwave devices based on bilayered substrates with ferroelectric layers must take into account the properties of these layers even despite very small thickness. *© 2002 MAIK "Nauka/Interperiodica".*

Formulation of the problem and analysis of the model. In recent years, microwave electronics makes use of phase shifters employing ferroelectric films, which represent integrated circuits fabricated by standard technologies without manual assembly and adjustment operations [1, 2]. Such microwave integrated circuits are based on insulating substrates (sapphire, polycrystalline alumina, MgO, $LaAlO_3$) coated with thin (0.5–1.0 μm) ferroelectric layers of $(Ba,Sr)TiO_3$. The tunable element is implemented in the form a planar capacitor representing a gap (s = 5–20 μm) in the conducting film [3] deposited over the ferroelectric layer. The capacitance of this planar capacitor is controlled by applied voltage. The ferroelectric film extends beyond the gap width and covers the whole substrate, which is explained only by the sequence of technological operations used for the device fabrication. In order to provide for a correct modeling of such devices, it is necessary to know how the presence of a thin ferroelectric layer influences the propagation characteristics of microstrip lines (MSLs).

The simplest model of the electric field distribution in an MSL (Fig. 1a) formulated in a quasistatic approximation [4, 5] is characterized by an effective strip width (w_{eff}) and an effective dielectric constant ε_{eff}. This MSL model is known as the quasi-TEM approximation, which is correct in the case of lines with the cross section small relative to the wavelength in the substrate:

$$w, h_s < 0.05\lambda_0/\sqrt{\varepsilon_s}, \tag{1}$$

where w is the strip width, h_s and ε_s are the substrate thickness and permittivity, respectively, and λ_0 is the wavelength in vacuum.

Let us apply this approximation to an MSL with a bilayered substrate containing a ferroelectric layer. The capacitance per unit length can be calculated as the capacitance of a layered capacitor:

$$C_1 = \frac{\varepsilon_0 w_{\text{eff}}}{h_s/\varepsilon_{s,\,\text{eff}} + h_f/\varepsilon_f}. \tag{2}$$

Here, $\varepsilon_{s,\,\text{eff}}$ is the effective dielectric constant of the substrate, h_f and ε_f are the thickness and permittivity of the

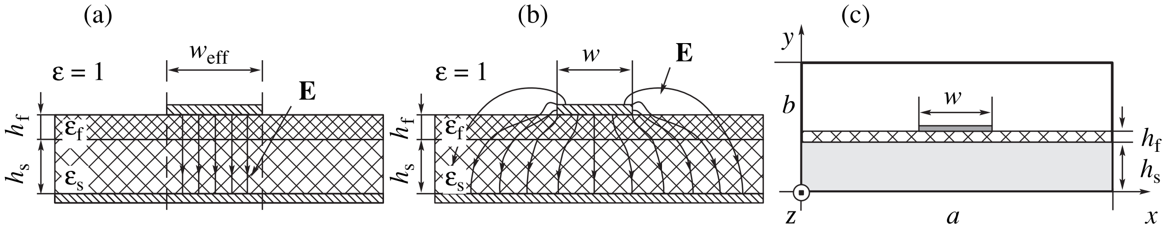

Fig. 1. A microstrip line on a bilayered substrate with an upper ferroelectric layer: (a) a model without fringing field; (b) a model with fringing field; (c) cross section diagram.

1063-7850/02/2806-0461$22.00 © 2002 MAIK "Nauka/Interperiodica"

ferroelectric film, respectively, and ε_0 is the permittivity of vacuum. For $h_s \gg h_f$ and $\varepsilon_s \ll \varepsilon_f$, the second term in the denominator of formula (2) is much smaller than the first one. This implies that, in the approximation under consideration, the presence of the ferroelectric film does not influence the MSL characteristics. In order to provide for a more correct approach, it is necessary to take into account that a certain part of the fringing field is parallel to the ferroelectric layer (Fig. 1b). For this reason, the electric field energy density in the ferroelectric can be $\varepsilon_f/\varepsilon_s$ times greater than that in the substrate. Therefore, the effect of the ferroelectric layer on the MSL characteristics must be taken into account even despite small thickness of this layer.

Method of calculation. The wave propagation parameters in an MSL based on a bilayered substrate are determined using the full-wave analysis based on the spectral-domain approach. In the general form, this method is formulated for calculating the complex propagation parameters of boxed multi-conductor planar lines in multilayer media.

The spectral Green functions are calculated within the framework of the immittance approach [6]. Using a recursive procedure for calculating the impedance of each layer (considered as a loaded line section of the equivalent circuit) for all fundamental modes, it is possible to construct a flexible algorithm for calculating the diadic Green functions for an arbitrary number of layers above and below the electrode interface. The layers are characterized by thicknesses and permittivities.

Using the standard spectral-domain notation [7], a system of linear equations for the fields and current densities in the conducting surface can be written in the following form:

$$\begin{bmatrix} \tilde{E}_z(\alpha_n) \\ \tilde{V}_x(\alpha_n) \end{bmatrix} = \begin{bmatrix} \tilde{Z}_{zz} & \dfrac{\tilde{Z}_{zx}}{-j\alpha_n} \\ \dfrac{\tilde{Z}_{xz}}{-j\alpha_n} & \dfrac{\tilde{Z}_{xx}}{-\alpha_n^2} \end{bmatrix} \begin{bmatrix} \tilde{J}_z(\alpha_n) \\ \tilde{J}'_x(\alpha_n) \end{bmatrix}, \qquad (3)$$

$$V_x(x) = \int_{-a}^{x} E_x(x')dx'.$$

Here, $\tilde{E}_{z,x}$ and $\tilde{J}_{z,x}$ are the tangential components of the electric field and current density, respectively; $Z = \begin{pmatrix} \tilde{Z}_{zz} & \tilde{Z}_{zx} \\ \tilde{Z}_{xz} & \tilde{Z}_{xx} \end{pmatrix}$ is the Green dyad; and α_n is the Fourier variable (the tilde denotes the Fourier image of the corresponding function). Functions describing the tangential components of the electric current density are expanded into series with respect to a basis set formed by the Chebyshev polynomials of the first kind. Applying the Galerkin method to solving Eq. (3), we arrive at a homogeneous system of linear equations

$$[A(\omega, k_z)][X] = 0, \qquad (4)$$

where $[A(\omega, k_z)]$ is the matrix of scalar products in the corresponding space, $[X]$ is the vector of unknown coefficients in the expansion of current densities J_z and J_x, ω is the circular frequency, and k_z is the propagation constant along the transmission line. A nontrivial solution to (4) determines the value of k_z at a given frequency ω.

Using the obtained propagation constant, we can calculate the related modal impedance of the MSL. Based on the method proposed in [8], it is possible to determine the power transmitted in the structure with an arbitrary number of layers. This value is used to determine the eigenvector of voltages by the formula

$$P = \frac{1}{2}VI^*, \qquad (5)$$

where asterisk denotes the complex conjugate. The wave impedance of the line for the fundamental mode is defined as $Z_0 = V/I$.

Figure 1c shows the model structure of a single MSL embedded in a three-layer medium. A metal "box" with ideally conducting walls has the side dimensions $a = 5$ mm and $b = 10$ mm. The calculations were performed for a frequency of $f = 12$ GHz. The results of the calculations are obtained in the form of the propagation constant of the fundamental mode and the corresponding wave impedance Z_0 and, accordingly, of the effective dielectric constant and the effective strip width on a bilayered substrate:

$$\varepsilon_{\text{eff}} = (k_z c/\omega)^2, \qquad (6)$$

$$w_{\text{eff}} = \frac{120\pi(h_s + h_f)}{Z_0\sqrt{\varepsilon_{\text{eff}}}}, \qquad (7)$$

where c is the speed of light in vacuum.

Results and discussion. Figure 2 presents the values of ε_{eff} and Z_0 as functions of the ratio of layer thicknesses h_f/h_s for $h_s = 500$ μm and $\varepsilon_s = 10$. The calculations were performed for various strip widths ($w = 0.25$, 0.5, and 1.0 mm) and various permittivities of the ferroelectric material ($\varepsilon_f = 400$ and 1000). The ε_{eff} and Z_0 values obtained for $h_f = 0$ (an MSL without a ferroelectric layer) coincide with the results of modeling within the framework of the quasistatic approach [4, 5]. The effective strip width w_{eff} is independent of h_f and coincides with the w_{eff} value obtained in the quasistatic approximation for $h_f = 0$ [4, 5].

Based on the above analysis, we arrive at the following conclusions:

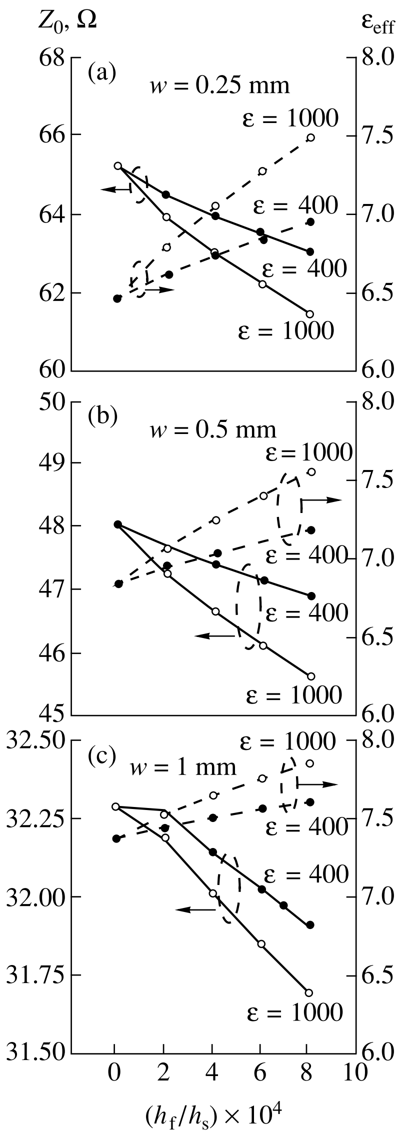

Fig. 2. The results of calculations of the effective permittivity and wave impedance of the model MSL for $\varepsilon = \varepsilon_f$.

1. The effective permittivity of an MSL on a bilayered substrate with a thin ferroelectric layer significantly depends on the ferroelectric layer thickness. A rough estimation is provided by the formula

$$\varepsilon_{\rm eff}(h_f) \cong \varepsilon_{\rm eff}(0) + \frac{h_f}{w}\varepsilon_f, \tag{8}$$

where $\varepsilon_{\rm eff}(0)$ is the effective dielectric constant of the MSL in the absence of the ferroelectric film [4, 5].

2. In the case when the condition (1) is fulfilled, the presence of a thin ferroelectric film virtually does not influence the effective strip thickness.

The capacitance (C_1) and inductance (L_1) per unit length of the line are determined using the well-known formulas

$$Z_0 = \sqrt{L_1/C_1}, \quad k_z = \omega\sqrt{L_1 C_1} \tag{9}$$

in combination with relationships (6) and (7), which yield

$$\begin{aligned} C_1 &= \varepsilon_0\varepsilon_{\rm eff}(h_f)w_{\rm eff}/(h_s + h_f), \\ L_1 &= \mu_0(h_s + h_f)/w_{\rm eff}. \end{aligned} \tag{10}$$

These expressions are consistent with the above conclusion that C_1 depends on the thickness and permittivity of the ferroelectric layer, whereas L_1 is virtually independent of the parameters of this layer.

Acknowledgments. The authors are grateful to I.B. Vendik for valuable advice and comments.

REFERENCES

1. O. Vendik, I. Vendik, N. Setter, *et al.*, IEEE Microwave Wireless Components Lett. **11** (10), 407 (2001).
2. A. B. Kozyrev, A. V. Ivanov, O. I. Soldatenkov, *et al.*, Pis'ma Zh. Tekh. Fiz. **27** (24), 16 (2001) [Tech. Phys. Lett. **27**, 1032 (2001)].
3. O. G. Vendik, S. P. Zubko, and M. A. Nikol'skiĭ, Zh. Tekh. Fiz. **69** (4), 1 (1999) [Tech. Phys. **44**, 349 (1999)].
4. R. K. Hoffmann, *Handbook of Microwave Integrated Circuits* (Artech House, Boston, 1987).
5. I. Kasa, *Microwave Integrated Circuits* (Elsevier, New York, 1991).
6. T. Itoh, IEEE Trans. Microwave Theory Tech. **28**, 733 (1980).
7. G. Cano, F. Medina, and M. Horno, IEEE Trans. Microwave Theory Tech. **46**, 1801 (1998).
8. G. Cano, F. Medina, and M. Horno, IEEE Trans. Microwave Theory Tech. **40**, 217 (1992).

Translated by P. Pozdeev

Technical Physics Letters, Vol. 28, No. 6, 2002, pp. 464–466. Translated from Pis'ma v Zhurnal Tekhnicheskoĭ Fiziki, Vol. 28, No. 11, 2002, pp. 44–50.

Helicons in an Optical Fiber

I. V. Dzedolik and A. I. Dzedolik

Tauride National University, Simferopol, Ukraine

e-mail: dzedolik@crimea.edu

Received September 24, 2001; in final form, January 10, 2002

Abstract—Solutions for nonlinear helical electric and magnetic waves and polarization modes in a quartz fiber are found. Parameters of these modes (the normal velocity of the wave front and the helix pitch) are calculated as functions of the fiber properties and the amplitude and frequency of the electromagnetic field. *© 2002 MAIK "Nauka/Interperiodica".*

Active media with continuous inflow and dissipation of the energy supplied from an external source may support 2D single-arm and multiarm helical waves (helicons) as well as 3D wave structures such as simple and twisted vortices whose centers of rotation form the vortex filament [1]. In this sense, the optical fiber is a passive, dissipative medium. However, due to the presence of interfaces between the fiber core and the cladding, the electromagnetic field existing in this guiding structure propagates in the form of modes satisfying (in the linear case) the translation and superposition conditions [2]. Hybrid *EH* and *HE* modes, which correspond to oblique rays in the fiber, possess helicoidal (spiral) equiphase surfaces [3].

Similarly, density waves existing in a liquid or gas filling a cylindrical tube propagate in the form of guided modes, in particular, as helicons [4]. The wave front of such a mode twists into a helix: the peripheral parts are retarded, because the wave velocity in the medium is constant, $v = \omega r = \text{const}$ [1]. Helicons arise on the surface of a vortex cavity in a liquid or gas [3], etc. The analogy between nonlinear and linear helicons is very interesting and informative. Helicons arising in an optically transparent passive medium may be treated as an example of self-organization of electromagnetic field due to the nonlinear interaction between the field and the medium.

An example of self-organized electromagnetic field actively studied nowadays is offered by vortex solitons [5, 6]. The dynamics of solitons existing in an optical fiber can be described by variations of the envelope as a function of the time and the longitudinal coordinate [7]. Unlike these objects, nonlinear vortices and helicons are primarily described by the transverse field distribution.

Let us consider conditions for excitation of the polarization waves and electromagnetic helicons in an optically transparent medium with a homogeneous refractive index. In steady-state conditions, the phase of a helicon is $\phi = \omega t - \theta(r) + l\varphi - \beta z$, where $\theta(r)$ is a function of the polar radius which describes the shape of the helix, φ is the polar angle, l is the azimuthal index (topological charge) specifying the number of arms in the helix, and z is the longitudinal coordinate. Write the system of Maxwell's equations for the electromagnetic field in a nonconducting dielectric (quartz waveguide),

$$\nabla \times \mathbf{B} = \frac{1}{c}\frac{\partial \mathbf{D}}{\partial t}, \quad \nabla \mathbf{D} = 0,$$
$$\nabla \times \mathbf{E} = -\frac{1}{c}\frac{\partial \mathbf{B}}{\partial t}, \quad \nabla \mathbf{B} = 0, \tag{1}$$

and the constitutive equation

$$\mathbf{D} = \mathbf{E} + 4\pi\mathbf{P}, \tag{2}$$

where $\mathbf{P} = -eN\mathbf{r}$ is the polarization vector of the medium. Taking into account formula $\nabla\mathbf{F} + 4\pi\nabla\mathbf{P} = 0$, we obtain from (1) and (2) the following equation:

$$\left(\nabla^2 - \frac{1}{c^2}\frac{\partial^2}{\partial t^2}\right)\mathbf{E} = -4\pi\left[\nabla(\nabla\mathbf{P}) - \frac{1}{c^2}\frac{\partial^2\mathbf{P}}{\partial t^2}\right]. \tag{3}$$

The unit cell of quartz possesses the center of symmetry; therefore, the potential of the crystal lattice can be approximated by the even periodic function $U = -f_0\cos\left(\frac{2\pi}{r_0}r\right)$, where r_0 is the mean atomic radius. The equation of motion for an optical electron in the atom situated in a site of the quartz lattice can be written as

$$m\frac{d^2\mathbf{r}}{dt^2} = -\nabla U - \sigma\frac{d\mathbf{r}}{dt} - e\mathbf{E}, \tag{4}$$

where $-\nabla U = -\mathbf{f}_0\sin\left(\frac{2\pi}{r_0}r\right)$ is the "averaged" restoring force of the crystal lattice. Let us multiply Eq. (4) by

$-eN$ and divide the result by the electron mass m to obtain the equation for polarization

$$\frac{d^2\mathbf{P}}{dt^2} = -\mathbf{f}_m\sin(\mathbf{qP}) + \sigma_m\frac{d\mathbf{P}}{dt} + v_e^2\mathbf{E}, \qquad (5)$$

where $\mathbf{f}_m = \mathbf{f}_0 eN/m$, $\mathbf{q} = \mathbf{1}(2\pi/r_0 eN)$, $\sigma_m = \sigma/m$, and $v_e^2 = e^2N/m$. System (3)–(5) describes nonlinear modes of a dielectric waveguide. Upon obtaining a solution for the electric field from (3)–(5), we can find the magnetic field from (1):

$$\mathbf{B} = -c\nabla\int dt\mathbf{E}. \qquad (6)$$

Let us find the solution to system (3)–(5) in the simplest case when vectors of the electromagnetic field and polarization have only radial components: $E = E_r(r, \varphi, z)$ and $P = P_r(r, \varphi, z)$. Then Eqs. (3)–(5) reduce to the system

$$\begin{gathered}\left(\nabla^2 - \frac{1}{c^2}\frac{\partial^2}{\partial t^2}\right)E = -4\pi\left(\frac{\partial^2 P}{\partial r^2} - \frac{P}{r^2} + \frac{1}{r}\frac{\nabla P}{\partial r}\right) + \frac{4\pi}{c^2}\frac{\partial^2 P}{\partial t^2}, \\ \frac{\partial^2 P}{\partial t^2} - \sigma_m\frac{\partial P}{\partial t} + f_m\sin(qP) = v_e^2 E.\end{gathered} \qquad (7)$$

Representing the field components and polarization vector as $E = E_0\exp(i\phi)$, $B = B_0(i\phi)$, and $P = P_0(i\phi)$, we can rewrite system (7) in the form

$$\begin{gathered}\left[\frac{\partial^2\theta}{\partial r^2} - i\left(\frac{\partial\theta}{\partial r}\right)^2 + \frac{1}{r}\frac{\partial\theta}{\partial r} + i\left(\frac{\omega^2}{c^2} - \beta^2 - \frac{l^2}{r^2}\right)\right]E \\ = -4\pi\left[\frac{\partial^2\theta}{\partial r^2} - i\left(\frac{\partial\theta}{\partial r}\right)^2 + \frac{1}{r}\frac{\partial\theta}{\partial r} - i\frac{1}{r^2} + i\frac{\omega^2}{c^2}\right]P, \qquad (8) \\ P - \frac{f_m}{\omega^2 + i\sigma_m\omega}\sin(qP) = -\frac{v_e^2}{\omega^2 + i\sigma_m\omega}E.\end{gathered}$$

Expanding the sine function into the power series as $\sin(qP) = qP(1 - q^2P_0^2/3! + q^4P_0^4/5! - q^6P_0^6/7! + \ldots) \equiv \mu qP$ and substituting the expansion into (8), we obtain the “dispersion relation”

$$\begin{gathered}\frac{\partial^2\theta}{\partial r^2} - i\left(\frac{\partial\theta}{\partial r}\right)^2 + \frac{1}{r}\frac{\partial\theta}{\partial r} = \frac{i\omega_e^2}{\omega^2 - \omega_e^2 - \mu q f_m + i\sigma_m\omega} \\ \times\left(\beta^2 + \frac{l^2 - 1}{r^2}\right) - i\left(\frac{\omega^2}{c^2} - \beta^2 - \frac{l^2}{r^2}\right).\end{gathered} \qquad (9)$$

Using the notation $\eta = d\theta/dr$, we can rewrite Eq. (9) as

$$\frac{d\eta}{dr} - i\eta^2 + \frac{1}{r}\eta = i\left(\beta^2(1+\gamma) - \frac{\omega^2}{c^2} + \frac{l^2(1+\gamma) - \gamma}{r^2}\right), \qquad (10)$$

where $\gamma = \omega_e^2/(\omega^2 - \omega_e^2 - \mu q f_m + i\sigma_m\omega)$. This equation represents the general Riccati equation. Using the substitution $\eta = id\ln(u)/dr$, we can transform (10) to the Bessel equation

$$\frac{d^2u}{dr^2} + \frac{1}{r}\frac{du}{dr} + \left(\frac{\omega^2}{c^2} - \beta^2(1+\gamma) - \frac{l^2(1+\gamma) - \gamma}{r^2}\right)u = 0. \qquad (11)$$

The solution to Eq. (11) can be written in the form of the Hankel function $u = C_0H_m^{(1)}(R)$, where $R = \sqrt{\omega^2/c^2 - \beta^2(1+\gamma)}\,r$ and $m = \sqrt{l^2(1+\gamma) - \gamma}$. Using the inverse substitution $\eta = i(du/dr)/u = i\sqrt{\omega^2/c^2 - \beta^2(1+\gamma)}\,[dH_m^{(1)}(R)/dR]/H_m^{(1)}(R)$ and integrating the variable $\eta = d\theta/dr$, we find the shape of the helicon:

$$\theta = \int\eta dr = i\int\frac{d\ln H_m^{(1)}(R)}{dR}dR = i\ln H_m^{(1)}(R); \qquad (12)$$

substituting (12) into formula $E = E_0\exp(i\phi)$, we obtain the expression for electric field

$$E_r = E_0H_m^{(1)}(R)\exp[i(\omega t + l\varphi - \beta z)]. \qquad (13)$$

Far from the absorption region, formula (13) with $\gamma \ll 1$ ($m = l$) coincides with expressions for spiral chemical waves [3] and waves in a gas [4].

Substituting (13) into (6), we find the magnetic field:

$$B_\varphi = -c\frac{\partial}{\partial z}\int dtE = \frac{c\beta B_0}{\omega}H_m^{(1)}\exp[i(\omega t + l\varphi - \beta z)]. \qquad (14)$$

The complex Poynting vector for the case under study is

$$\begin{gathered}\mathbf{S} = \frac{c}{4\pi}\mathbf{E}\times\mathbf{B} = \frac{c}{4\pi}\mathbf{1}_zE_rB_\varphi \\ = \mathbf{1}_z\frac{c\beta E_0B_0}{\omega}[H_m^{(1)}(R)]^2\exp[i2(\omega t + l\varphi - \beta z)].\end{gathered} \qquad (15)$$

The nonlinear polarization modes in the quartz waveguide, the electric and magnetic modes (13) and (14), and the energy flux density (15) represent helicons. For $R \gg 1$, the cross sections of their equiphase surfaces are the Archimedean spirals: $\omega t - R + l\varphi - \beta z = \text{const}$ (Fig. 1). Near the waveguide axis (at $R \longrightarrow 0$), the front of a helicon wave is distorted.

Let us find the velocity of point A in a helicon which is separated by distance r from the helix center O [1]. For this purpose, we draw a circle centered at O and passing through the point A. The velocity of the wave front crossing this circle equals $v_\tau = \omega r$; the velocity of the normal displacement of the wave front is denoted by v_n (Fig. 2). The velocity of circular motion is related to the normal velocity of the wave front as $v_\mathrm{n} = v_\tau\cos\alpha$,

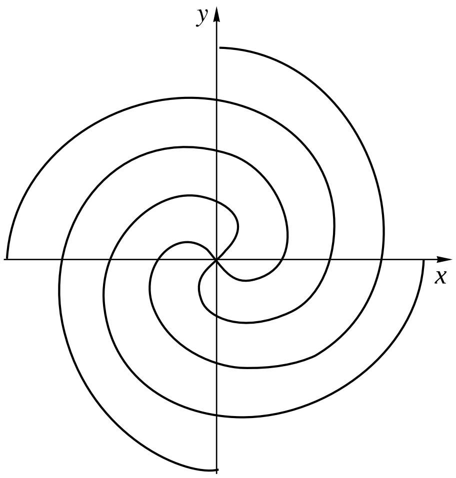

Fig. 1. Equiphase surfaces $\omega t - \beta z$ = const of a helicon with the topological charge $l = 4$ in the cross section of a quartz fiber.

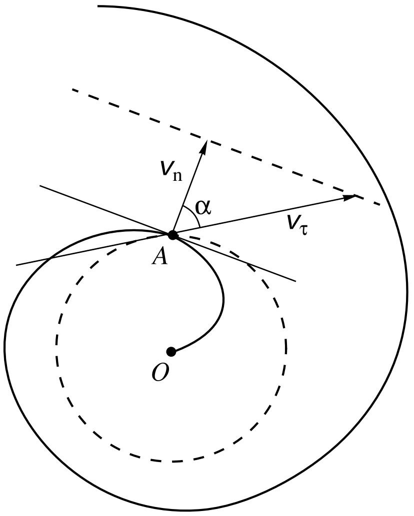

Fig. 2. Velocity of the helicon front in the cross section of a quartz fiber.

where α is the angle between the normal to the wave front and the tangent line to the circle at the point *A*. Taking into account the formula $\tan\alpha = rd\phi/dr = -r\eta$, we find that $\cos\alpha = 1/\sqrt{1 + \tan^2\alpha} = 1/\sqrt{1 + r^2\eta^2}$. The velocity of normal displacement of the helicon wave front is determined by the expression

$$v_n = \frac{v_\tau}{\sqrt{1 + r^2\eta^2}}$$

$$= \frac{\omega}{\sqrt{r^{-2} + [\beta^2(1+\gamma) - \omega^2/c^2][d\ln H_m^{(1)}(R)/dR]^2}}.$$

The helicon pitch can be determined from the equation $\theta = (R + h_S) - \theta(R) = 2\pi$, which, in the case under study, takes the form $H_m^{(1)}(R + b_S) = H_m^{(1)}(R)$. The velocity of the wave front and the pitch of the helicon propagating in a quartz waveguide depend on the frequency of electromagnetic field, the electron plasma frequency, the amplitude of the polarization wave, and the topological charge. The critical value of the electromagnetic field intensity *I* at which we should take into account the nonlinear polarization of quartz glasses is at least $\sim 10^{12}$ W/cm^2 [7]. This means that helicons in an optical fiber can be observed at such field intensities.

REFERENCES

1. A. Yu. Loskutov and A. S. Mikhaĭlov, *An Introduction to the Synergetics* (Nauka, Moscow, 1990).
2. A. W. Snyder and J. D. Love, *Optical Waveguide Theory* (Chapman and Hall, London, 1983; Radio i Svyaz', Moscow, 1987).
3. M. Berry, in *Lecture Notes, Les Houches, Session 35, 1981* (North-Holland, Amsterdam, 1982), pp. 453–543.
4. E. Skudrzyk, *The Foundations of Acoustics: Basic Mathematics and Basic Acoustics* (Springer-Verlag, New York, 1971; Mir, Moscow, 1976), Vol. 2.
5. D. Rosas, C. T. Law, and G. A. Swartzlander, Jr., J. Opt. Soc. Am. B **14** (11), 3054 (1997).
6. Y. S. Kivshar, A. Nepomnyashchy, V. Tikhonenko, *et al.*, Opt. Lett. **25** (2), 123 (2000).
7. S. A. Akhmanov, V. A. Vysloukh, and A. S. Chirkin, *The Optics of Femtosecond Laser Pulses* (Nauka, Moscow, 1988).

Translated by A. Kondrat'ev

Technical Physics Letters, Vol. 28, No. 6, 2002, pp. 467–470. Translated from Pis'ma v Zhurnal Tekhnicheskoĭ Fiziki, Vol. 28, No. 11, 2002, pp. 51–57.
Original Russian Text Copyright © 2002 by Khomchenko, Sotsky, Romanenko, Glazunov, Kostyuchenko.

Determining Thin Film Parameters by Prism Coupling Technique

A. V. Khomchenko, A. B. Sotsky, A. A. Romanenko,
E. V. Glazunov, and D. N. Kostyuchenko
Institute of Applied Optics, National Academy of Sciences of Belarus, Mogilev, Belarus
e-mail: ipo@physics.belpak.mogilev.by

Received December 10, 2001

Abstract—A new method for determining the absorption coefficients, refractive indices, and thicknesses of thin films is proposed. The method is based on the measurement of the angular dependence of the energy reflection coefficient of a light beam upon excitation of the waveguide or leaky modes by a prism coupler. The features of determination of the parameters of SiO_x films on silicon and glass substrates are considered. *© 2002 MAIK “Nauka/Interperiodica”.*

Progress achieved in the field of controlled fabrication of thin-film structures [1] has made it possible to use the contact waveguide methods for determining the parameters of thin films. The corresponding techniques, based on measurements of the propagation constants of the waveguide modes excited in a thin film by a prism coupler, were described in [2, 3]. However, the originally proposed methods allowed only the refractive index and thicknesses of a thin film to be determined.

Below we report on the results of investigations showing new possibilities in determining the parameters of thin films with complex permittivity, which are offered by the prism coupling technique. The proposed approach is based on the measurement of the angular dependence of the energy reflection coefficient of a light beam upon excitation of the waveguide or leaky modes by a prism coupler, followed by reconstruction of the complex propagation constants using the results of these measurements.

Consider a thin film capable of guiding optical modes, which is situated on a substrate with a dielectric permittivity ε_s. Let the film contact the base of an equilateral prism as depicted in Fig. 1a. The prism with a base angle θ, the surrounding medium (atmosphere), and an air gap of thickness g between the prism and the waveguide are assumed to possess real permittivities ε_p, ε_a, and ε_g, respectively, such that $\varepsilon_p > \varepsilon_g \geq \varepsilon_a$. The structure is excited by a Gaussian light beam of radius w_0, with the beam axis making an angle γ with the normal to the entrance face of the prism. The energy reflection coefficient for the beam reflected from the prism is given by the formula $R(\gamma) = A(\gamma)r(\gamma)$, where $r(\gamma)$ is the coefficient of reflection from the prism base, $A(\gamma) = 16\kappa^2/(1+\kappa)^4$, $\kappa = (\varepsilon_p/\varepsilon_a)^T\cos\gamma/\sqrt{\varepsilon_p/\varepsilon_a - \sin^2\gamma}$, and $T = 0$ or 1 (for *TE* and *TM* polarization modes, respectively) [4].

Generalizing the results obtained in [5], we may conclude that the complex propagation constant h in the case of a resonance excitation of the guided mode can be restored from the experimental angular dependence $r(\gamma)$. For the dependence recorded in the angle interval $\gamma_0 - a \leq \gamma \leq \gamma_0 + a$, where γ_0 is the coordinate of minimum of the function $r(\gamma)$ corresponding to a given excited mode, the restoration formula is as follows:

$$h = \beta + \frac{\sin\alpha}{w}\{p_4^{(0)} + i[p_1 - p_2(1-\delta)^2(2\delta)^{-1}]\}. \quad (1)$$

Here, $\beta = k_0\sqrt{\varepsilon_p}\cos\alpha$, $\alpha = 0.5\pi - \theta + \arcsin(\sqrt{\varepsilon_a\varepsilon_p^{-1}}\sin\gamma_0)$,

$$\delta = (\varepsilon_p\varepsilon_g^{-1})^T\sqrt{(k_0^2\varepsilon_g - \beta^2)(k_0^2\varepsilon_p - \beta^2)},$$

$$w = w_0(\cos\gamma_0)^{-1}\sqrt{1 - \varepsilon_a\varepsilon_p^{-1}\sin^2\gamma_0},$$

and $k_0 = 2\pi/\lambda_0$ is the wave number in vacuum. The quantity p_1 is a root of the equation

$$[G(-p_1)]^{-1}\mathrm{Re}\int_0^{a_1} G\,dp_4 = \left(2a - \int_{\gamma_0 - a}^{\gamma_0 + a} r\,d\gamma\right)0.5k_0\sqrt{\varepsilon_a}w_0(1 - r_0)^{-1}, \quad (2)$$

where $G(t) = \frac{i}{\sqrt{2}}\int_{-\infty}^{\infty}\frac{\exp(-\tau^2)}{it - \tau\sqrt{2}}d\tau$, $t = -p_1 + ip_4$, $a_1 = k_0\sqrt{\varepsilon_a}w_0 a$, and $r_0 = r(\gamma_0)$. The values of $p_2 = |p_2|\exp(i\sigma)$,

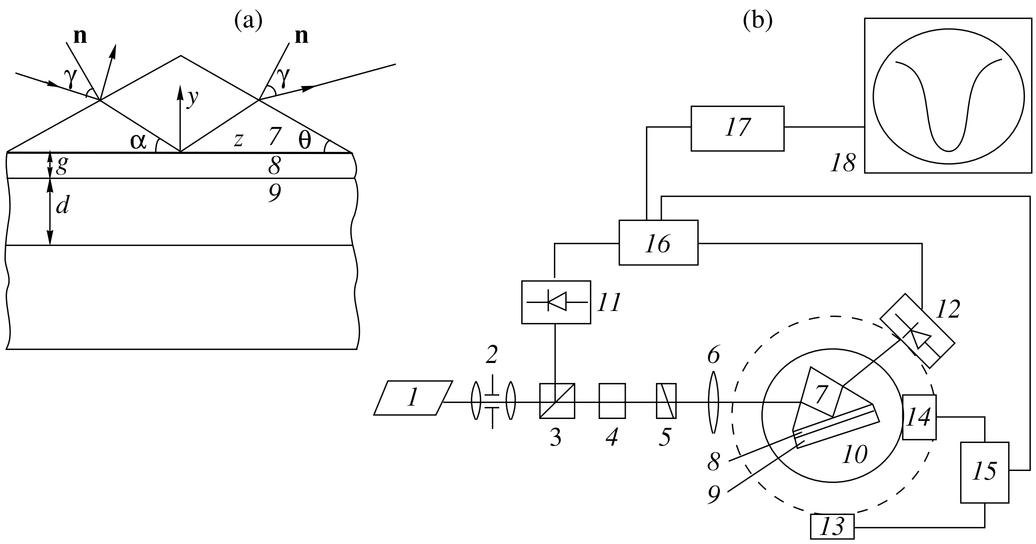

Fig. 1. Schematic diagrams of (a) a prism coupler and (b) an experimental setup used for recording the angular dependence of the light beam reflection coefficient: (*1*) radiation source; (*2*) collimator; (*3*) beam splitter; (*4*) attenuator; (*5*) polarizer; (*6*) lens; (*7*) prism; (*8*) gap; (*9*) thin-film structure; (*10*) rotary table; (*11*, *12*) photodetectors; (*13*, *14*) step motors; (*15*) synchronization control unit; (*16*) comparator; (*17*) analog-to-digital converter (ADC); (*18*) computer.

σ, and $p_4^{(0)}$ are calculated using the expressions

$$2|p_2| = -p_1 + (-1)^{\rho}\sqrt{p_1^2 + p_1\sqrt{0.5\pi}(1-r_0)[G(-p_1)]^{-1}}, \quad (3)$$

$$\sigma = k_0\sqrt{\varepsilon_a}w_0\left(\int_{\gamma_0}^{\gamma_0+a} r\,d\gamma - \int_{\gamma_0-a}^{\gamma_0} r\,d\gamma\right)N^{-1}, \quad p_4^{(0)} = \sigma P, \quad (4)$$

where $\rho = 0$ or 1, and

$$N = 8|p_2|\sqrt{\frac{2}{\pi}}\left\{\operatorname{Im}\int_0^{a_1} G\,dp_4 - \left(\frac{|p_2|}{p_1} + 1\right)[\operatorname{Re}G(-p_1 + ia_1) - G(-p_1)]P\right\},$$

$$P = [p_1 G(-p_1) + \sqrt{0.5\pi}] \times \{(1 + |p_2|p_1^{-1})[p_1\sqrt{0.5\pi} + (1 + p_1^2)G(-p_1)]\}^{-1}.$$

Using expression (1), it is possible to restore the complex mode propagation constants with an allowance for a perturbation introduced by the coupling prism into the structure studied, that is, the measured value of h is independent of the gap thickness determined by the force pressing the prism to the film. Upon substituting the h values for any of the two modes featured by the film into the corresponding dispersion equations, we can determine the refractive index n, the absorption coefficient k for $k(\varepsilon = (n + ik)^2)$, and the film thickness d [5].

For performing the angular measurements, we have designed and constructed an automated setup depicted in Fig. 1b. In this scheme, the Gaussian beam from a He–Ne laser ($\lambda_0 = 0.6328$ μm, $w_0 = 492$ μm) is incident onto a coupling prism *7* mounted on a rotary table *10*. The angle of incidence γ can be varied using a system driven by step motor *14*. In our experiments, the angular step of the table rotation was 20 sec of arc. The

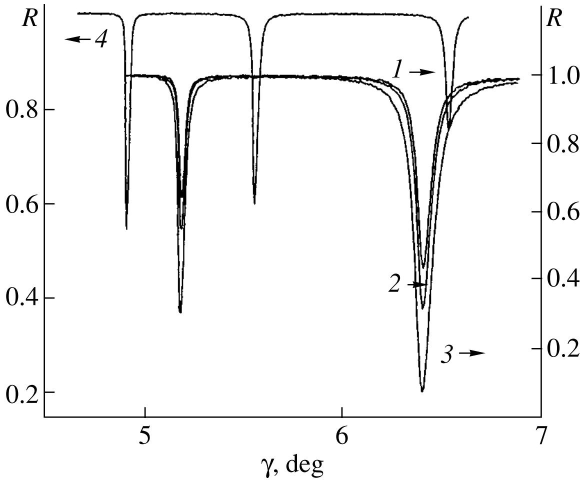

Fig. 2. Angular dependences of the light reflection coefficient measured for (*1*–*3*) a SiO$_x$–Si structure with increasing pressing load (right-hand *R* scale) and (*4*) a SiO$_x$–quartz glass structure (left-hand *R* scale).

Table 1. The results of processing angular dependences presented in Fig. 2 for a SiO$_x$ film on a Si substrate

Curve number	Reh_0^*	Reh_1^*	$\lvert \mathrm{Im} h_0^* \rvert \times 10^4$	$\lvert \mathrm{Im} h_1^* \rvert \times 10^4$
1	1.46489	1.46491	1.31	2.04
2	1.46488	1.46491	0.62	2.04
3	1.46490	1.46491	0.45	2.04

* h_0 and h_1 are the h values restored upon selecting ρ = 0 and 1 in Eq. (3), respectively.

angular dependence $r(\gamma)$ was determined with the aid of photodetector *12* (driven synchronously with the table by step motor *13* and measuring the power of a light beam reflected from the coupling prism device), photodetector *11* (measuring the incident beam power), and unit *16* comparing the two photodetector signals (unit *16* is synchronized with the step motor control unit *15*). The signal from comparator *16* was digitized in 10-digit ADC *17* and fed to computer *18* for storage, processing, and display.

We have studied the thin-film structures of two types, obtained by RF sputtering of a quartz glass (KV grade) in an argon–oxygen atmosphere (4 : 1, v/v) onto silicon (n_s = 3.515) or quartz (the same KV glass, n_s = 1.4567) substrates. Structures of the first type maintained only the leaky modes. The corresponding $R(\gamma)$ curves measured for various forces pressing the coupling prism to the substrate (and, hence, for the corresponding outgoing *TE* modes) are presented in Fig. 2 by curves *1–3* (increasing curve number corresponds to decreasing gap width g). The perturbation introduced by the coupling prism is manifested by the ambiguity of selecting ρ in expression (3) [5]. In practice, one has to chose one of the two values of the propagation constant (calculated as a result of processing of the experimental data), none of which can be rejected a priori. The results obtained upon processing curves *1–3* in Fig. 2 show that the h value corresponding to correct ρ is stable, whereas the other varies (Table 1). Using the h values measured for various leaky modes, we calculated the SiO$_x$ film parameters for a SiO$_x$ film on a Si substrate: $n = 1.47545$, $k = 1.6 \times 10^{-5}$, $d = 3.50$ μm. The rms errors of determining n, k, and d values were 1×10^{-5}, 0.1×10^{-5}, and 0.01 μm, respectively (for the errors of k_0^{-1} Reh and Imh measurements equal to 6×10^{-6} and 0.02|Imh|, respectively).

Structures of the second type (n_s = 1.4567) exhibited waveguide properties [6] and maintained three waveguide modes with the *TE* polarization (Fig. 2, curve *4*). The values of propagation constants measured for these waveguide modes and the corresponding calculated film parameters are listed in Table 2. The rms errors of k_0^{-1} Reh and k_0^{-1} Imh measurements were equal to 4×10^{-6} and 1.5×10^{-7}, respectively.

In order to check for correctness of the obtained results, the parameters of the waveguide films were determined by independent methods. The optical losses measured for the third mode with the aid of a fiber scanning along the waveguide [7] were 9.7 dB/cm (error, 0.3 dB/cm). The film thickness measured on a profilograph was 3.51 μm (error, 0.02 μm). As can be seen, these values agree with the calculated data presented in Table 2. Since the structures of both types were prepared in a single technological cycle, the sample parameters must be sufficiently close which is also confirmed by experiment.

An analysis of the results of experiments with the films featuring waveguide modes shows that the possibility of correct determination of the system parameters depends on the degree of localization of the mode fields which, in turn, depends on $\Delta n = n_s - n$ and on the film thickness d. For $\Delta n \geq 0.75$, the k values coincide (to within the relative error $\delta k/k = 0.03$) with the data for an analogous waveguide film. For $\Delta n < 0.75$, the $\delta k/k$ value varies with the film thickness: for $d \geq 3.5$ μm this ratio does not exceed 0.05 for SiO$_x$ films on a K8 optical glass substrate. The minimum value of k, which can be determined with an acceptable accuracy of measurements, is also determined by the outgoing mode losses. For a SiO$_x$ film with a thickness of 2.5 μm on a Si substrate, $\delta k/k$ = 0.1 and 0.03 for $k = 10^{-5}$ and 3×10^{-5}, respectively. The errors of determination of the refractive index and film thickness never exceeded 5×10^{-5} and 3%, respectively. Therefore, use of the proposed method for determining the absorption of thin films featuring only leaky modes is expedient only provided for a sufficiently large difference of refractive indices of the substrate and film (at least for $\Delta n > 0.5$). In the case of small Δn values, application of this method is expedient for the films with thicknesses $d \geq 5$ μm. It should

Table 2. The parameters of a waveguide SiO$_x$ film on a quartz glass substrate

Mode number	Reh/k_0	|Imh_0|, $\times 10^{-5}$	n	$k \times 10^{-5}$	d, μm
0	1.47335	1.57			
1	1.46720	1.49	1.47544	1.57	3.50
2	1.45785	1.15*	$\pm 1 \times 10^{-5}$	±0.03	±0.004

* The value corresponding to the optical losses of 9.91 dB/cm.

be noted that the proposed method can be used for the investigation of thin metal films guiding plasmon modes.

Thus, the proposed method of determining the parameters of thin layers can be of interest in the investigations of various thin-film structures used in optics, optoelectronics, and microelectronics.

REFERENCES

1. V. N. Sretenskiĭ and V. A. Yudinov, Zarubezhn. Radioélektron., No. 3, 69 (1996).
2. R. Ulrich and R. Torge, Appl. Opt. **12** (12), 2901 (1973).
3. T. W. Hou and C. J. Mogab, Appl. Opt. **20** (18), 3184 (1981).
4. A. B. Sotskiĭ, A. V. Khomchenko, and L. I. Sotskaya, Opt. Spektrosk. **78** (3), 502 (1995) [Opt. Spectrosc. **78**, 453 (1995)].
5. A. A. Romanenko and A. B. Sotskiĭ, Zh. Tekh. Fiz. **68** (4), 88 (1998) [Tech. Phys. **43**, 427 (1998)].
6. G. T. Petrovskiĭ, V. P. Red'ko, and A. V. Khomchenko, Zh. Tekh. Fiz. **54** (10), 2045 (1984) [Sov. Phys. Tech. Phys. **29**, 1199 (1984)].
7. R. Th. Kersten, Vak.-Tech. **23** (1), 16 (1973).

Translated by P. Pozdeev

Technical Physics Letters, Vol. 28, No. 6, 2002, pp. 471–474. Translated from Pis'ma v Zhurnal Tekhnicheskoĭ Fiziki, Vol. 28, No. 11, 2002, pp. 58–65.
Original Russian Text Copyright © 2002 by Bezruchko, Ivanov, Ponomarenko, Seleznev.

Experimental Study of Bifurcations in Systems with Rapidly Varying Parameters

B. P. Bezruchko, R. N. Ivanov, V. I. Ponomarenko, and E. P. Seleznev
Saratov Branch, Institute of Radio Engineering and Electronics, Russian Academy of Sciences, Saratov, Russia
e-mail: sbire@sgu.ru

Received December 3, 2001

Abstract—The period-doubling bifurcations in nonlinear circuits under conditions when the control parameter changes rapidly as compared to the oscillation relaxation process were experimentally studied. The choice of one of the two possible final states differing only in the phase of oscillations was determined. The results show that real systems with continuous time obey the laws of breakage of the probability symmetry of the postbifurcation states, which were previously established by numerical experiments in discrete systems. *© 2002 MAIK "Nauka/Interperiodica".*

Introduction. Originally, the term bifurcation (from Latin for "doubling") means splitting of the evolution pathway of a system that takes place when a control parameter of the system attains a certain critical level. In some cases, the two variants of the postbifurcation behavior are equiprobable. For example, having lost stability, a symmetric cycle exhibits a symmetry loss bifurcation and splits into two probabilistically identical mirror-symmetric cycles featuring oscillations with a double period, which differ only in phase. In this case, there arises a problem of choosing one of the two possible pathways under conditions where the control parameter varies at a finite rate in the presence of noise. This problem is related to basic phenomena such as the spontaneous symmetry breakage known in various natural sciences [1–3].

Below we present the results of observation of the aforementioned bifurcations in nonlinear oscillation circuits under conditions when a control parameter changes within a time shorter than a characteristic relaxation time of the system.

Depending on the conditions, there are two possible types of the bifurcation transitions in a system with noise: stochastic and dynamic [4–6]. The former type is realized in the limit of negligibly slow variation of the control parameter. Here, the choice of a postbifurcation (final) state is fully determined by noise. If the noise probability distribution is symmetric, the final states are probabilistically symmetric as well: $p_1 = p_2 = 1/2$. Transitions of the pure dynamic type are observed in the limit of negligibly small noise. In this case, either the first ($p_1 = 1$, $p_2 = 0$) or the second ($p_1 = 0$, $p_2 = 1$) final state is selected, depending on the initial conditions, with a unit probability that implies completely predictable behavior. In real systems, certain intermediate situations are realized in which both noise and the rate of the control parameter variation are significant. Nevertheless, a conditional boundary between stochastic and dynamic transitions can be defined using a criterion according to which the possible final state is attained at a preset probability (e.g., $p_1 = 0.75$, $p_2 = 0.25$).

Previously [6–8], the phenomenon of breakage of the probability symmetry of the final states in a system featuring dynamic bifurcations in the presence of noise was numerically modeled using a one-dimensional mapping of the type $x_{n+1} = f(x_n + \xi_n, r)$ with a quadratic function f, in which there were two possible variants of the periodic motion (differing only in phase) upon a period-doubling bifurcation. In this mapping, x_n is a dynamic variable, $n = 0, 1, \ldots, N$ is the discrete time, and ξ_n is the noise possessing zero mean ($\langle\xi\rangle = 0$), symmetric distribution, and the variance σ^2. The bifurcation (control) parameter r was assumed to vary as described by a piecewise linear function

$$r(n) = \begin{cases} r_1 + Sn, & n \le N, \\ r_1 + SN = r_2, & n > N. \end{cases} \qquad (1)$$

Here, S is the parameter variation rate determined as $S = \Delta r/N$, $\Delta r = r_2 - r_1$ is the total change in the control parameter, and N is the number of iterations corresponding to this change. The modeling aimed at determining the probability $p_{1,2}$ of the system falling into a given final state (with doubled oscillation period), depending on the noise variance σ^2 for various S values. The results were expressed in terms of a critical noise level σ_c^2, corresponding to a boundary between stochastic and dynamic transition scenarios, determined as a function of the parameter variation rate S.

It was demonstrated that the phenomenon of breakage of the probability symmetry of the final states under the conditions of fast period-doubling bifurcation in the

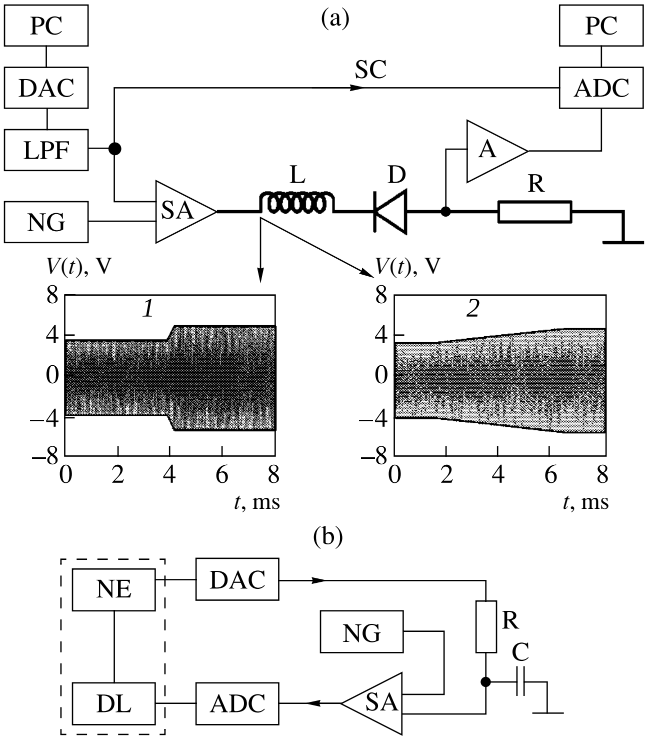

Fig. 1. Schematic diagrams of the experimental setups used to study the breakage of the probability symmetry of the postbifurcation states in (a) an oscillatory circuit with a semiconductor diode [arrows indicate typical shapes of the excitation signal for the cases of (*1*) high and (*2*) low rates of the control parameter variation] and (b) a ring circuit with a delayed feedback oscillator: (PC) personal computer; (DAC) digital-to-analog converter; (ADC) analog-to-digital converter; (LPF) digital low-pass filter; (NG) noise generator; (A) amplifier; (SA) summing amplifier; (SC) synchronization circuit; (NE) nonlinear element; (DL) delay line.

discrete models studied is determined by the boundaries of the basin of attractions of various final states in the phase space, which "move" in response to the control parameter variation [8]. When the parameter r changes within a small vicinity of the bifurcation (critical) value r_{c1}, the $\sigma_c^2(S)$ value is represented by a power function of the type $\sigma_c^2 \approx 2\gamma^2 S^2$, where $\gamma = (dx^*/dr)|_{rc1}$ is a factor characterizing the displacement of boundaries of the basin of attractions of the postbifurcation states. The purpose of this study was to experimentally confirm that real systems with continuous time obey the laws established previously for discrete models.

Experimental systems and procedures. The objects for investigation were as follows (Fig. 1): (a) a nonautonomous dissipative oscillator representing a nonlinear oscillatory diode circuit (diode resonator) comprising induction coil L, resistor R, and diode D (indicated by thick solid lines in Fig. 1a) and (b) a ring autooscillator system of the delayed feedback oscillator (DFO) type. We employed a mixed analog-digital oscillator scheme combining purely digital nonlinear element and delay line with analog filter *RC*, linked by analog-to-digital (ADC) and digital-to-analog (DAC) converters. This scheme allowed the system characteristics (the shape of nonlinear function $F(x)$ and the delay time τ) to be readily modified within broad limits while retaining the other parameters unchanged.

The scheme of the first experiment is depicted in Fig. 1a. The system was excited with a harmonic signal of the type $V(t) = V_0(t)\sin(\omega t)$, where $V_0(t)$ is the variable amplitude and ω is a circular frequency, which was generated by a personal computer linked to a DAC and an analog low-pass filter (LPF). The harmonic signal was fed into a summing amplifier together with a noise signal supplied from the corresponding generator. The noise was close to normal and possessed a zero mean in the working frequency range. The total signal was applied to a system studied via a decoupling amplifier. The control parameter was represented by the signal amplitude $V_0(t)$, which varied according to a piecewise linear law

$$V_0(t) = \begin{cases} V_{01} + St, & t \le T, \\ V_{01} + ST = V_{02}, & t > T. \end{cases} \qquad (2)$$

Here, V_{01} and V_{02} are the initial and final values of the parameter, S is the parameter variation rate determined as $S = \Delta V_0/T$, $\Delta V_0 = V_{02} - V_{01}$ is the total change in the control parameter, and T is the time for which this change takes place (for convenient comparison with the results of numerical modeling, the rate S was reduced to dimensionless form). The output voltage variation pattern was measured using an amplifier linked to an ADC (synchronized with the excitation signal from the master oscillator). Then a personal computer determined which of the two final oscillation states differing in phase (shifted in time by the period of oscillations) was established in the system upon a period-doubling bifurcation.

In experiments with the autooscillator system (Fig. 1b), the ring oscillator signal in the analog part was summed with a noise component supplied from a controlled noise generator. Here, the control parameter was represented by the coefficient r entering into the characteristics of the nonlinear element of DFO, which were selected in the form of either

$$F(x) = r - x^2 \qquad (3)$$

or

$$F(x) = -x(r + x). \qquad (4)$$

The cases of functions (3) and (4) differ in the character of the dependence of a stationary solution x^* of a period-1 cycle equation on the parameter r. For $F(x)$ given by formula (4), the derivative $\gamma = dx^*/dr = 0$ (the point x^* exhibits no shift in the one-dimensional phase space), whereas for (3) this derivative is nonzero ($\gamma > 0$). The parameter r varied in time according to the

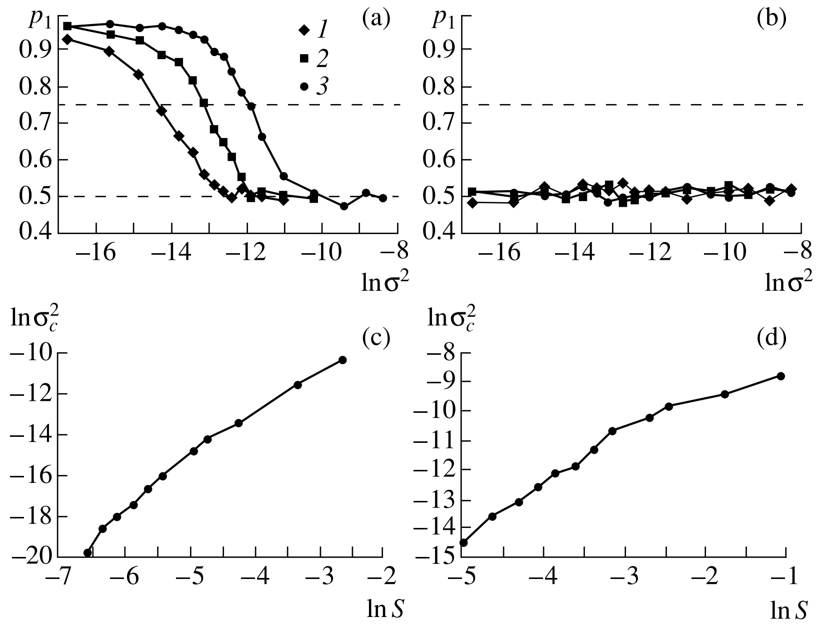

Fig. 2. (a, b) Plots of the probability p_1 of attaining a preset given final state versus noise intensity logarithm $\ln(\sigma_c^2)$ in the ring DFO system with nonlinear element characteristics of the type (3) and (4), respectively, for $S = 6.75 \times 10^{-3}$ (*1*), 13.5×10^{-3} (*2*), and 27×10^{-3} (*3*). (c, d) Experimental logarithmic plots of the critical noise level versus rate of the control parameter variation in a large ΔV interval for the diode resonator and the ring DFO system with a nonlinearity of type (3), respectively.

piecewise linear law (1). In the final stage, the postbifurcation state was determined as characterized by the phase shift of established double-period oscillations (relative to a reference signal).

Using the observed output voltage patterns, the probabilities $p_{1,2}$ of falling into one of the two possible final states were determined for all systems as functions of the noise variance σ^2 for various control parameter variation rates S. In order to accumulate a sufficient statistics, necessary for calculating mean probabilities with an error not exceeding 1%, 2000 experiments were run with each set of the noise variance and the parameter variation rate. Finally, the smoothed $p_{1,2}(\ln S)$ curves were used to determine the critical noise levels σ_c^2 as functions of S.

Results and discussion. The results of our experiments showed that, in the general case, both real systems studied exhibit the phenomenon of breakage of the probability symmetry of the final states, provided that the rate of variation of the control parameter is sufficiently high. Figure 2a presents typical experimental probabilities for a ring DFO system with a nonlinearity of type (3) to fall into a given final state, plotted versus the noise level for various control parameter variation rates. In the region of low rates of the control parameter variation, even a relatively low noise level leads to equiprobable final states. As the parameter variation rate grows, the dynamic processes become more pronounced and the results of the bifurcation transition become predictable.

By selecting a special shape of the nonlinear function F for the ring DFO system, it is possible to provide for conditions under which the symmetry is not broken even at high S values. Figure 2b shows the results of experiments in this system with a nonlinearity of type (4), when $\gamma = 0$. Under these conditions, the cycle does not change upon losing stability: the position of boundaries of the basin of attraction of the final states is independent of the control parameter, and the postbifurcation states remain equiprobable irrespective of the control parameter variation rate. This situation is impossible for the diode resonator circuit, since it is necessary to ensure that the cycle (having lost stability) would be independent of the control parameter in a three-dimensional phase space. We failed to provide for this condition by varying the circuit and excitation parameters.

The above results confirm a relationship between the appearance of asymmetry and the "motion" of boundaries of the basin of attractions corresponding to various final states in the phase space. This behavior is qualitatively similar to that observed for the quadratic mappings [8]. It should be noted that, in a broad range of the control parameter variation, the critical noise variance σ_c^2 (corresponding to a conditional boundary between stochastic and dynamic bifurcations) plotted as a function of S in the logarithmic coordinates is nonlinear (Figs. 2c and 2d). Therefore, this dependence is not described by a power function (in contrast to what was assumed in the original theoretical investigations of this phenomenon).

Acknowledgments. This study was supported by the Russian Foundation for Basic Research (project nos. 00-02-17441and 01-02-06372) and by the US Civilian Research and Development Foundation for the Independent States of the Former Soviet Union (CRDF Award no. REC-006).

REFERENCES

1. V. I. Gol'danskiĭ and V. V. Kuz'min, Usp. Fiz. Nauk **157** (1), 3 (1989) [Sov. Phys. Usp. **32**, 1 (1989)].
2. I. N. Zheludev, Usp. Fiz. Nauk **157** (4), 683 (1989) [Sov. Phys. Usp. **32**, 357 (1989)].
3. S. A. Akhmanov and A. S. Roshal', Izv. Vyssh. Uchebn. Zaved., Radiofiz. **4** (2), 203 (1961).
4. R. Kapral and P. Mandel, Phys. Rev. A **32** (2), 1076 (1985).
5. C. Baesens, Physica D (Amsterdam) **53** (2–4), 319 (1991).
6. O. Ya. Butkovskiĭ, J. S. Brush, Yu. A. Kravtsov, and E. D. Surovyatkina, Zh. Éksp. Teor. Fiz. **109** (6), 2201 (1996) [JETP **82**, 1186 (1996)].
7. O. Ya. Butkovskiĭ, Yu. A. Kravtsov, and E. D. Surovyatkina, Zh. Éksp. Teor. Fiz. **113**, 369 (1998) [JETP **86**, 206 (1998)].
8. B. P. Bezruchko and R. N. Ivanov, Pis'ma Zh. Tekh. Fiz. **26** (22), 7 (2000) [Tech. Phys. Lett. **26**, 982 (2000)].

Translated by P. Pozdeev

Technical Physics Letters, Vol. 28, No. 6, 2002, pp. 475–478. Translated from Pis'ma v Zhurnal Tekhnicheskoĭ Fiziki, Vol. 28, No. 11, 2002, pp. 66–74.
Original Russian Text Copyright © 2002 by Bulyarskii, Zhukov, Prikhod'ko.

Emission from Mn^{4+} Ions in Gadolinium Gallium Garnet at High Laser Pumping Intensities

S. V. Bulyarskii, A. V. Zhukov, and V. V. Prikhod'ko
Ul'yanovsk State University, Ul'yanovsk, Russia
e-mail: avg@ulsu.ru

Received October 17, 2001

Abstract—The $^4T_2 \longrightarrow {}^4A_2$ transition in Mn^{4+} ion is observed for the first time in the luminescence spectrum of a manganese-doped gadolinium gallium garnet $Gd_3Ga_5O_{12}:Mn^{4+}$ (GGG:Mn^{4+}) crystal under intensive laser pumping conditions. It is shown that an increase in intensity of the $^4T_2 \longrightarrow {}^4A_2$ transition as compared to that of the $^2E \longrightarrow {}^4A_2$ transition in the luminescence spectra of GGG:Mn^{4+} becomes possible because an increase in the pumping power leads to increasing contribution of the induced transitions. This process is more pronounced in the region of maximum overlap of the bands of $^2E \longrightarrow {}^4A_2$ and $^4T_2 \longrightarrow {}^4A_2$ transitions, which results in enhancement of the phononless line of the latter transition with a peak at 694 nm. It is suggested that GGG:Mn^{4+} can be used as a working element in continuously tunable lasers. © *2002 MAIK "Nauka/Interperiodica".*

Introduction. Transition metal impurities with the d^3 outermost electron shell configuration, such as Cr^{3+}, Mn^{4+}, and V^{2+}, still draw the interest of researchers engaged in the search for new materials to be used as active media in solid state lasers. A promising class of matrices for these impurities is offered by garnet crystals.

The most thoroughly studied d^3 impurity in the garnet structure is Cr^{3+} [1, 2]. The luminescence spectra of chromium contain two characteristic bands: the narrow R line (corresponding to the $^2E \longrightarrow {}^4A_2$ transition between terms of the Cr^{3+} ions) observed in the spectra of garnets at about 695 nm and a broad band in the region of longer wavelengths (the $^4T_2 \longrightarrow {}^4A_2$ transition). Which of the two transitions dominates depends on the crystal field strength [3].

The outermost electron shell structure of the Mn^{4+} ion is similar to that of Cr^{3+}. This fact accounts for the close optical properties. However, both luminescence and absorption spectra of the manganese ion exhibit certain distinctions from those of chromium [4–7]. One of such features is related to a greater value of the crystal field parameter (Dq) observed for Mn^{4+} ions in crystals with garnet structure [8]. For example, Mn^{4+} ions in gadolinium gallium garnet (GGG) are characterized by $Dq = 1960\ cm^{-1}$ (versus $Dq = 1585\ cm^{-1}$ for Cr^{3+} in the same matrix) [4]. A consequence of this (according to the Tanabe–Sugano diagram [3]) is that the $^2E \longrightarrow {}^4A_2$ transition dominates in the luminescence spectra of Mn^{4+}, while the $^4T_2 \longrightarrow {}^4A_2$ transition (typical of chromium in the same matrix) is virtually absent [2].

Below we demonstrate that, under certain conditions (at temperatures above 300 K and high pumping power), the relative intensity of the $^4T_2 \longrightarrow {}^4A_2$ transition increases. The main factors accounting for this change are (i) a difference in the temperature dependence of the probabilities of $^2E \longrightarrow {}^4A_2$ and $^4T_2 \longrightarrow {}^4A_2$ transitions and (ii) an increase in the induced radiation intensity.

Preparation of samples and analysis of the luminescence spectra measured at various temperatures and laser pumping levels. Manganese-doped gadolinium gallium garnet $Gd_3Ga_5O_{12}:Mn^{4+}$ (GGG:Mn^{4+}) samples were prepared as [111]-oriented plane-parallel plates with ground faces and with lateral dimensions of ~0.5 × 1 cm and a thickness of 0.5 mm. All samples were transparent in the visible spectral range. Some of the samples exhibited slight coloration, which was explained by the presence of uncontrolled color centers in the crystal lattice [9].

The concentration of Mn impurity in the samples was below 0.1 at.%. This circumstance allowed the complex formation effects (capable of inducing new lines in the luminescence spectra [10, 11]) to be excluded from the consideration.

The luminescence spectra were measured on SDL-2 and DFS-24 spectrometers. The spectra were excited by radiation of either a constant-wave YAG:Nd laser (with a wavelength of $\lambda = 532$ nm and a power of $P = 200$ W) or a pulsed-periodic copper vapor laser ($\lambda = 510.6$ nm; $P = 1000$ W; pulse repetition rate, $f = 8$ kHz; pulse duration, $\tau = 20$ ns). These lasers were selected because the radiation wavelengths fall within the

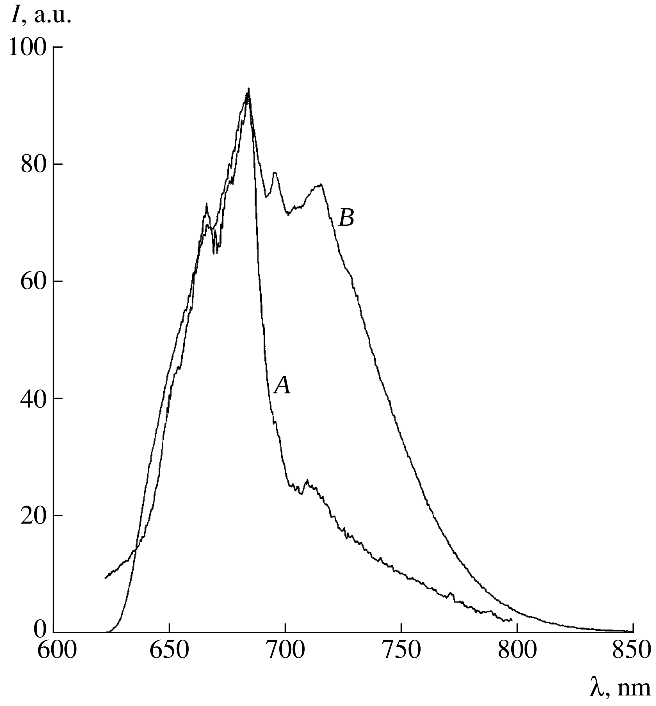

Fig. 1. The luminescence spectra of GGG:Mn^{4+} measured at 300 K and a laser pumping power of (*A*) P_L ~10 W/cm^2 and (*B*) P_L ~10^6 W/cm^2.

absorption band of Mn^{4+} corresponding to the $^4A_2 \longrightarrow$ $^4T_2$ transition [4]. The luminescence spectra were measured at several fixed temperatures in the range from 100 to 390 K. For this purpose, the samples were either mounted in a special holder in a cryostat (with a window ensuring the light beam striking the side face) or heated with a tungsten coil. The temperature was monitored with a copper–constantan thermocouple.

The luminescence spectra measured at room temperature with small laser pumping power per unit area (pumping power density, P_L ~ 10 W/cm^2) for all manganese-doped gadolinium gallium garnet samples display characteristic bands in the region of 650–700 nm (Fig. 1, curve *A*). According to [4, 12], this spectrum was identified as due to emission from Mn^{4+} ions in the GGG crystal matrix. The spectrum exhibits well-manifested features due to the $^2E \longrightarrow {}^4A_2$ transition, including the *R* line at 663.5 nm [4] and a band of complex structure in the region of longer wavelengths (with a maximum at 682 nm), which can be attributed to vibronic transitions.

The spectra measured for a high laser pumping power (P_L > 10 kW/cm^2) reveal a new maximum at 714 nm. No such peak was observed in [4], where the $^2E \longrightarrow {}^4A_2$ transition in Mn^{4+} was selectively excited. A comparison of the spectra *A* and *B* in Fig. 1 shows that this band (with a maximum at 710–714 nm) is present in the luminescence spectrum measured under usual conditions (i.e., for a low laser pumping level), but the peak intensity is small and cannot be distinguished from vibronic satellites of the *R* line [4–7]. Based on the analogy with the spectrum of trivalent chromium ion [2, 13, 14], it was suggested that the new peak belongs to the $^4T_2 \longrightarrow {}^4A_2$ transition of Mn^{4+} ion in GGG. Figure 1 (curve *B*) shows the luminescence spectrum of GGG:Mn^{4+} measured at a pumping power density of P_L ~ 10^6 W/cm^2. The $^4T_2 \longrightarrow {}^4A_2$ transition is manifested by a broad wavy band composed of weak equidistant peaks. The maximum at 694 nm, which is almost indistinguishable at a low pumping level, was attributed to the phononless line of the latter transition.

An analysis of the shape of the luminescence spectra of GGG:Mn^{4+} measured at various temperatures confirmed interpretation of the line peaked at 714 nm as belonging to the $^4T_2 \longrightarrow {}^4A_2$ transition. As the temperature increased, the spectral lines exhibited broadening and (beginning at 250–270 K) the integral intensity of the whole band sharply decreased (Fig. 2). This variation of the spectrum cannot be explained only by broadening and splitting (related, for example, to inhomogeneity of the crystal [15, 16]) of the band belonging to the $^4T_2 \longrightarrow {}^4A_2$ transition.

The sharp drop in the integral luminescence intensity beginning at ~250–270 K is indicative of a temperature-activated character of the nonradiative transitions [17]. Figure 3 shows the experimental plots of the integral intensity of the $^2E \longrightarrow {}^4A_2$ and $^4T_2 \longrightarrow {}^4A_2$ transitions versus temperature in comparison with the temperature dependences of the lifetime of the ^2E level [5]. In the region close to room temperature, there is a sharp (but not equal) increase in the intensity of both transitions. Taking into account the observed temperature-induced variation of the luminescence spectrum, redistribution of the room-temperature intensities of the $^2E \longrightarrow {}^4A_2$ and $^4T_2 \longrightarrow {}^4A_2$ transitions observed for increased pumping power density can be explained by the laser beam heating of the samples. However, an analysis of the spectra measured at various temperatures for a high pumping power density (P_L ~ 10^6 W/cm^2) showed that the laser heating effect cannot completely account for the redistribution of intensities of the $^2E \longrightarrow {}^4A_2$ and $^4T_2 \longrightarrow {}^4A_2$ transitions observed upon changing the laser pumping power. The plots of the integral intensities versus temperature differed from those presented in Fig. 3 only by a 21 and 19 K shift in the temperature axis for the $^2E \longrightarrow {}^4A_2$ and $^4T_2 \longrightarrow {}^4A_2$ transitions, respectively. In addition, there was an increase in intensity of the narrow peak at 694 nm (assigned to the phononless line of the latter transition).

Figure 4 shows plots of the integral intensities of the $^2E \longrightarrow {}^4A_2$ and $^4T_2 \longrightarrow {}^4A_2$ transitions and the phononless line of the $^4T_2 \longrightarrow {}^4A_2$ transition versus pumping power density. Data for the phononless line refer to the peak intensity obtained after approximation and back-

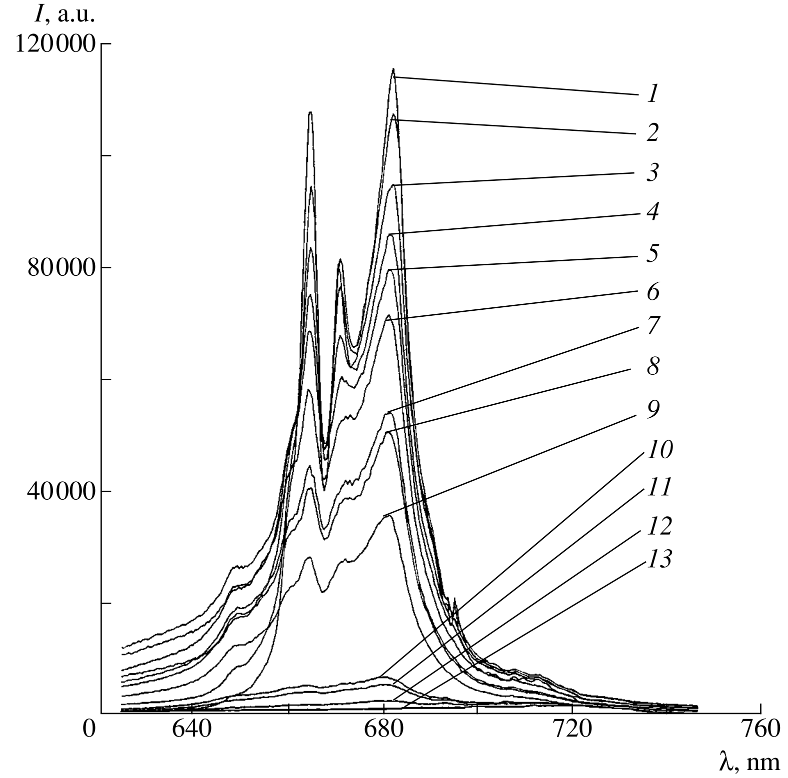

Fig. 2. The luminescence spectra of GGG:Mn^{4+} excited by a YAG:Nd laser and measured at various temperatures: (*1*) 100; (*2*) 125; (*3*) 150; (*4*) 175; (*5*) 200; (*6*) 225; (*7*) 250; (*8*) 260; (*9*) 270; (*10*) 285; (*11*) 300; (*12*) 330; (*13*) 390 K.

ground subtraction. The behavior observed is indicative of saturation of the $^4T_2 \longrightarrow {}^2E \longrightarrow {}^4A_2$ channel and of an increase in intensity of the transitions from the term $^4T_2$ directly to the ground term $^4A_2$. Indeed, according to [4], the term ^2E is characterized by a large lifetime ($\tau = 1.2$ ms at $T = 77$ K).

An increase in the peak intensity of the phononless line, as well as a nonlinear character of variation of the

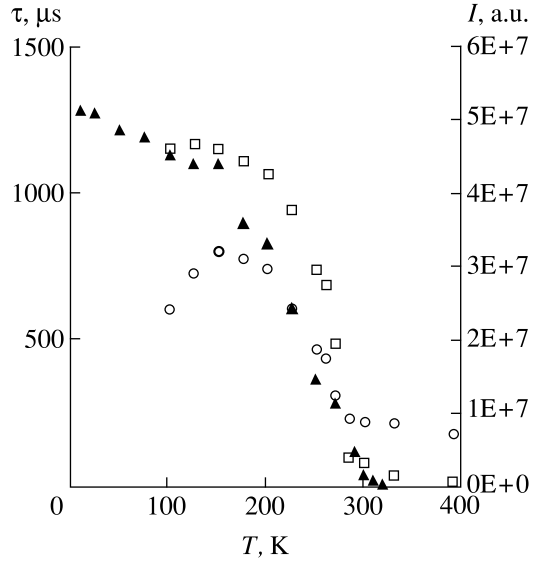

Fig. 3. Temperature dependences of the integral intensities of the $^2E \longrightarrow {}^4A_2$ (squares) and $^4T_2 \longrightarrow {}^4A_2$ (circles) transitions and the lifetime of the ^2E level (triangles, data from [4]).

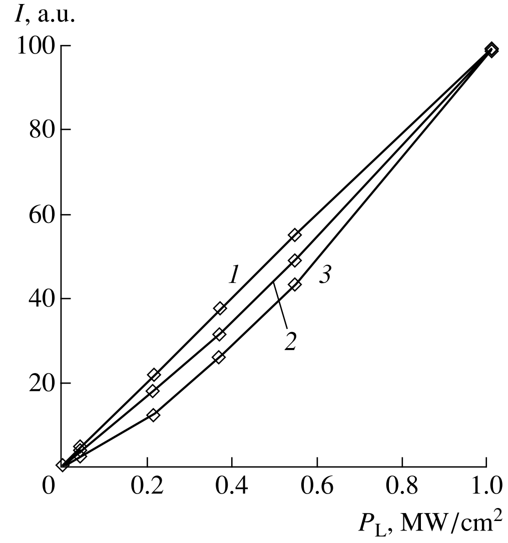

Fig. 4. Normalized plots of the integral intensities versus pumping power density: (*1*) $^2E \longrightarrow {}^4A_2$ transition; (*2*) $^4T_2 \longrightarrow {}^4A_2$ transition; (*3*) phononless line of the $^4T_2 \longrightarrow {}^4A_2$ transition.

integral intensity of the $^4T_2 \longrightarrow {}^4A_2$ transition depending on the pumping power density suggest that these effects are manifestations of the induced optical transitions. The $^4T_2 \longrightarrow {}^4A_2$ emission is caused both by transition from the same term and by the more intensive transitions $^2E \longrightarrow {}^4A_2$. This is possible owing to a considerable overlap of the spectral bands of the two transitions. Note that the overlap is more pronounced in the vicinity of the phononless line of the $^4T_2 \longrightarrow {}^4A_2$ transition than in the long-wavelength range, which probably accounts for the greater induced emission observed for the phononless line.

Conclusion. The $^4T_2 \longrightarrow {}^4A_2$ transition in Mn^{4+} ion was observed for the first time in the luminescence spectrum of a GGG:Mn^{4+} crystal, which is especially pronounced under intensive laser pumping conditions. The transition was identified based on the comparison of the luminescence spectrum of GGG:Mn^{4+} to that of Cr^{3+} ion, for which this transition is observed both in GGG and in other garnets in the region of longer wavelengths relative to the *R* line.

It was shown that an increase in intensity of the $^4T_2 \longrightarrow {}^4A_2$ transition in the luminescence spectra of GGG:Mn^{4+} is possible owing to an increase in the role of induced transitions as a result of increasing pumping power. This process is more pronounced in the region of maximum overlap of the $^2E \longrightarrow {}^4A_2$ and $^4T_2 \longrightarrow {}^4A_2$ transitions, which results in enhancement of the phononless line of the latter transition.

The observed significant homogeneous broadening of the *R* line probably makes possible the use of GGG:Mn^{4+} as a working element of solid-state lasers with continuous frequency tuning.

REFERENCES

1. M. Yamaga and B. Henderson, Phys. Rev. B **46** (6), 3273 (1992).
2. U. Hoemmerich and K. L. Bray, Phys. Rev. B **51** (18), 12133 (1995).
3. J. F. Donegan, T. J. Glynn, and C. F. Imbusch, J. Lumin. **36** (2), 93 (1986).
4. A. Brenier, A. Suchocki, C. Pedrini, *et al.*, Phys. Rev. B **46** (6), 3219 (1992).
5. A. Suchocki, M. Potemski, A. Brenier, *et al.*, J. Appl. Spectrosc. **62** (5), 181 (1995).
6. B. R. Jovanic, J. Lumin. **75** (1), 171 (1997).
7. L. A. Riseberg and M. J. Weber, Solid State Commun. **9** (11), 791 (1971).
8. I. B. Bersuker, in *Spectroscopy of Crystals* (Nauka, Leningrad, 1973), pp. 22–32.
9. G. J. Pogatsnik, L. S. Cain, Y. Chen, *et al.*, Phys. Rev. B **43** (2), 1787 (1991).
10. M. Kh. Ashurov, Yu. K. Voron’ko, V. V. Osiko, *et al.*, in *Spectroscopy of Crystals* (Nauka, Leningrad, 1978), pp. 55–67.
11. E. G. Valyashko, S. V. Grum-Grzhimaĭlo, I. M. Kutovoĭ, *et al.*, in *Spectroscopy of Crystals* (Nauka, Moscow, 1966), pp. 55–67.
12. O. N. Boksha and S. V. Grum-Grzhimaĭlo, *Spectroscopy of Crystals* (Nauka, Moscow, 1970).
13. A. Monteil, M. Ferrari, and F. Rossi, Phys. Rev. B **43** (4), 3646 (1991).
14. B. Struve and G. Huber, Appl. Phys. B **36**, 195 (1985).
15. A. A. Kaplyanskiĭ, S. P. Feofilov, and R. I. Zakharchenya, Opt. Spektrosk. **79** (5), 709 (1995) [Opt. Spectrosc. **79**, 653 (1995)].
16. S. V. Bulyarskii, A. E. Kozhevin, S. N. Mikov, *et al.*, Phys. Status Solidi A **180** (2), 408 (2000).
17. S. V. Bulyarskiĭ and N. S. Grushko, *Generation-Recombination Processes in Active Elements* (Mosk. Gos. Univ., Moscow, 1995).

Translated by P. Pozdeev

Technical Physics Letters, Vol. 28, No. 6, 2002, pp. 479–482. Translated from Pis'ma v Zhurnal Tekhnicheskoĭ Fiziki, Vol. 28, No. 11, 2002, pp. 75–83.

Dispersion Characteristics of the Surface Electromagnetic-Spin Waves in Ferrite–Ferroelectric–Dielectric–Metal Structures

V. E. Demidov[a],*, B. A. Kalinikos[a], S. F. Karmanenko[a],
A. A. Semenov[a], and P. Edenhofer[b],**
[a] *St. Petersburg State Electrotechnical University, St. Petersburg, Russia*
** e-mail: eivt@eltech.ru*
[b] *Institute for High-Frequency Technique, University of Bochum, D-44780 Bochum, Germany*
*** e-mail: edh@hf.ruhr-uni-bochum.de*
Received November 19, 2001

Abstract—Dispersion characteristics of the surface hybrid electromagnetic-spin waves propagating in a layered structure comprising a ferrite film on a ferroelectric plate and a metal screen at a certain distance from the ferroelectric plate surface were experimentally studied. The experimental data are compared to the results of calculations performed within the framework of a previously developed theory. The theoretical and experimental dispersion characteristics show good coincidence. *© 2002 MAIK "Nauka/Interperiodica".*

Investigations of hybrid electromagnetic-spin waves propagating in layered ferrite–ferroelectric structures, which were initiated by Afinogenov *et al.* [1–4], offer good prospects for creating microwave devices which can be continuously tuned by applied electric field [5]. The passage from the conventional spin-wave devices, where the working parameters are controlled by a constant magnetic field, to systems with the electric-field-controlled permittivity of a ferroelectric layer provides for a significant increase in the device characteristics. In comparison to spin wave devices based on ferrite films, the new structures implementing structures of the ferrite–ferroelectric type are characterized by a significantly higher tuning rate, lower energy consumed for the control, and smaller dimensions. At present, the study of wave processes in the layered ferrite–ferroelectric structures is especially important in view of the successful attempts at growing high-quality ferroelectric films on polycrystalline [6] and single crystal [7] ferrite surfaces.

Previously [8, 9], we developed a general theory of electromagnetic–spin waves (EMSWs) propagating in layered ferrite–ferroelectric structures. Within the framework of this theory, the layered structure geometry was analyzed from the standpoint of providing optimum conditions for controlling the dispersion characteristics of EMSWs by changing the permittivity of the ferroelectric layer. It was shown that the most promising results are expected from devices employing hybrid EMSWs propagating in layered structures comprising a ferrite film on a ferroelectric plate and a metal screen at a certain distance from the ferroelectric plate surface. Theoretically, the maximum control efficiency corresponds to the case when the frequency range of nonexchange surface magnetostatic spin waves is close to the cutoff frequency of the first thickness mode TE_1 of the transverse electromagnetic waves. The cutoff frequency of the TE_1 mode is determined by parameters of the ferroelectric layer and by the spacing between ferroelectric surface and metal screen. In the particular case of an unscreened ferrite–ferroelectric structure, this frequency is zero.

Despite numerous theoretical papers devoted to hybrid EMSWs (see [9] and references therein), only a few experimental investigations were reported. These were [1, 3, 4], where the hybridization of electromagnetic modes in a ferroelectric waveguide with the backward volume [4] and surface [1, 3] spin waves was studied. In those experiments, the wave process was observed under the conditions of weak hybridization, whereby the ferroelectric waveguide was removed far from the ferrite film surface. Under such conditions, the hybridization was manifested by a narrow absorption peak in the amplitude–frequency characteristic, near a point corresponding to intersection of the dispersion curves of the electromagnetic and spin waves. In addition, the dispersion characteristics of the hybrid waves were measured for decreasing spacing between the ferroelectric waveguide and the ferrite film [3]. However, the measurements were performed in a narrow range of frequencies and wavenumbers (in the vicinity of the point of intersection of the dispersion curves), while the influence of a metal screen on the dispersion of hybrid waves was not studied at all. Moreover, no experimental results have been reported to the present which

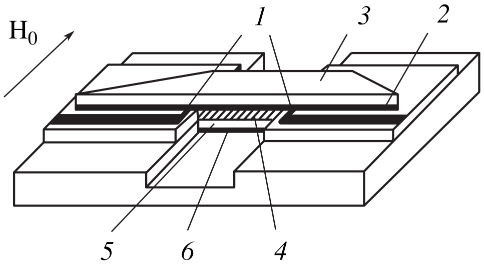

Fig. 1. Schematic diagram of the experimental device. See the text for explanations.

would allow verification of the previously developed theories describing hybrid EMSWs.

In this context, we have experimentally studied the dispersion characteristics of the surface hybrid EMSWs propagating in a layered structures of the ferrite–ferroelectric–dielectric–metal (FFDM) type and compared the experimental data to the results of calculations so as to assess the adequacy of the previously developed theory of hybrid EMSWs.

The surface EMSWs were studied in a device schematically depicted in Fig. 1. The device comprises two microstrip transmission lines terminating in two short-circuited spin wave transducers *1* with a width of 50 μm and a length of 3 mm. The distance between transducers is 7 mm. An iron yttrium garnet (IYG) film *2* with a thickness of L =16.5 μm and a width of 3 mm, grown on a gallium gadolinium garnet (GGG) substrate *3* with a thickness of 500 μm, is placed above the transducers. A layered structure comprising ferroelectric plate *4*, dielectric spacer *5* (with a thickness d), and metal screen *6* is pressed to the ferrite film from below with the aid of special clamps. The ferroelectric plate was cut from a bulk sample of barium strontium titanate ($Ba_{0.6}Sr_{0.4}TiO_3$) ceramics. The plate is 3 mm wide, 4.5 mm long, and has a thickness of a = 315 μm. This measuring device was placed into a constant magnetic field H_0 oriented parallel to the transducers.

The system described above operates as follows. The input transducer excites a magnetostatic surface spin wave (MSSW) which propagates in the ferrite film, enters the layered FFDM structure, and converts into a hybrid EMSW. Then the wave exhibited the inverse transformation and the resulting wave was received by the output transducer.

The dispersion characteristics of EMSWs were obtained in two steps. First, the dispersion characteristic of MSSWs was determined with the ferroelectric–dielectric–metal structure removed. For this purpose, the phase–frequency characteristic was measured and the frequency dependence of the group velocity was calculated from the slope of this curve. The absolute wavenumbers were determined under the condition that the frequency corresponding to the beginning of the transmission band in the amplitude–frequency characteristic corresponds to zero wavenumber. During the data processing, the wavenumbers of MSSWs were refined by fitting the experimental dispersion curve to the theoretical one calculated using the Damon–Eshbach formula [10]. In the second step, the phase–frequency characteristic was measured with the ferroelectric–dielectric–metal structure gradually approaching the ferrite film surface up to their close contact with pressing. In the course of this process, variation of the frequencies of the characteristic points on the phase–frequency characteristic (for which the absolute wavenumbers were determined in the first step) was traced. As a result, we obtained the dispersion curve for waves propagating sequentially in the ferrite film, then in the FFDM structure, and in the ferrite film again. The required dispersion characteristic of hybrid EMSWs propagating in the FFDM structure studied was obtained from the two dispersion curves with an allowance for the distances traveled by the wave in the free ferrite film and in the FFDM structure.

Figure 2 (points) shows the dispersion characteristics measured for various values of the magnetic field strength H_0 (indicated at the curves). The two parts of this figure correspond to the cases when (a) the metal screen is situated immediately on the surface of the ferroelectric plate and (b) when the screen is removed. Filled symbols refer to the MSSWs observed in the free ferrite film with the ferroelectric plate removed, while open symbols represent data for the EMSWs propagating in the layered structure. Solid curves in Fig. 2 show the dispersion curves of MSSWs calculated using the Damon–Eshbach formula, while the dashed curves represent the results of calculations according to the formulas derived in our theory for hybrid waves [9]. The theoretical dispersion curves of hybrid waves were calculated for a ferroelectric ceramic with the permittivity $\varepsilon_a = 2600$. This value was determined by measuring the capacitance of a flat capacitor formed on a ferroelectric plate analogous to that used in the experimental FFDM structure.

As can be seen from Fig. 2, a significant deviation of the dispersion curve of hybrid waves in the metal-screened ferroelectric plate from that of MSSWs in the course of H_0 growth is manifested when the frequency range of the spin waves shifts to the cutoff frequency of the electromagnetic TE_1 mode (in our case, 4700 MHz). In the case of a free ferroelectric plate, this deviation increases gradually because the TE_1 cutoff frequency is zero. As the frequency range of the spin waves shifts above the cutoff frequency of the TE_1 mode, the spectrum becomes bimodal and, hence, the MSSW energy is spent for the excitation of waves corresponding to both branches of the hybridized dispersion curves. This is manifested by the onset of interference in the initial portion of the transmission band, which hinders measurements of the hybrid wave dispersion in the interval of frequencies corresponding to small wavenumbers

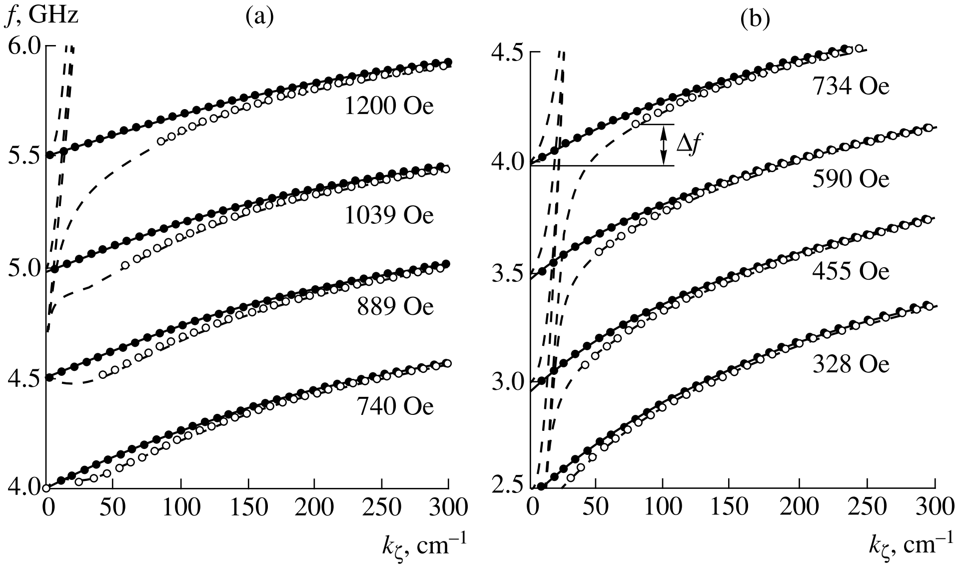

Fig. 2. The experimental and theoretical dispersion characteristics determined for various values of the magnetic field strength H_0 (indicated at the curves). See the text for explanations.

(Δf interval in Fig. 2b). As the field strength H_0 increases, the latter frequency interval expands.

A comparison of the experimental data to the results of theoretical calculations shows good coincidence in the regions corresponding to small frequencies. As the wavenumber increases, the experimental dispersion curves deviate from the theoretical. The theory predicts a stronger hybridization as compared to that observed in the experiment. This behavior can be explained by nonideality of the contact between ferrite and ferroelectric layers, which leads to a thin air gap between the two surfaces. The long spin waves, for which the electromagnetic field amplitude slowly decays with the distance from the ferrite surface, are less sensitive to this air gap. On the contrary, the field amplitude of the short spin waves drops sharply over a distance of several hundred microns. In this case, the presence of the air gap results in a significant decrease of the field penetration into the ferroelectric and, hence, in a weaker hybridization between spin waves and electromagnetic modes of the ferroelectric plate.

The dispersion characteristics of hybrid EMSWs were determined for several intermediate values of the dielectric spacer thickness (d = 110, 220, and 330 μm). These cases also demonstrated a good agreement between experimental and theoretical curves. In the course of experiments, the cutoff frequency of the electromagnetic TE_1 modes for each value of the dielectric layer thickness was determined at the onset of increase in the wavenumber of the hybrid waves corresponding to the beginning of the transmission band. The results of these measurements are represented by points in Fig. 3, where a solid curve shows the results of theoretical calculations. As can be seen from this comparison, there is a good agreement between theory and experiment for small d values. As the distance to the metal screen increases, there appears a certain misfit. This behavior can be explained by the existence of leakage electromagnetic fields related to finite lateral dimensions of the layered structure, which were not taken into account in the theory. As the dielectric gap width grows, the thickness of the layered structure becomes comparable to the width and, hence, the influence of the leakage fields on the hybrid wave properties increases.

The results of this study indicate that the theory of hybrid electromagnetic-spin waves developed previously [9] describes the propagation of such waves in

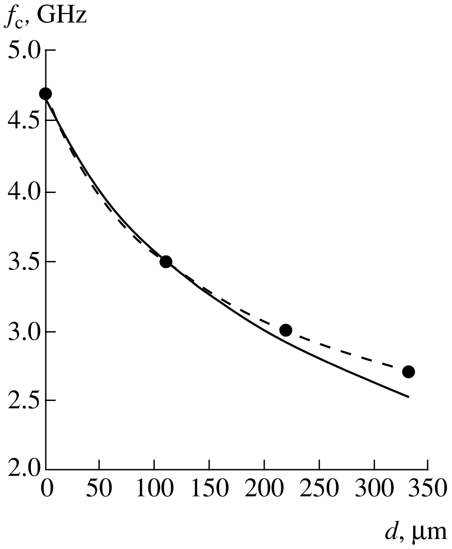

Fig. 3. The experimental and theoretical plots of the cutoff frequency f_c of the electromagnetic TE_1 mode versus distance from the ferroelectric plate to the metal screen.

layered structures of the ferrite–ferroelectric–dielectric–metal type with a good precision.

Acknowledgments. This study was supported by the Russian Foundation for Basic Research (project no. 99-02-16370), the INTAS Foundation (grant no. 99-1812), and Deutsche Forschungsgemeinschaft (grant DFG 2001).

REFERENCES

1. V. B. Anfinogenov, T. N. Verbitskaya, Yu. V. Gulyaev, *et al.*, Pis'ma Zh. Tekh. Fiz. **12** (15-16), 938 (1986) [Sov. Tech. Phys. Lett. **12**, 389 (1986)].
2. V. B. Anfinogenov, T. N. Verbitskaya, Yu. V. Gulyaev, *et al.*, Radiotekh. Élektron. (Moscow) **34** (3), 494 (1989).
3. V. B. Anfinogenov, T. N. Verbitskaya, Yu. V. Gulyaev, *et al.*, Radiotekh. Élektron. (Moscow) **35** (2), 320 (1990).
4. V. B. Anfinogenov, T. N. Verbitskaya, P. E. Zil'berman, *et al.*, Zh. Tekh. Fiz. **60** (9), 114 (1990) [Sov. Phys. Tech. Phys. **35**, 1068 (1990)].
5. V. Demidov, P. Edenhofer, and B. Kalinikos, Electron. Lett. **37** (19), 1154 (2000).
6. Q. X. Jia, J. R. Groves, P. Arendt, *et al.*, Appl. Phys. Lett. **74** (11), 1564 (1999).
7. W. J. Kim, W. Chang, S. B. Qadri, *et al.*, Appl. Phys. A **71** (1), 7 (2000).
8. V. E. Demidov and B. A. Kalinikos, Zh. Tekh. Fiz. **71** (2), 89 (2001) [Tech. Phys. **46**, 219 (2001)].
9. V. E. Demidov, B. A. Kalinikos, and P. Edenhofer, Zh. Tekh. Fiz. **72** (3), 61 (2002) [Tech. Phys. **47**, 343 (2002)].
10. R. W. Damon and J. R. Eshbach, J. Phys. Chem. Solids **19** (3/4), 308 (1961).

Translated by P. Pozdeev

Technical Physics Letters, Vol. 28, No. 6, 2002, pp. 483–485. Translated from Pis'ma v Zhurnal Tekhnicheskoĭ Fiziki, Vol. 28, No. 11, 2002, pp. 84–90.
Original Russian Text Copyright © 2002 by Davidenko, Ishchenko.

Electroluminescence of New Dyed Polymer Films in Sandwich Structures

N. A. Davidenko and A. A. Ishchenko
Kiev National University, Kiev, Ukraine
e-mail: daviden@ukrpack.net
Institute of Organic Chemistry, National Academy of Sciences of Ukraine, Kiev, Ukraine
e-mail: alexish@i.com.ua

Received January 16, 2002

Abstract—Electroluminescence (EL) from sandwich structures with emitting layers based on poly(*N*-epoxypropylcarbazole) (PEPC) doped with a boron difluoride organic dye complex was discovered and studied. The EL is implemented in heterostructures with Al- or In-based injecting heterojunctions possessing better technological properties as compared to those of conventional magnesium–silver electrodes. It is established that EL is controlled by the bulk recombination of charge carriers, whereby dye molecules act as the recombination centers. The EL efficiency is maximum in systems with a 50 mass % dye content in a submicron polymer film. The growth in EL quenching with an increase in the polymer film thickness is related to accumulation of the bulk space charge within a short time after the application of electric field. *© 2002 MAIK “Nauka/Interperiodica”.*

Developing new materials based on organic polymer films for electroluminescent devices is currently an important task because of high practical demands and considerable problems encountered in the use of existing materials [1–3]. In order to reproduce the electroluminescence (EL) effect, it is necessary to satisfy several requirements providing for (i) the effective injection of charge carriers from electric contacts into an organic polymer film, (ii) the transport of carriers to the recombination centers in the bulk of a polymer, and (iii) the recombination of carriers accompanied by the emission of light quanta.

The main problems in meeting these requirements are related to selecting the proper contact materials and providing conditions for effective transport of carriers without trapping in the polymer film bulk and effective radiative recombination. The well-known EL devices based on sandwich heterostructures employ for the most part separate transport and emitting polymer layers and magnesium–silver cathodes, the fabrication of which requires a complicated technology.

Below we present the results of investigations directed toward the creation and characterization of new electroluminescent materials and compositions, in particular, the films of poly(*N*-epoxypropylcarbazole) (PEPC) doped with a boron difluoride organic dye (BFI) complex (Fig. 1).

The experiments were performed on samples of sandwich structures comprising a glass substrate, a transparent conducting SnO_2:In_2O_3 (ITO) film, a dyed polymer layer (PEPC + *N* mass % BFI), and an aluminum electrode. The dye concentration *N* was varied from 1 to 70 mass %. The PEPC + *N* mass % BFI films were obtained by casting a chloroform solution containing corresponding amounts of PEPC and BFI onto ITO-coated glass substrates, followed by drying in a thermal box for 3 h at 80°C. The polymer film thickness *L* was varied from 0.5 to 5 μm. The metal contacts were applied onto the polymer film by deposition in vacuum.

The spectra of absorption, photoluminescence (PL), and electroluminescence of the PEPC + *N* mass % BFI films were measured in the wavelength range from 400 to 1000 nm. The electric current density (j) and the integral EL intensity (I_{EL}), observed on the side of the ITO film upon the application of voltage to the electric contacts of the sandwich structure, were studied as functions of the magnitude and polarity of the electric voltage (U) applied to the contacts, time after switching on the voltage, and the polymer film thickness. All mea-

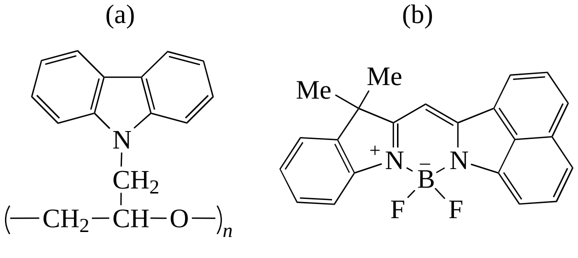

Fig. 1. The structure of components of a photoconducting polymer system studied: (a) poly(*N*-epoxypropylcarbazole) (PEPC); (b) boron difluoride organic dye (BFI).

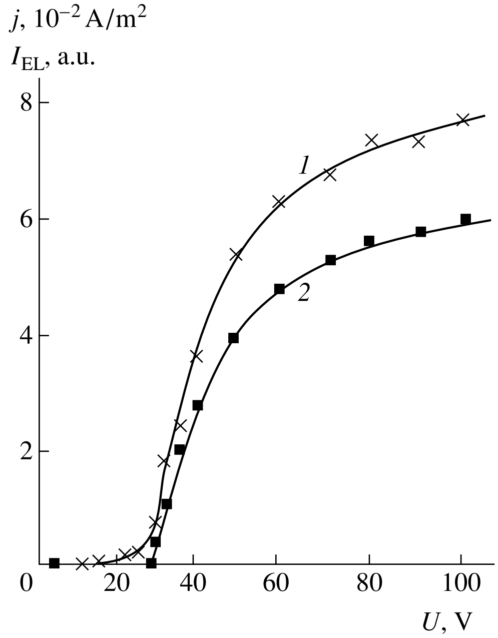

Fig. 2. The plots of (*1*) current density j and (*2*) electroluminescence intensity I_{EL} versus applied voltage for an ITO–(PEPC + 50 mass % BFI)–Al structure with $L = 0.7$ μm (measured for negative polarity of the Al electrode).

surements were performed at room temperature in air under normal conditions.

The samples of the ITO–PEPC–Al sandwich structure with a dye-free PEPC layer possess low electric conductivity, do not show the EL effect, and exhibit optical absorption in the region of $\lambda < 400$ nm. In contrast, the ITO–(PEPC + N mass % BFI)–Al heterostructures are characterized by a significant electric conductivity which increases with the dye content N. The optical absorption in the visible spectral range is determined by the electronic absorption of BFI showing a pronounced vibrational structure. When the BFI content increases above 1 mass %, the vibrational structure exhibits considerable smoothening, while the absorption band broadens and shifts toward longer wavelengths. As the dye concentration N varies from 1 to 50 mass %, the wavelength corresponding to maximum absorption changes from 530 to 510 nm, while the fluorescence peak shifts from 612 to 638 nm. This is evidence of the molecular interactions arising in the polymer–dye system, with aggregation of dye molecules in the limiting case [4].

An increase of the BFI content in the ITO–(PEPC + N mass % BFI)– Al structure leads to the appearance of EL. The PL and EL spectra coincide. After application of the voltage U, the I_{EL} value rapidly reaches maximum and then gradually (within a few seconds or faster) decreases to attain a stationary level. The rate of this decay and the difference between maximum and quasi-stationary I_{EL} values increase with the voltage magnitude. Analogous trends are observed in the behavior of the current density j as a function of U and t. However, both the rate of I_{EL} decay after switching on the voltage and the relative difference between maximum and quasi-stationary EL levels are greater than the analogous characteristics for the current density. After switch-off the voltage, exposure of a sample for a few seconds in the dark, and repeated application of the voltage, the j and I_{EL} values build up to the same maximum values as in the first run and then repeat the decay kinetics. The current density and the EL intensity also depend on the polarity of the applied voltage, both j and I_{EL} values being greater for the negative polarity of the Al electrode. As the N value increases (for the same polymer film L and the electric field strength U/L), the I_{EL} value initially grows, passes through a maximum at $N = 50$ mass %, and then decreases. The EL luminance can reach up to several tens of cd/m^2, which makes the emission detectable to the naked eye at usual room lighting.

As the U value grows, the j and I_{EL} increase as well, but this variation is nonlinear (Fig. 2). As can be seen from Fig. 2, the character of the dependence of j on U changes at $U/L \sim 3 \times 10^7$ V/m, whereby the slope of the curve decreases. This is accompanied by the appearance of electroluminescence. When the polymer layer thickness L is increased (for the same N and U/L), I_{EL} also grows to reach a maximum at $L = 1$ μm and then decreases (Fig. 3). The data presented in Figs. 2 and 3 characterize the behavior I_{EL} and j as functions of U/L for the ITO–(PEPC + 50 mass % BFI)–Al structure samples. Additional investigations showed that both j and I_{EL} values increase upon changing the electrode material from aluminum to indium (cf. curves *1* and *2* in Fig. 3). As is seen, replacing the aluminum cathode by indium decreases the threshold value of U/L at which the EL effect is observed.

The experimental results presented above can be interpreted within the framework of the following model. The positive (holes) and negative (electrons) charge carriers appear in the polymer film as a result of temperature- and field-induced injection from electrodes and subsequent drift in the applied electric field. The conclusion that the charge carrier injection from the contacts contributes to the j value is confirmed by the fact that the current increases with decreasing L (for $L < 1$ μm) and the j versus U/L curve corresponds to the Richardson–Schottky equation [5]. Since both j and I_{EL} grow with N up to a dye concentration of 50 mass %, which corresponds to an increase in the degree of aggregation of BFI molecules, we may suggest that the drift of holes in the structure studied proceeds basically by the same mechanism as in the polymer film without additives [6], that is, by hopping between the carbazolyl groups of PEPC. The transport of injected electrons, which is absent in undoped PEPC films, becomes possible in the doped material and increases with dopant concentration. Therefore, we may assume that the transport of nonequilibrium electrons proceeds via BFI

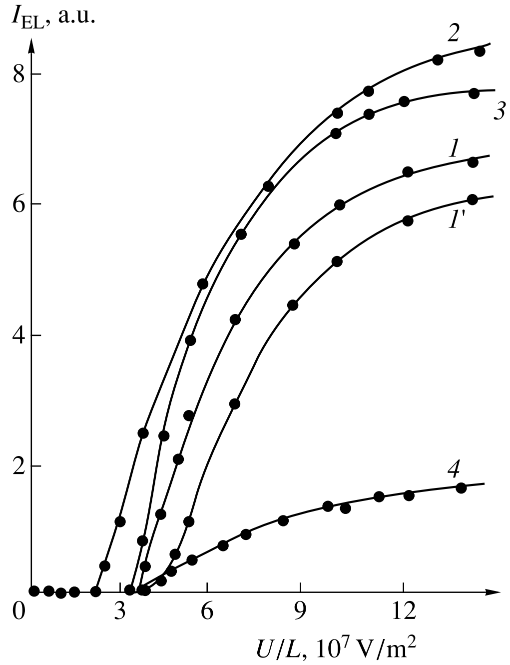

Fig. 3. The plots of I_{EL} versus U/L for an ITO–(PEPC + 50 mass % BFI)–Al structures with various polymer film thicknesses, metal electrode materials, and applied voltage polarities: (*1*) $L = 0.7$ μm, Al($-U$); (*1*') $L = 0.7$ μm, Al($+U$); (*2*) $L = 0.7$ μm, In($-U$); (*3*) $L = 1.0$ μm, Al($-U$); (*4*) $L = 3.1$ μm, Al($-U$).

molecules and is facilitated by a growth in the degree of dye aggregation.

The EL effect in sandwich structures is related to the bulk radiative recombination of charge carriers which takes place in BFI molecules. A decrease in the EL intensity is caused by the fact that PEPC films doped by ionic and intraionic dyes contain traps for nonequilibrium carriers, which are situated near dye ions [7]. Injected holes may fill the traps in the vicinity of dye ions. In such a case, the dye molecule is not involved in the EL effect because the injected electron, being trapped at this molecule, cannot recombine with the trapped hole. In addition, our recent investigations [8, 9] of the photoconductivity and luminescence in PEPC films doped with squarilium dye showed that the traps can also form near electrically charged moieties of the dye molecules. Since BFI molecules (like squaraines) possess a bipolar structure [4], the PEPC films doped with BFI may contain such traps for nonequilibrium carriers near electrically charged moieties of BFI molecules.

REFERENCES

1. P. L. Burn, A. B. Holmes, A. Kraft, *et al.*, Nature **356** (6364), 47 (1992).
2. J. Kalinowski, in *Electrical and Related Properties of Organic Solids*, Ed. by R. W. Munn, A. Miniewicz, and B. Kuchta (Kluwer, Dordrecht, 1997), pp. 167–206.
3. U. Mitschke and P. Bauerle, J. Mater. Chem. **10** (7), 1471 (2000).
4. A. A. Ishchenko, *Structure and Spectral-Luminescent Properties of Polymethine Dyes* (Naukova Dumka, Kiev, 1994).
5. N. A. Davidenko, N. A. Derevyanko, A. A. Ishchenko, *et al.*, Teor. Éksp. Khim. **37** (6), 336 (2001).
6. N. G. Kuvshinskiĭ, N. A. Davidenko, and V. M. Komko, *Physics of Amorphous Molecular Semiconductors* (Lybid', Kiev, 1994).
7. N. Davidenko, A. Ishchenko, N. Derevyanko, *et al.*, Mol. Cryst. Liq. Cryst. **361**, 71 (2001).
8. N. A. Davidenko and A. A. Ishchenko, Fiz. Tverd. Tela (St. Petersburg) **42** (8), 1365 (2000) [Phys. Solid State **42**, 1403 (2000)].
9. Yu. A. Skryshevskiĭ, N. A. Davidenko, A. A. Ishchenko, *et al.*, Opt. Spektrosk. **88** (3), 399 (2000) [Opt. Spectrosc. **88**, 352 (2000)].

Translated by P. Pozdeev

Technical Physics Letters, Vol. 28, No. 6, 2002, pp. 486–488. Translated from Pis'ma v Zhurnal Tekhnicheskoĭ Fiziki, Vol. 28, No. 11, 2002, pp. 91–95.
Original Russian Text Copyright © 2002 by Emel'yanov, Rogacheva.

Recombination-Stimulated Growth of a Dislocation Loop under Conditions of Intense Laser-Induced Electron–Hole Pair Production

V. I. Emel'yanov and A. V. Rogacheva
International Laser Center, Moscow State University, Moscow, Russia
e-mail: emel@em.msk.ru

Received December 19, 2001

Abstract—A mechanism of the recombination-stimulated growth of a coupled interstitial–vacancy disk in a semiconductor featuring intensive generation and localization of electron–hole pairs is proposed. An expression is obtained for the growth rate of the dislocation loop as a function of the laser radiation intensity and the medium temperature. © *2002 MAIK "Nauka/Interperiodica".*

Introduction. The process of laser-induced nucleation of dislocations is usually described in terms of the mechanism of the dislocation formation caused by the shear strain arising as a result of the spatially inhomogeneous laser-induced heating of the crystal [1].

Below we propose a new mechanism explaining the spontaneous growth of a dislocation loop in a semiconductor crystal in the presence of a high concentration of electron–hole pairs generated by laser radiation. The growth of a dislocation loop by this mechanism proceeds due to the energy of recombination of the electron–hole pairs. By analogy with the mechanism of laser-induced point defect production [2–4], the proposed mechanism can be referred to as the radiation-stimulated dislocation loop growth.

Model. Consider a semiconductor in which the laser pumping produces electron–hole pairs and let there appear a seeding defect. The localization and recombination of an electron–hole pair at this defect is accompanied by the liberation of energy spent on creating an interstitial–vacancy pair (recombination-stimulated point defect production) [2–4].

Repeated events of the electron–hole pair localization at the laser generated defects, followed by the pair recombination, energy liberation, and interstitial–vacancy pair formation lead to the appearance of a pair of interstitial and vacancy disks (Fig. 1). Let such a pair form and let us consider the growth of this pair mediated by elementary events whereby an atom passes from the circumference of the vacancy disk v (from the core of subtraction dislocation) to a state i on the circumference of the interstitial disk (in the core of the penetration dislocation) (Fig. 1). Since the initial state v occurs in a contracted region, while the final state i is in an expanded region (Fig. 1), the energy of this atom in the latter state is higher than in the former state (Fig. 2). Owing to recombination of the localized electron–hole pair, the atom performing the $v \longrightarrow i$ transition surmounts the barrier $E_v - E_{\text{exc}}$ (solid arrow in Fig. 2),where E_v is the initial activation energy of the $v \longrightarrow i$ transition and E_{exc} is the energy liberated as a result of recombination (recombination-stimulated transition $v \longrightarrow i$). Since the concentration of localized electron–hole pairs in the vicinity of state i is significantly lower than that in the vicinity of state v (see below), we can neglect the contribution due to the recombination-stimulated transition $i \longrightarrow v$ and assume that an atom performing the reverse transition $i \longrightarrow v$ surmounts the barrier E_i (dashed arrow in Fig. 2). Below we will assume that $E_v > E_i$, but $E_v - E_{\text{exc}} < E_i$.

Since the region of the crystal in the vicinity of state i (on the circumference of the interstitial disk) is

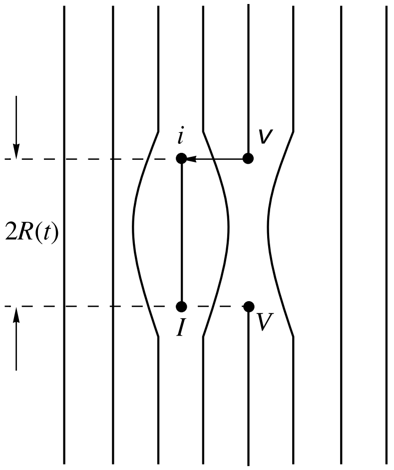

Fig. 1. Schematic diagram illustrating the formation of coupled interstitial (I) and vacancy (V) disks. Arrows indicate the transitions of an atom from crystal state v to defect state i, for which the loop radius increases by one lattice period a.

1063-7850/02/2806-0486$22.00 © 2002 MAIK "Nauka/Interperiodica"

expanded [5], the band gap width ($\Gamma \longrightarrow x$ transition) in this region is greater, while the optical absorption coefficient is smaller than the corresponding values in the defect-free crystal [5]. At the same time, the region of the crystal in the vicinity of state v (on the circumference of the vacancy disk) is contracted [5]. Therefore, the bandgap width in this region is smaller while the optical absorption coefficient is greater than the values in the defect-free crystal. Thus, the rate of free carrier production as a result of the laser-induced interband transitions is greater in the vicinity of state v than in the vicinity of state i. As a result, the rate of localization of the electron–hole pairs and, hence, the concentration of these pairs are also greater in the vicinity of state v. For this reason, and because $E_v - E_{\text{exc}} < E_i$, the rate of $v \longrightarrow i$ transitions exceeds the rate of reverse ($i \longrightarrow v$) transitions. This leads to an increase in the coupled interstitial-vacancy dislocation disks during the laser pulse action (Fig. 2).

Mechanism. We assume that transitions $v \longleftrightarrow i$ proceed only from the circumference of radius R, where $R = R(t)$ is the radius of interstitial–vacancy disks V and I (Fig. 1). Let n_v and n_i denote the number of atoms on the circumferences V and I, respectively. Under the condition $\exp(E_{\text{exc}}/k_BT) \gg 1$, the kinetic equation for n_v is as follows:

$$\frac{\partial n_v}{\partial t} = -\gamma_v n_v + \gamma_i n_i, \quad \gamma_v = \gamma_{v0}\frac{n_s}{n},$$
$$\gamma_{v0} = \frac{1}{\tau}\exp\left(-\frac{E_v - E_{\text{exc}}}{k_BT}\right), \tag{1}$$

$$\gamma_i = \frac{1}{\tau}\exp\left(-\frac{E_i}{k_BT}\right). \tag{2}$$

Here, τ^{-1} is the transition rate constant, n is the number density of atoms in the crystal, n_s is the concentration of localized electron–hole pairs in the same crystal,

$$n_s = BI_L, \tag{3}$$

B is a coefficient characterizing the efficiency of production and localization of the electron–hole pairs, and I_L is the laser radiation intensity. In writing relation (3), it is assumed that localization of the electron–hole pair proceeds within period of time much shorter than the laser pulse duration: $\tau_{loc} \ll \tau_p$ (for details, see [6]).

Taking into account relation (3), we can estimate the average time of the transition $v \longrightarrow i$ after which the loop radius increases by one lattice period a:

$$\gamma_v^{-1} = \gamma_{v0}^{-1}\frac{I_0}{I_L}, \quad I_0 = n/B. \tag{4}$$

Assuming, in accordance with the above model considerations, that $\gamma_i \ll \gamma_v$ and using formulas (4), we obtain an expression for the growth rate of a dislocation loop during irradiation as a function of the laser radiation intensity and the temperature:

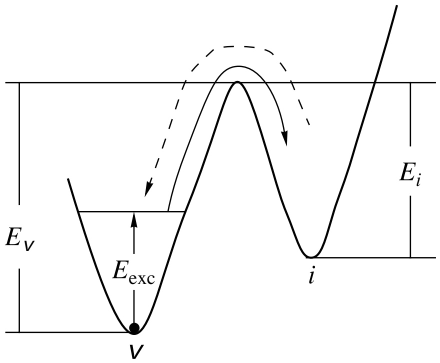

Fig. 2. An energy diagram illustrating the atomic transitions between crystal (v) and defect (i) states.

$$\frac{dR}{dt} = v_g = \gamma_v a = \frac{aI_L}{\tau I_0}\exp\left(-\frac{E_v - E_{\text{exp}}}{k_BT}\right). \tag{5}$$

Here, $T = T_0 + \Delta T$, where T_0 is the initial temperature and ΔT is the temperature increase due to the laser heating. For a sufficiently small intensity of pumping ($\Delta T \ll T_0$), the rate v_g linearly increases with the laser radiation intensity I_L and exhibits an activation dependence on the initial temperature T_0. When the pumping intensity is sufficiently large ($\Delta T \geq T_0$), the dislocation loop growth rate $v_g = v_g(I_L)$ becomes, according to (5), a strongly nonlinear function of the laser intensity. For $I_L/I_0 = n_s/n \sim 10^{-2}$, $a = 3 \times 10^{-10}$ m, $\tau^{-1} = 10^{13}$ s^{-1}, $E_v - E_{\text{exc}} \sim 1.6 \times 10^{-19}$ J, and $T \sim 1500$ K, we obtain an estimate of $v_g \sim 1.3 \times 10^{-2}$ m/s.

After termination of the laser pulse ($I_L = 0$, $n_s = 0$), the localized electron excitations in the vicinity of state v are absent ($E_{\text{exc}} = 0$) and the rate of the $i \longrightarrow v$ transition (dashed arrow in Fig. 2) becomes greater than that of the reverse transition $v \longrightarrow i$ (because $E_i < E_v$). As a result, the dislocation loop radius after termination of the laser pulse starts decreasing (annihilation of the interstitial dislocation disk). Using formula (2), we conclude that the dislocation loop radius decreases at a rate of $v_r = (a/\tau)\exp(-E_i/k_BT)$.

Conclusion. Previously [7], we developed a model of a slow temperature switching wave (with a velocity on the order of 10^{-2} m/s) propagating in a solid with nonequilibrium (laser-induced) defects. This model was used [8] for the interpretation of a slow ($\sim 10^{-2}$ m/s) propagation of the permittivity pulse in a medium excited by pulsed laser radiation. The nonequilibrium defects in [8] were assumed to be the laser-induced dislocation loops, the formation of which was not considered. The above consideration provides for a possible mechanism of the laser-induced generation and annihilation of such loops.

Acknowledgments. This study was supported by the Russian Foundation for Basic Research, project no. 00-02-17249(A).

REFERENCES

1. H. G. van Bueren, *Imperfections in Crystals* (North-Holland, Amsterdam, 1961; Inostrannaya Literatura, Moscow, 1962).
2. H. Sumi, Phys. Rev. B **29**, 4616 (1984).
3. L. C. Kimerling, Solid State Electron. **21**, 1391 (1978).
4. V. I. Emel'yanov and P. K. Kashkarov, Appl. Phys. A **55**, 161 (1992).
5. H. F. Matare, *Defect Electronics in Semiconductors* (Wiley, New York, 1971; Mir, Moscow, 1974).
6. V. I. Emel'yanov and A. V. Rogacheva, Kvantovaya Élektron. (Moscow) **25** (11), 1017 (1998).
7. V. I. Emel'yanov and A. V. Rogacheva, Phys. Lett. A **264**, 478 (2000).
8. E. M. Kudriavtsev, V. I. Emel'yanov, A. V. Rogacheva, *et al.*, Laser Phys. **10** (3), 1 (2000).

Translated by P. Pozdeev

Technical Physics Letters, Vol. 28, No. 6, 2002, pp. 489–490. Translated from Pis'ma v Zhurnal Tekhnicheskoĭ Fiziki, Vol. 28, No. 12, 2002, pp. 1–4.

Straining of a Bi-2223/Ag Ribbon Studied by the Method of Acoustic Emission

E. Dul'kin[a], **V. Beilin**[a], **E. Yashchin**[a], **M. Roth**[a], **and L. V. Grebenkina**[b]
[a] *Graduate School of Applied Science, The Hebrew University of Jerusalem, Jerusalem, 91904 Israel*
[b] *Institute of Mechanics and Applied Mathematics, Rostov State University, Rostov-on-Don, 344104 Russia*
Received December 27, 2001

Abstract—The process of cooling of a Bi-2223/Ag ribbon after secondary sintering at 1000 K is studied by the method of acoustic emission (AE). The acoustic response is observed below 500 K and increases in intensity with decreasing temperature. It is established that the AE signal variation reflects the plastic flow in the silver coating caused by a difference between the thermal expansion coefficients of silver and the ceramic core of the Bi-2223/Ag ribbon. *© 2002 MAIK "Nauka/Interperiodica".*

Previously [1], we reported on the process of secondary sintering of a Bi-2223/Ag ribbon studied by the method of acoustic emission (AE). During the thermal treatment, an AE signal from heated ribbons was detected in the temperature range from 840 to 930 K, which reflected the process of liquid-phase healing of the cracks appearing in the ribbon material in the course of rolling. The process of subsequent cooling remained unstudied. However, the final mechanical properties of commercial ribbons significantly depend on the post-sintering cooling conditions. In view of the successful use of the AE method in [1], we have applied the same technique to investigation of the process of cooling of Bi-2223/Ag ribbons after the secondary sintering stage.

The experiments were performed on 10-mm-long, 3-mm-wide, 0.250-mm-thick samples of a Bi-2223/Ag ribbon fabricated using the standard powder-in-tube (PIT) technology [2]. The AE measurements were performed as described elsewhere [3]. The samples were fixed with a high-temperature glue composition on the edge of a cylindrical acoustic waveguide and introduced into a furnace. A piezoelectric sensor made of a TsTS-19 ceramics was glued to the opposite edge of the waveguide occurring outside the furnace. The samples were heated at a rate of 5 K/min up to 1000 K, kept at this temperature for 20 h, and cooled at the same rate.

In the heating mode, the AE signals from ribbon samples were observed in the temperature range from 840 to 930 K as reported in [1]. On cooling, the acoustic response appears below 500 K (see figure); the AE signal intensity $\dot{N}$ increases with decreasing temperature. The growth of $\dot{N}$ obeys the exponential law and continues until complete cooling down to room temperature. Quantitative analysis of the experimental data leads to the following expression describing the temperature variation of the AE signal intensity:

$$\dot{N}(T) = 2\times10^{5}\exp(-0.02T), \qquad (1)$$

where T is the current temperature.

In order to explain the appearance of the AE signal, let us estimate the relative deformation of the silver coating and the ceramic core of the Bi-2223/Ag composite ribbon. The thermal expansion coefficients of silver and Bi-2223 ceramics along the *a* axis are $\alpha_s = 20.5\times10^{-6}\ \mathrm{K}^{-1}$ and $\alpha_c = 13.6\times10^{-6}\ \mathrm{K}^{-1}$, respectively [4]. In view of the high plasticity of silver (yield stress, 65 MPa) and sufficiently large strength of the sintered ceramics (ultimate strength, 150 MPa) [5], it is the silver component that experiences expansion relative to

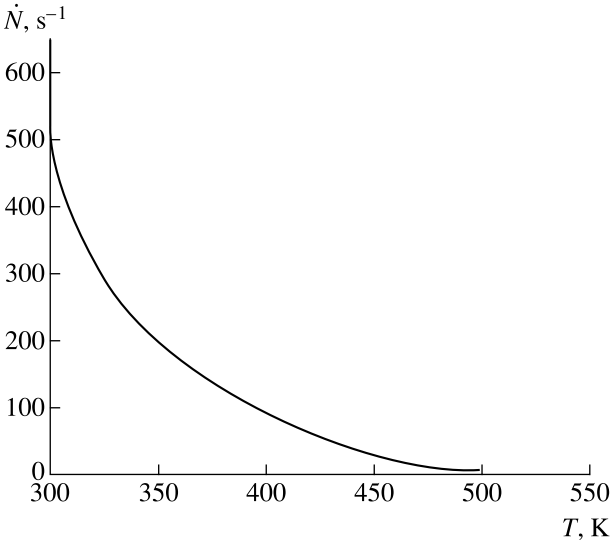

Temperature variation of the AE signal intensity $\dot{N}$ in the course of cooling of a Bi-2223/Ag ribbon after annealing for 20 h at 1000 K.

the ceramic core in the course of cooling. Therefore, we can estimate the relative deformation of silver at 0.35% for the ribbon samples cooled from 1000 to 500 K. This tensile strain exceeds the apparent elastic limit (0.2%) for metals. As is known, the transition from elastic expansion to plastic flow in metals is usually accompanied by the acoustic emission [6–8].

Based on the data obtained, we can explain the observed AE emission as follows. In the course of prolonged high-temperature annealing, the ribbon comprising a silver coating on a ceramic core features thermal diffusion of the components and converts into a metal–ceramic composite. In the course of cooling, the difference in the coefficients of thermal expansion results in the development of mechanical stresses in the ribbon. These stresses are manifested by significant straining of a more plastic silver coating. When the strain exceeds a critical level, silver features a transition from elastic expansion to plastic flow. This is accompanied by the formation of misfit dislocations which serve as a source of the acoustic emission. As the ribbon is cooled, the strain grows and the number of dislocations increases, which is manifested by the increase in the AE intensity $\dot{N}$. Note a significant difference in the behavior of the AE intensity $\dot{N}$ during the production and multiplication of dislocations in this study and in the course of crack healing observed in [1]. A comparison of these data suggests that the dislocation multiplication energy is higher by at least one order of magnitude than the crack healing energy.

REFERENCES

1. E. Dul’kin, V. Beilin, E. Yashchin, *et al.*, Pis’ma Zh. Tekh. Fiz. **27** (9), 79 (2001) [Tech. Phys. Lett. **27**, 387 (2001)].
2. V. Beilin, A. Goldgirsh, E. Yashchin, *et al.*, Physica C (Amsterdam) **309**, 56 (1998).
3. E. A. Dul’kin, Sverkhprovodimost: Fiz., Khim., Tekh. **5**, 102 (1992).
4. A. A. Kiselev, *High-Temperature Superconductivity* (Mashinostroenie, Leningrad, 1990), Vol. 1.
5. Z. Hun, P. Skov-Hansen, and T. Freltoft, Supercond. Sci. Technol. **10**, 371 (1997).
6. S. S.-Y. Hsu and K. Ono, J. Acoust. Soc. Am. **74**, 1304 (1983).
7. O. A. Bartenev and V. A. Khamitov, Zavod. Lab. **53**, 37 (1987).
8. V. V. Polyakov, A. V. Egorov, and I. N. Svistun, Pis’ma Zh. Tekh. Fiz. **27** (22), 14 (2001) [Tech. Phys. Lett. **27**, 937 (2001)].

Translated by P. Pozdeev

Technical Physics Letters, Vol. 28, No. 6, 2002, pp. 491–493. Translated from Pis'ma v Zhurnal Tekhnicheskoĭ Fiziki, Vol. 28, No. 12, 2002, pp. 5–12.
Original Russian Text Copyright © 2002 by Omel'chenko, Uskov.

Interference of Nonstationary Oblique Shock Waves

A. V. Omel'chenko and V. N. Uskov
St. Petersburg State University, St. Petersburg, Russia
e-mail: vmu@peterlink.ru

Received December 18, 2001

Abstract—Special features of calculation of the flow parameters behind a nonstationary oblique shock wave moving in a stream of absolutely nonviscous gas are considered. The wave intensity at which the stream behind the shock wave may exhibit singularities is determined. The problem of calculating a nonstationary shock wave configuration formed during the interaction of a supersonic jet with an obstacle is solved. *© 2002 MAIK "Nauka/Interperiodica".*

Many gasdynamic problems [1–3] encounter the task of determining the parameters of flow f_2 behind a shock wave propagating in a gas stream, given the parameters of flow f_1 (velocity u_1, static pressure p_1, density ρ_1, temperature T_1, etc.) in front of the wave, the velocity w of the shock wave along a straight trajectory making an angle α with the gas stream direction, and the angle σ of the wave slope relative to the trajectory (Fig. 1a).

The main parameter of the problem is the shock wave intensity

$$J = \frac{p_2}{p_1} = (1+\varepsilon)\left(\frac{u_{1n}-D}{a_1}\right)^2 - \varepsilon, \quad \varepsilon = \frac{\gamma-1}{\gamma+1}, \qquad (1)$$

which depends on the components of velocities $u_{1n} = u\sin(\sigma-\alpha)$ and $D = w\sin\sigma$ normal to the wave front and on the thermodynamic variables of the initial stream (sound velocity a_1 and adiabatic index γ). A physically justified condition $J \geq 1$ poses restrictions on the determining parameters, which will be considered below.

Using the conditions for dynamic consistency on the shock wave front [1–3], we can readily determine the Rankine–Hugoniot adiabate of the shock wave; establish relationships between specific enthalpies, temperatures, sound velocities, and the shock wave intensity,

$$E = \frac{\rho_2}{\rho_1} = \frac{J+\varepsilon}{1+\varepsilon J}, \quad \frac{h_2}{h_1} = \frac{T_2}{T_1} = \frac{a_2^2}{a_1^2} = \frac{J}{E} = \frac{J(1+\varepsilon J)}{J+\varepsilon}; \qquad (2)$$

and derive expressions for the normal velocity components

$$D = u_{1n} + \chi I a_1, \quad u_{2n} = u_{1n} + \chi(1-\varepsilon)a_1\left(I - \frac{1}{I}\right),$$
$$I = \sqrt{\frac{J+\varepsilon}{1+\varepsilon}}, \qquad (3)$$

where $\chi = \pm 1$ is the index of wave propagation direction.

Expressing the velocity components through the angles $\sigma_e = \sigma - \alpha$ and β and using the condition $u_{1\tau} = u_{2\tau}$, we determine the stream velocity u_2 behind the shock wave:

$$u_2 = u_1 \frac{\cos\sigma_e}{\cos(\sigma_e - \beta)}. \qquad (4)$$

Formulas (3) and (4) yield a relationship between the angles β and σ_e for the oblique shock wave:

$$\tan(\sigma_e - \beta) = \tan\sigma_e + \chi\frac{(1-\varepsilon)(I - 1/I)}{M_1\cos\sigma_e}. \qquad (5)$$

Combining formulas (4) and (2), we obtain a relati-

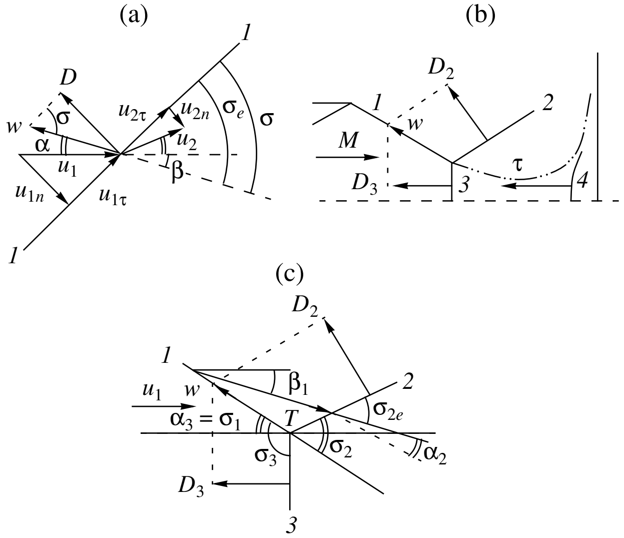

Fig. 1. The flow geometry for (a) an oblique shock wave moving downstream at a velocity *w* in a stream of velocity *u*, (b) overexpanded supersonic stream incident onto an infinite flat obstacle, and (c) triple shock wave configuration moving down a supersonic stream.

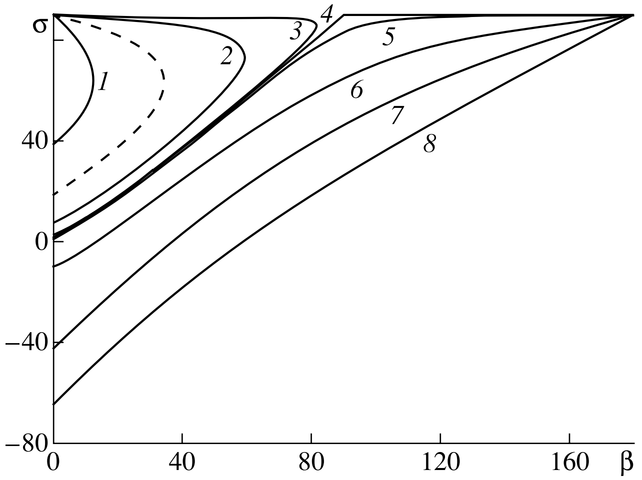

Fig. 2. Plots of the angle β of the stream rotation behind the shock wave versus the sloping angle σ of the wave.

onship

$$M_2 = M_1 \frac{\cos\sigma_e}{\cos(\sigma_e - \beta)} \sqrt{\frac{J + \varepsilon}{J(1 + \varepsilon J)}} \qquad (6)$$

between the Mach number $M_2 = u_2/a_2$ behind the shock wave and that ($M_1 = u_1/a_1$) in the initial stream.

Setting $J = 1$ in Eq. (1), we obtain a formula

$$\sigma_s = \arcsin\frac{M_D - \chi}{M_1}, \qquad (7)$$

which relates the Mach numbers $M_D = D/a_1$ and $M_1 > 0$ to the angle $\sigma_e = \sigma_s$ between the direction of the oncoming stream and the weak discontinuity front. Note that, in contrast to the case of a weak stationary shock wave ($M_D = 0$) for which $\sigma_s = \arcsin(1/M_1)$ is fixed, the σ_s value in the nonstationary case may vary within the interval $[-\pi/2, \pi/2]$. In the nonstationary case, the interval $\sigma_s \in (0, \pi/2]$ corresponds to a weak opposite shock wave, while the interval $\sigma_s \in [-\pi/2, 0)$ corresponds to a weak cocurrent shock wave. The special value $\sigma_s = 0$ refers to the case of a weak shock wave propagating perpendicularly to the oncoming stream, whereby the stream does not influence the shock wave (which propagates as if the stream were absent).

The value of $J = 1$ corresponds to the minimum possible intensity of the shock wave. A maximum intensity is attained for the J values corresponding to a forward shock wave ($\sigma = \pi/2$). Let us fix the Mach number $M_1 > 0$ and analyze the behavior of the main gasdynamic parameters for various M_D and $J \geq 1$, restricting the consideration to $\chi = -1$.

As can be seen from formula (7), the range of M_D ($\chi = -1$) is limited from above by $M_D = M_1 - 1$. For this M_D value, the stream can feature only a weak discontinuity with $J = 1$ and $\sigma = \pi/2$, which either propagates upstream (for $M < 1$) or is carried downstream (for $M > 1$). As the M_D value decreases, the lower boundary σ_s given by formula (7) goes down to reach zero for $M_D = -1$ and the value $\sigma_s = -\pi/2$ for $M_D = -M_1 - 1$. For $M_D < -M_1 - 1$, an oblique shock wave with an intensity $J > 1$ exists for any $\sigma \in [-\pi/2, \pi/2]$.

Figure 2 shows the $\sigma(\beta)$ curves constructed for various $M_D < M_1 - 1$, where $M_1 = 3$. As can be seen, the character of these curves significantly depends on the M_D value. For $M_D \in (M_*, M_1 - 1)$, the shape of $\sigma(\beta)$ (curves *1*–*3*) is qualitatively the same as in the case of a stationary shock wave ($M_D = 0$, dashed curve). For $M_D < M_*$, there always exists a shock wave which causes the stream to deviate by any preset angle $\beta \in [0°, 180°]$ (curves *5*–*8*).

The special Mach number M_* corresponds to the case whereby the M_2 value becomes zero behind the forward shock wave (curve *4*). Using formulas (1) and (3), we can readily obtain a relationship between M_* and the Mach number M_1 of the oncoming stream:

$$M_* = \frac{(1 - 2\varepsilon)M_1 - \sqrt{M_1^2 + 4(1 - \varepsilon)^2}}{2(1 - \varepsilon)}. \qquad (8)$$

For $M_D < M_*$, the stream behind the forward shock wave is rotated by 180°; for $\sigma < \pi/2$, the angle of rotation varies within the interval $\beta \in [0°, 180°]$. For $M_D < -M_1 - 1$, all the $\sigma(\beta)$ curves originate from the point (0°, –90°) and come to the point (180°, 90°).

In practical problems involving nonstationary shock waves, the analysis is usually performed using reversal of the wave motion [3]. The passage from a laboratory coordinate system to that related to the moving shock wave simplifies the problem by reducing the analysis to a simpler case of the jump in compression [2]. However, this transformation is not always possible in complicated cases involving the interference of oblique shock waves. For example, consider a shock wave configuration encountered in the study of nonstationary processes in jet streams [4]. When a homogeneous flat stream is outgoing from a profiled overexpanding nozzle ($n_a = p_n/p_a < 1$), there appears a straight oblique compression jump *1* (Fig. 1b) at the nozzle edge. In the case of an efficiently small n_a value, this shock wave exhibits irregular reflection from the stream axis. As a result of this reflection, there appear the Mach jump *3*, the reflected oblique jump *2*, and the tangential discontinuity τ separating the stream behind jumps *2* and *3*. For the sake of simplicity, let us assume that reflection of the oblique jump gives rise to a stationary Mach configuration of the shock waves in which the branching jump *3* is orthogonal to the current lines of the oncoming stream.

Let such a stream come onto an infinite flat obstacle (Fig. 1b). As was demonstrated previously (see, e.g., [5]), the dynamic and total pressures in the supersonic stream past the jumps *1* and *2* may significantly exceed the corresponding values behind the straight jump *3* in a subsonic flow. A large difference between these value may result in that the tangential discontinuity τ would instantaneously “stick” to the obstacle surface and block the subsonic flow. As a result, the “sticking” point will give rise to a curvilinear shock wave *4* interacting with the Mach jump *3* and propagating upstream. This will lead to a shift of the shock wave *2* containing the special point T with the branching jump *3* (Fig. 1c). Thus, we arrive at the problem of describing the stream behind the shock wave *2*.

In order to solve this problem, note that the shock wave *2* propagates along a trajectory coinciding with the line of jump *1* at a velocity of $w = D_2/\sin\sigma_2 = D_3/\sin\sigma_3$, where D_2 and D_3 are the velocities of shock waves *2* and *3*, respectively; σ_2 and $\sigma_3 = \pi/2 + \sigma_1$ are the angles between vector w and the surfaces of discontinuities *2* and *3*, respectively; and σ_1 is the sloping angle of jump *1* (Fig. 1c). The shock wave *3* moving upstream at a relative velocity of $M_{D3} < 0$ leads to an increase in the wave intensity,

$$J_3 = (1+\varepsilon)\left[\frac{u}{a}\sin(\sigma_3 - \alpha_3) - \frac{w}{a}\sin\sigma_3\right]^2 - \varepsilon$$

$$= (1+\varepsilon)(M - M_{D3})^2 - \varepsilon,$$

where $\alpha_3 = \sigma_1$ is the angle between vector w and the oncoming stream velocity u. As a result, the intensity $J_2 = J_3/J_1$ of the shock wave *2* increases as well, this leading to a change in the angle σ_2 related to J_2 by the formula (1)

$$J_2 = (1+\varepsilon)(M_1\sin\sigma_{2e} - M_{D2})^2 - \varepsilon,$$
$$\sigma_{2e} = \sigma_2 - \alpha_2. \qquad (9)$$

Here, M_1 is the Mach number behind jump *1* and $\alpha_2 = \sigma_1 - \beta_1$ is the angle between vector w and the stream velocity u_1 behind jump *1*. Upon numerically solving Eq. (9), we can calculate σ_2 and, hence, determine β_2, the angle of stream rotation (5) by shock wave *2*.

In the general case, the angle β_2 differs from β_{20}, the angle of stream rotation behind the immobile jump *2* in the stationary Mach configuration. As a result, the conditions of dynamic consistency at the tangential discontinuity τ separating the streams are broken. To restore these conditions, we have to admit that the initial straight jump *3* acquires curvature in the vicinity of the triple point T in the course of the shock wave motion. The curvature must provide both for the condition of equal pressures and for the collinearity of current lines above and below the tangential discontinuity τ (Fig. 1c). Assuming that the velocity w at which the shock wave *3* moves along jump *1* is still related to the velocity D_3 of the shock wave in the vicinity of the symmetry axis as $D_3 = w\cos\sigma_1$, we arrive at a system of equations for determining the gasdynamic parameters of flow at the branching point T (Fig. 1c):

$$J_3 = J_1 J_2, \quad \beta_3 = \beta_2 - \beta_1. \qquad (10)$$

Here, the intensities J_2 and J_3 are calculated by formulas (9), while J_3 is determined as

$$J_3 = (1+\varepsilon)(M\sin\sigma_{3e} - M_w\sin\sigma_3)^2 - \varepsilon,$$
$$\sigma_{3e} = \sigma_3 - \alpha_3, \quad M_w = w/a,$$

and the angles β_2 and β_3 are determined using formula (5). The results of calculations showed that, as the velocity D_3 of the Mach jump *3* grows, the intensities J_2, J_3 and the angles β_2, β_3 monotonically increase. A more complicated behavior is observed for the angle σ_3 describing the slope of jump *3* at the point T: the function $\sigma_3(M_{D3})$ initially (at small $|M_{D3}|$) decreases from $\sigma_{30} = 90° + \sigma_1$, then exhibits a minimum, and eventually increases again tending to σ_{30} as $M_{D3} \longrightarrow M_*$, where M_* is given by formula (8). At the point $M_{D3} = M_*$, the derivative of the function $\sigma_3(M_{D3})$ exhibits discontinuity; for $M_{D3} < M_*$, the σ_3 value monotonically decreases with increasing $|M_{D3}|$. It should be noted that, for $|M_{D3}| > |M_*|$, the stream behind jump *3* changes direction to the opposite and the gasdynamic parameters in the vicinity of point T have to be calculated using, instead of Eqs. (10), the system of equations

$$J_3 = J_1 J_2, \quad \pi - \beta_3 = \beta_2 - \beta_1.$$

Acknowledgments. This study was supported by the Russian Foundation for Basic Research (project no. 00-15-96106) and by the INTAS Foundation (grant no. 99-785).

REFERENCES

1. V. N. Uskov, *Traveling One-Dimensional Waves* (Balt. Gos. Tekh. Univ., St. Petersburg, 2000).
2. K. P. Stanyukovich, *Nonstationary Motions of Continuous Medium* (Gostekhizdat, Moscow, 1955).
3. G. Emanuel and T. H. Yi, Shock Waves, No. 10, 113 (2000).
4. B. G. Semiletenko, B. N. Sobkolov, and V. N. Uskov, Izv. Sib. Otd. Akad. Nauk SSSR, Tekh. Ser., No. 13 (1975).
5. A. V. Omel’chenko and V. N. Uskov, Izv. Akad. Nauk, Mekh. Zhidk. Gaza, No. 6, 118 (1995).

Translated by P. Pozdeev

Technical Physics Letters, Vol. 28, No. 6, 2002, pp. 494–496. Translated from Pis'ma v Zhurnal Tekhnicheskoĭ Fiziki, Vol. 28, No. 12, 2002, pp. 13–18.
Original Russian Text Copyright © 2002 by Khodenkov.

Orientation Transitions in the Domain Wall Structure of Orthoferrites

G. E. Khodenkov
Institute of Electronic Control Computers, Moscow, Russia
e-mail: angeline@mtu-net.ru

Received January 11, 2002

Abstract—The effect of higher anisotropy constants on the orientational phase transitions in the domain walls (DWs) in orthoferrites of the G_xF_z type is studied. Equations of the reduced description of the DW structure in the vicinity of the transition point (determined by the equality of two independent second-order crystallographic anisotropy constants) are constructed, which are analogous to the Slonczewski equations for uniaxial ferromagnets. It is established that, in addition to DWs of the known (*ab* and *ac*) types, stable DWs with different spin rotation planes may exist depending on the relationships between fourth-order anisotropy constants. In some cases, the DW spectra may contain an antisymmetric local level in addition to the DW translational mode. *© 2002 MAIK "Nauka/Interperiodica".*

Weak ferromagnets, including rare earth orthoferrites, are highly promising media for information technologies. In this context, it is of interest to study the special orientational phase transitions in the internal structure of domain walls (DWs) accompanying changes (induced by temperature of some other factor) in constants of the crystallographic magnetic anisotropy. A transition of this type was probably observed by Zalesskiĭ *et al.* [1].

The theory of such transitions was developed mostly by Farztdinov *et al.* [2, 3]. However, the transition point in this theory was determined using the condition of equality of the energies of various domain structures. In terms of Hubert and Schaefer [4], this corresponds to the equilibrium thermodynamic approach. Below we develop a simple theory valid in the vicinity of the transition point. Using this theory, analogous to the Slonczewski equations for uniaxial ferromagnets [5], one can readily determine the intermediate DW structures and evaluate their local stability.

Let us restrict the consideration to an orthoferrite in the G_xF_z state (with the antiferromagnetic vector $\mathbf{l}$ in the domains being collinear to the *x* axis; the coordinate axes *x*, *y*, and *z* coincide with the crystallographic axes *a*, *b*, and *c*, respectively). We use an approximate theory with the unit vector $\mathbf{l}$ (magnetization vector excluded) and the effective Lagrangian in the form (for details see, e.g., [6]):

$$\mathscr{L} = \frac{M_0}{2\gamma\omega_E}\dot{\mathbf{l}}^2 - \tilde{\Phi},$$

$$\tilde{\Phi} = \frac{1}{2}A(\nabla\mathbf{l})^2 + \frac{1}{2}(K_b^{(2)}l_y^2 + K_c^{(2)}l_z^2) \qquad (1)$$

$$+ \frac{1}{4}(K_{bb}^{(4)}l_y^4 + 2K_{bc}^{(4)}l_y^2l_z^2 + K_{cc}^{(4)}l_z^4).$$

Here, M_0 is the magnetization of sublattices in the orthoferrite; γ is the magnetomechanical (gyromagnetic) ratio; $\omega_E = \gamma a/M_0$, $a \sim 10^9$ erg/cm^3 and $A \sim 10^7$ erg/cm being the homogeneous and inhomogeneous exchange constants, respectively; $K_{**}^{(j)}$ are the renormalized anisotropy constants of the second ($j = 2$, $K_{**}^{(2)} \sim 10^6$ erg/cm^3, positive) and fourth ($j = 4$, $K_{**}^{(4)} \sim 0.1|K_{**}^{(2)}|$) orders (the Dzyaloshinsky constant renormalizes $K_b^{(2)}$ and does not enter (1) explicitly). Analogous representations, developed for magnets of other types, are widely used in the theory of DW spectra [7, 8].

For definiteness, let the DW plane be perpendicular to the *y* axis. Then, according to Eq. (1), there exist one-dimensional DWs with a single angular degree of freedom $\varphi(y)$ of two simple types, *ab* and *ac*, characterized by the 180° rotation of $\mathbf{l}(y)$ in the *ab* (*xOy*) and *ac* (*zOx*) planes, respectively. In particular, for *ab*-DW,

$$\cos\varphi = -\sqrt{1+\kappa_{ab}}\tanh y/\sqrt{1+\kappa_{ab}\tanh^2 y},$$
$$\varphi'(y) = \sin\varphi\sqrt{1+\kappa_{ab}\sin^2\varphi}, \qquad (2)$$

where the angle $\varphi(y)$ is counted from the *x* axis; the lengths are measured in the units of $\Delta_{ab} = \sqrt{A/K_b^{(2)}}$ (the effective width of *ab*-DW); and $\kappa_{ab} = K_{bc}^{(4)}/2K_b^{(2)}$. Equation (1) yields two separate equations for the amplitudes of small oscillations δl:

$$\Omega^2\delta l_{\parallel,\perp} = \hat{L}_{\parallel,\perp}\delta l_{\parallel,\perp} \equiv \left(-\frac{d^2}{dy^2} + V_{\parallel,\perp}(y)\right)\delta l_{\parallel,\perp};$$

1063-7850/02/2806-0494$22.00 © 2002 MAIK "Nauka/Interperiodica"

$$\begin{aligned} V_{\parallel}(y) &= \varphi'''(y)/\varphi'(y), \\ V_{\perp}(y) &= (-2 + K_{bc}^{(4)}/K_{b}^{(2)})\sin^{2}\varphi \\ &\quad - 3(K_{bc}^{(4)}/2K_{b}^{(2)})\sin^{4}\varphi + K_{c}^{(2)}/K_{b}^{(2)}, \end{aligned} \tag{3}$$

where $\delta l_{\parallel,\perp}(y)$ are small amplitudes in the spin rotation plane xOy and in the perpendicular plane; $\Omega^2 = \omega^2 M_0/\gamma\omega_E K_b^{(2)}$; and ω are the unknown resonance frequencies. The analogous results for *ac*-DWs are presented below in a somewhat different context.

The local stability of *ab*-DWs described by Eqs. (2) is determined by the condition of positiveness of the corresponding operator: $\hat{L}_{\perp} > 0$. With an allowance for the condition $K_{**}^{(2)} > |K_{**}^{(4)}|$, the eigenvalue problem (3) in the zero approximation ($K_{**}^{(4)} = 0$) reduces to a potential of the type $1 - 2/\cosh^2 y$ (well known in the DW theory). For this potential, the lower eigenvalue is zero and the corresponding symmetric eigenfunction is $\delta l_{\perp}^{0}(y) = 1/(\sqrt{2}\cosh y)$. Taking into account the lowest powers in $K_{**}^{(4)}$ in the expansion of $V_{\perp}(y)$, we obtain the following condition of stability in the first-order perturbation theory:

$$K_{c}^{(2)} - K_{b}^{(2)} + 2(K_{bc}^{(4)} - K_{bb}^{(4)})/3 > 0. \tag{4}$$

Now let us determine the discrete levels of the operator $\hat{L}_{\parallel}$. As is evident from the form of $V_{\parallel}(y)$ in Eqs. (3), a lower eigenfunction of $\hat{L}_{\parallel}$ is the symmetric function $\delta l_{\perp}^{0}(y) \sim \varphi'(y)$ corresponding to the eigenvalue $\omega = 0$ (translational level of the spectrum). In order to determine additional levels [9], note that (also due to the form of Eqs. (3)) this operator can be represented as

$$\hat{L}_{\parallel} = \hat{A}^{+}\hat{A} \equiv (d/dy + \varphi''/\varphi')(-d/dy + \varphi''/\varphi'). \tag{5}$$

Introducing the new dependent variable $\hat{A}m_{\parallel}(y)$, we obtain a relationship equivalent to the initial one, but with a different potential:

$$V_{\parallel}^{*}y = 1 + 2\kappa_{ab}/\cosh^{4}y(1 + \kappa_{ab}\tanh^{2}y). \tag{6}$$

Now it is evident that an additional level exists if $\kappa_{ab} < 0$. For $|\kappa_{ab}| < 1$ (as in the case under consideration), the shallow level approximation is valid. In this approximation, the potential (6) can be replaced by the delta function $1 - (8|\kappa_{ab}|/3)\delta(y)$, which yields

$$\Omega^2 = 1 - \frac{16}{9}\kappa_{ab}^{2}, \quad \delta l_{\parallel}^{0}(y) \sim \tanh y \exp\left(-\frac{4}{3}|\kappa_{ab}||y|\right). \tag{7}$$

The DW structure and the corresponding spectrum are presented in the figure (constructed for $\kappa_{ab} = -0.1$), where the calculated eigenvalue differs from that given by (7) only in the third decimal digit and the eigenfunctions fully coincide on the drawing scale employed.

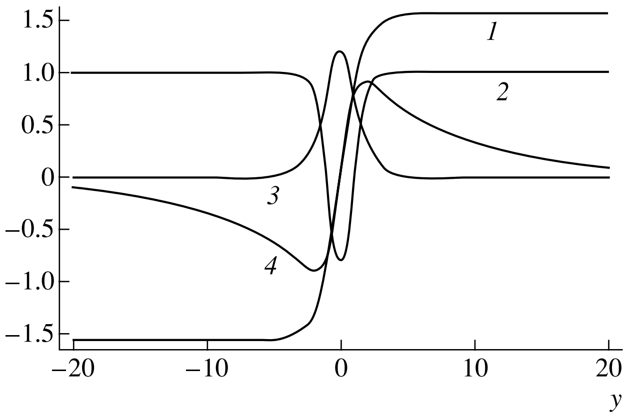

The structure and eigenfunctions of *ab*-DWs (for $\kappa_{ab} = -0.1$): (*1*) angle $\varphi(y)$ calculated by formula (2); (*2*) potential $V_1(y)$ calculated by formula (3); (*3*) non-normalized lower ($\Omega = 0$) eigenfunction $\sim \varphi'(y)$; (*4*) antisymmetric eigenfunction ($\Omega^2 \approx 0.98$, see (6)).

In order to study the transition region, where $K_c^{(2)} \approx K_b^{(2)}$ and the DWs with two angular degrees of freedom may exist, let us represent the anisotropic terms in (1) responsible for the transition as

$$\frac{1}{4}(K_{b}^{(2)} + K_{c}^{(2)})\sin^{2}\vartheta + \frac{1}{4}(K_{b}^{(2)} - K_{c}^{(2)})\sin^{2}\vartheta\cos 2\psi. \tag{8}$$

Here, vector **l** is replaced by the angular variables in a spherical coordinate system with the polar angle ϑ counted from the x axis and the azimuthal angle ψ counted from the y axis (normal to the DW plane). In this representation, the second (difference) term is small ($\sim K_{**}^{(4)}$) and the problem acquires the small parameter $\varepsilon = |K_b^{(2)} - K_c^{(2)}|/(K_b^{(2)} + K_c^{(2)})$. Formulated in this way, the problem formally coincides with the problem of 180° DWs in a strongly anisotropic uniaxial ferromagnet (the parameter ε corresponds to $1/Q$, where $Q \gg 1$ is the so-called quality factor of the uniaxial ferromagnet). As is known, the latter case admits a simple description of a spatial (non-one-dimensional) low-frequency dynamics based on a reduced theory (with excluded coordinate y) employing the Slonczewski equations.

In the vicinity of the transition, we may take $\sin\vartheta = 1/\cosh y/\Lambda$ (where $\Lambda = \sqrt{2A/(K_b^{(2)} + K_c^{(2)})}$). Upon averaging the energy density over y, which is the simplest procedure for passing to the Slonczewski equations, we obtain the surface energy density σ replacing $\tilde{\Phi}$ in Eq. (1):

$$\sigma = \Delta\Big\{A(\nabla_{x,z}\psi)^2 + (K_b^{(2)} + K_c^{(2)})\sin^2\psi + \frac{1}{3}[K_{bb}^{(4)}\cos^4\psi + 2K_{bc}^{(4)}\sin^2\psi\cos^2\psi + K_{cc}^{(4)}\sin^4\psi]\Big\}. \tag{9}$$

Note that, according to Eq. (1), the characteristic Bloch line widths $\Lambda = \sqrt{2A/(K_b^{(2)} - K_c^{(2)})}$ [2] for the DW of orthoferrites significantly exceed the DW width Δ. In this approximation, real DWs with two angular degrees of freedom are replaced by one-angle walls. The small corrections ~ε can be constructed within the framework of the general procedure of deriving the Slonczewski equations [10].

Let us restrict the consideration to homogeneous states of the DWs described by Eq. (9). The *ab*-DW state type corresponds to $\psi = 0, \pi$ and the local stability condition $\partial^2\sigma/\partial\psi^2 > 0$ coincides with inequality (4) following from exact perturbation theory. According to Eq. (9), the *ac*-DW state corresponds to $\psi = \pm\pi/2$ and the local stability condition analogous to (4) is

$$K_b^{(2)} - K_c^{(2)} + 2(K_{bc}^{(4)} - K_{cc}^{(4)})/3 > 0. \tag{10}$$

In addition to the simple DWs of the *ab* and *ac* types, the equation $\partial\sigma/\partial\psi = 0$ admits some other solutions (states) corresponding to

$$\cos 2\psi = 3\frac{K_c^{(2)} - K_b^{(2)} + 1/3(K_{cc}^{(4)} - K_{bb}^{(4)})}{K_{bb}^{(4)} - 2K_{bc}^{(4)} + K_{cc}^{(4)}}, \tag{11}$$

which are stable provided that

$$\left|K_c^{(2)} - K_b^{(2)} - 1/3(K_{cc}^{(4)} - K_{bb}^{(4)})\right| < K_{bb}^{(4)} - 2K_{bc}^{(4)} + K_{cc}^{(4)}. \tag{12}$$

The results of this study indicate that the transitions between *ab* and *ac* DWs in orthoferrites are accompanied by a number of interesting effects. The transitions may appear as “extended” (cf. the local stability conditions (4) and (10)), whereby new states (phases) of DWs (possessing two degrees of freedom and approximately described by Eqs. (11)) can arise inside a region with the dimensions ~max$|K^{(4)}|$. In addition, an antisymmetric high-frequency mode (7) localized at the DW can be excited provided that the fourth-order anisotropy constants obey certain additional conditions.

REFERENCES

1. A. V. Zalesskiĭ, A. M. Savvinov, I. S. Zheludev, and A. N. Ivashchenko, Zh. Éksp. Teor. Fiz. **68** (4), 1449 (1975) [Sov. Phys. JETP **41**, 723 (1975)].
2. M. M. Farztdinov, *Physics of Magnetic Domains in Antiferromagnets and Ferrites* (Nauka, Moscow, 1981).
3. M. M. Farztdinov, *Spin Waves in Ferromagnets and Antiferromagnets with Domain Structure* (Nauka, Moscow, 1988).
4. A. Hubert and R. Schaefer, *Magnetic Domains* (Springer-Verlag, Berlin, 1998), p. 696.
5. A. P. Malozemoff and J. C. Slonczewski, *Magnetic Domain Walls in Bubble Materials* (Academic, New York, 1979; Mir, Moscow, 1982).
6. V. G. Bar’yakhtar, M. V. Chetkin, B. A. Ivanov, and S. N. Gadetskii, *Dynamics of Topological Magnetic Solitons* (Springer-Verlag, Berlin, 1994), p. 179.
7. B. A. Ivanov, A. K. Kolezhuk, and G. M. Wysin, Phys. Rev. Lett. **76** (3), 511 (1996).
8. B. A. Ivanov, V. M. Murav’ev, and D. D. Sheka, Zh. Éksp. Teor. Fiz. **116** (3), 1091 (1999) [JETP **89**, 583 (1999)].
9. G. E. Khodenkov, Fiz. Met. Metalloved. **61** (5), 850 (1986).
10. G. E. Khodenkov, Fiz. Met. Metalloved. **78** (3), 33 (1994).

Translated by P. Pozdeev

Technical Physics Letters, Vol. 28, No. 6, 2002, pp. 497–500. Translated from Pis'ma v Zhurnal Tekhnicheskoĭ Fiziki, Vol. 28, No. 12, 2002, pp. 19–26.
Original Russian Text Copyright © 2002 by Matveev, Gusarevich.

Single and Double Ionization Cross Sections of Atoms Colliding with Relativistic Structural Heavy Ions

V. I. Matveev* and E. S. Gusarevich
Pomorskiĭ State University, Arkhangelsk, Russia
** e-mail: matveev.victor@pomorsu.ru*

Received December 3, 2001

Abstract—The single and double ionization cross sections of hydrogen and helium atoms colliding with relativistic structural heavy ions are calculated within the framework of the eikonal approximation. By structural ions are implied those containing partly occupied electron shells. It is shown that an allowance for the finite size of charged ions leads to significant changes in the ionization cross sections as compared to those determined for the point ions possessing the same charges and energies. © *2002 MAIK “Nauka/Interperiodica”.*

Many experiments on heavy particle accelerators involve partly stripped relativistic ions possessing large charges and high energies (see, e.g., [1–7] and references therein). The usual calculation schemes describe such screened ions as point charges. Theoretical investigations of the excitation or ionization of target atoms under the action of partly stripped ions described as finite-size charged particles with a certain electron structure are rather few. In fact, the projectile incident upon a target should be considered as an extended structural particle with dimensions on the order of the size of electron shells occupied by electrons corresponding to a stationary ion charge, rather than as a point charge.

However, the strong field of a multicharge ion cannot be considered using the perturbation theory (see, e.g., [8]) within the framework of a widely employed method of classical trajectories. Applicability of this method, which is still insufficiently justified proceeding from the first principles [9], is only confirmed by comparison to experiment. A nonperturbative quantum-mechanical analysis of this situation within the framework of a sudden perturbation approach attempted by Yudin [10, 11] allowed the ionization probabilities to be determined within a limited interval of impact parameters, while the total ionization cross sections were determined by recourse to a semiempirical procedure of renormalization in the Born approximation.

In this study, we have developed a nonperturbative method for calculating the ionization and excitation cross sections of target atoms interacting with partly stripped relativistic multicharge ions considered as extended charges using the eikonal approximation and the method of solution matching proposed previously [12–14]. For illustration, we applied the proposed method to calculation of the cross sections for the single ionization of hydrogen and the double ionization of helium atoms. It will be shown that an allowance for the extended ion charge leads to significant changes in the ionization cross sections as compared to those determined in the case of projectiles considered as point charges possessing the same charges and energies. It should be noted that we decline from discussing the processes of excitation and loss of electrons belonging to projectile ions, which are now under extensive experimental and theoretical investigation (see, e.g., [15, 16]).

Consider a nonrelativistic (both before and after collision) N-electron atom resting at the origin of the coordinates. As demonstrated in [12, 13], a cross section for the transition of this atom from state $|0\rangle$ into state $|n\rangle$ upon collision with a relativistic ion moving at a velocity v can be described in the small-angle eikonal approximation as (here and below we use the atomic system of units)

$$\sigma_n = \int d^2b \left| \left\langle n \left| 1 - \exp\left\{ -\frac{i}{v} \int_{-\infty}^{+\infty} U(X, \mathbf{b}; \{\mathbf{r}_a\}) dX \right\} \right| 0 \right\rangle \right|^2. \quad (1)$$

The scattering Coulomb potential $U = U(X, \mathbf{b}; \{\mathbf{r}_a\})$ is considered as a function of both the ion coordinates $\mathbf{R} = (X, \mathbf{b})$, expressed through the impact parameter b, and the set of positions of the atomic electrons $\{\mathbf{r}_a\}$ ($a = 1, \ldots, N$). The Coulomb interaction of the partly screened ion occurring at the point $\mathbf{R}$, with N_i atomic electrons located at the points $\mathbf{r}_a$ on the corresponding shells, is described by the potential [11, 17–19]

$$U(\mathbf{R}; \{\mathbf{r}_a\}) = -\sum_a \left\{ \frac{Z(1-\nu)}{|\mathbf{r}_a - \mathbf{R}|} + \frac{Z\nu}{|\mathbf{r}_a - \mathbf{R}|} \exp\left(-\frac{1}{\lambda} |\mathbf{r}_a - \mathbf{R}| \right) \right\}.$$

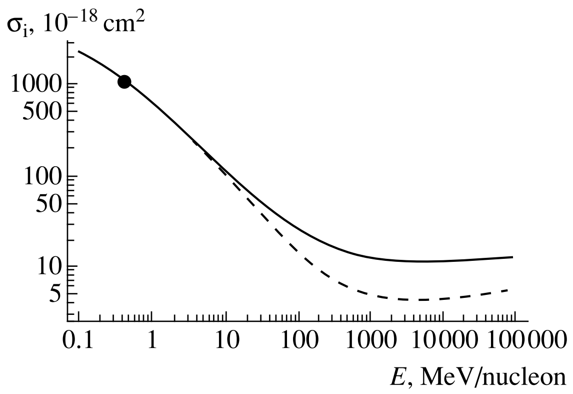

Fig. 1. The ionization cross section for a hydrogen atom colliding with partly stripped uranium ions U^{6+}. Solid and dashed curves refer to extended and point ions with the same charge and energy, respectively; the black circle shows the experimental result for C^{6+} + H collisions [5].

Here, λ is the screening parameter, bearing the physical meaning of an effective ion radius, which is determined by the formula

$$\lambda = g\frac{v^{2/3}}{1 - v/7}\frac{1}{Z^{1/3}};$$
$$g = 0,3(3\pi^2/50)\Gamma(1/3) \approx 0.48, \qquad (2)$$

where $v = N_i/Z$ is the relative number of electrons in the ion.

A special feature of collisions between multicharge ions and atoms is that the inelastic cross sections are usually rather large and significantly exceed the atomic dimensions. Taking this circumstance into consideration, we can assume that $r_a/R \ll 1$ and write the integral in expression (1) as

$$-\frac{i}{v}\int_{-\infty}^{+\infty} U dX = i\mathbf{q}\sum_a \mathbf{r}_a,$$
$$\mathbf{q} = \frac{2Z^*}{vb}\left[1 + \frac{v}{1-v}\frac{b}{\lambda}K_1\left(\frac{b}{\lambda}\right)\right]\frac{\mathbf{b}}{b}, \qquad (3)$$

where vector $\mathbf{q}$ has an evident meaning of the momentum transferred to atomic electrons from a projectile ion with an impact parameter $\mathbf{b}$, $Z^* = Z(1 - \nu)$ is the effective (apparent) ion charge, and $K_1(x)$ is the Macdonald function.

First, let us consider the collision of a relativistic structural multicharge ion with a hydrogen atom. Following [12, 13], the cross sections of inelastic processes can be described using the method of solution matching, which allows the final formulas to be expressed in an analytical form. The whole interval $0 < b < \infty$ of possible values of the impact parameter b can be divided into two regions:

$$\text{(A) } 0 < b < b_0, \quad \text{(B) } b_0 < b < \infty;$$

$$b_0 \sim v\gamma, \quad \gamma = 1/\sqrt{(1-\beta^2}, \quad \beta = v/c, \qquad (4)$$

which correspond to small and large values of the impact parameter (c is the speed of light). In the region of small impact parameters (A), a strong field of the multicharge ion can be described within the framework of the perturbation theory and the cross section can be calculated by formula (1). In the region of large impact parameters (B), the field of the projectile ion can be considered as weak and described as the field of a point charge Z^*, while the cross section can be calculated using perturbation theory. Calculating σ_n in both regions (4) and summing the results, we obtain the total cross section. Note that knowledge of the exact boundary between regions (A) and (B) is insignificant because the dependence of σ_n on b_0 in each of the two regions is logarithmic. This ensures correct matching of the corresponding contributions, so that the particular form of the dependence of σ_n on b_0 is eliminated from the final expression.

The resulting ionization cross section of a hydrogen atom is as follows (cf. [13]):

$$\sigma_i = 8\pi\frac{Z^{*2}}{v^2}\lambda_i\left(\ln\frac{2\alpha_i v^2\gamma}{\eta Z^*\omega_i} - \frac{\beta^2}{2}\right), \qquad (5)$$

where $\eta = \exp B = 1.781$ ($B = 0.5772$ is the Euler constant), $\omega_i = 0.711$ is the so-called "mean" ionization energy [13], $\lambda_i = 0283$, and α_i are coefficients calculated by the formula

$$\alpha_i = \lim_{b_0 \to \infty}\frac{Z^*}{vb_0}$$
$$\times \exp\left\{\frac{1}{\lambda_i}\frac{v^2}{8\pi Z^{*2}}\int_0^{b_0} 2\pi b db \int d^3\mathbf{k}|\langle\mathbf{k}|\exp(i\mathbf{qr})|0\rangle|^2\right\}. \qquad (6)$$

Note that formula (5) coincides in form with the expression obtained [13] for the ionization by collision with a point charge Z^*. However, in the case of the point charge, the coefficients $\alpha_i = 3.264$ are independent of the ion charge and velocity [13]. In contrast, by virtue of the transferred momentum determined by formula (3), the α_i values for the extended charge depend both on the ion velocity v and on the relative number of electrons ν. Figure 1 shows the ionization cross sections for a hydrogen atom interacting with partly stripped uranium ions U^{6+}. The cross sections were calculated by formula (5) for ions with $Z = 92$ and the number of electrons $N_i = 86$ corresponding to the apparent ion charge $Z^* = 6$, while the screening parameter $\lambda = 0.116$ (in atomic units) was determined by formula (2).

Now let us consider the double ionization of a helium atom. According to [12, 13], calculation of the corresponding cross section does not require using the method of solution matching. The double ionization cross section can be determined directly by formula (1), in which the integration with respect to d^2b can be extended over the whole plane of the impact parameter:

$$\sigma^{2+} = \iiint \left|\langle \mathbf{k}_1, \mathbf{k}_2 | \exp(i\mathbf{q}\{\mathbf{r}_1 + \mathbf{r}_2\}) | 0, 0\rangle\right|^2 d^3\mathbf{k}_1 d^3\mathbf{k}_2 d^2 b. \tag{7}$$

Here $|\mathbf{k}_1, \mathbf{k}_2\rangle$ is the wave function of a helium atom with two electrons in the continuum possessing the momenta $\mathbf{k}_1$ and $\mathbf{k}_2$; $|0, 0\rangle$ is the wave function of helium in the ground state. In the calculation, the wave functions were represented as symmetrized products of the hydrogen-like one-electron wave functions of helium with the same effective nuclear charge $Z_c = 1.97$ (according to [13], this effective charge ensures a good agreement with the experimental data for the double ionization of helium by impact with a fully stripped relativistic ion). The results of these calculations are presented in Fig. 2, which shows the double ionization cross section of helium by partly stripped iron ions Fe^{15+} of various energies. The cross sections were calculated by formula (7) for an ion with $Z = 26$, $N_i = 11$, $Z^* = 15$, and $\lambda = 0.096$ determined by formula (2).

As can be seen from Figs. 1 and 2, the effect of extended ion charge increases with the energy of projectiles and leads to a considerable increase in both single and double ionization cross sections as compared to the values for the point charge. This behavior of the ionization cross sections is quite clear from the general physical considerations. Indeed, in the case of large impact parameters, an impinging ion interacts with atomic electrons like a point charge equal to the apparent charge of the screened ion (in our notation Z^*). In the collisions with small impact parameters, the ion interacts with electrons as the fully stripped charge Z. The cross section reflects contributions from all regions of the impact parameter. Since Z is greater than Z^*, the atomic electrons effectively interact with an ion possessing a charge greater than Z^*. This results in an effective increase in the cross section, which can be significant for $Z \gg Z^*$.

In order to evaluate the effect of the ion charge extension, let us introduce the relative increment $\chi_H = (\sigma_i - \sigma_{i(point)}/\sigma_{i(point)})$, where $\sigma_{i(point)}$ is the ionization cross section of hydrogen by a point ion possessing the same charge Z^* and relative velocity as the extended ion. Let r be the effective radius such that $\sigma_{i(point)} = \pi r^2$. Based on the simple geometric considerations (whereby the screened ion is considered as a ball of radius λ), the cross section of an extended ion can be evaluated as $\sigma_i \sim \pi(r + \lambda)^2$. Then, for $\lambda \ll r$ (which is valid in the cases studied above), we readily obtain an estimate for χ_H using the calculated values of $\sigma_{i(point)}$ for ionization by the point ion and λ for the effective ion radius: $\chi_H \sim 2\lambda/r = 2\pi^{1/2}\lambda/[\sigma_{i(point)}]^{1/2}$. Thus, as the $\sigma_{i(point)}$ value decreases with the energy, the relative increment χ_H grows. As can be seen, the cross sections in Figs. 1 and 2 are consistent with these conclusions. This behavior is probably common for all cross sections of the inelastic processes accompanying the collisions of relativistic structural heavy ions with atoms.

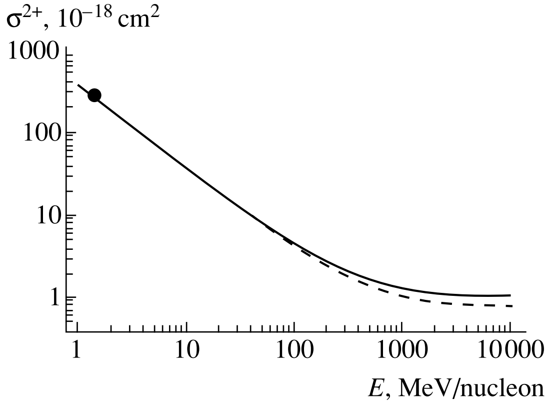

Fig. 2. The double ionization cross section for a helium atom colliding with partly stripped iron ions Fe^{15+}. Solid and dashed curves refer to extended and point ions with the same charge and energy, respectively; black circle shows the experimental result for Fe^{15+} + He collisions [6].

Acknowledgments. This study was supported by the Russian Foundation for Basic Research (project no. 01-02-17047) and by the Ministry of Education of the Russian Federation (project no. E00-3.1-390).

REFERENCES

1. H. F. Krause, C. R. Vane, S. Datz, *et al.*, Phys. Rev. A **63**, 032711 (2001).
2. T. Ludziejewski, Th. Stohlker, D. C. Ionescu, *et al.*, Phys. Rev. A **61**, 052706 (2000).
3. E. Wells, I. Ben-Itzhak, K. D. Carnes, *et al.*, Phys. Rev. A **60**, 3734 (1999).
4. M. Tschersich, R. Drozdowski, M. Busch, *et al.*, J. Phys. B **32**, 5539 (1999).
5. M. B. Shah and H. B. Gilbody, J. Phys. B **16**, L449 (1983).
6. J. H. McGuire, A. Mueller, B. Schuch, *et al.*, Phys. Rev. A **35**, 2479 (1987).
7. H. Berg, J. Ullrich, E. Bernstein, *et al.*, J. Phys. B **25**, 3655 (1992).
8. M. Purkait, A. Dhara, S. Sounda, and C. R. Mandal, J. Phys. B **34**, 755 (2001).

9. C. Illescas, B. Pons, and A. Riera, Phys. Rev. A **63**, 062722 (2001).
10. G. L. Yudin, Dokl. Akad. Nauk SSSR **282**, 874 (1985) [Sov. Phys. Dokl. **30**, 488 (1985)].
11. G. L. Yudin, Zh. Tekh. Fiz. **55**, 9 (1985) [Sov. Phys. Tech. Phys. **30**, 4 (1985)].
12. V. I. Matveev and S. G. Tolmanov, Zh. Éksp. Teor. Fiz. **107**, 1780 (1995) [JETP **80**, 989 (1995)].
13. V. I. Matveev and Kh. Yu. Rakhimov, Zh. Éksp. Teor. Fiz. **114**, 1646 (1998) [JETP **87**, 891 (1998)].
14. V. I. Matveev and D. U. Matrasulov, J. Phys. B **33**, 2721 (2000).
15. T. Ludziejewski, Th. Stohlker, D. C. Ionescu, *et al.*, Phys. Rev. A **61**, 052706 (2000).
16. A. B. Voitkiv, C. Muller, and N. Grun, Phys. Rev. A **62**, 062701 (2000).
17. G. Maynard, D. Gardes, M. Chabot, *et al.*, Nucl. Instrum. Methods Phys. Res. B **146**, 88 (1998).
18. G. Maynard, M. Chabot, and D. Gardes, Nucl. Instrum. Methods Phys. Res. B **164–165**, 139 (2000).
19. W. Brandt and M. Kitagawa, Phys. Rev. B **25**, 5631 (1982).

Translated by P. Pozdeev

Technical Physics Letters, Vol. 28, No. 6, 2002, pp. 501–503. Translated from Pis'ma v Zhurnal Tekhnicheskoĭ Fiziki, Vol. 28, No. 12, 2002, pp. 27–32.
Original Russian Text Copyright © 2002 by Shagaev.

Increasing Thermal Stability of Devices Employing Backward Volume Magnetostatic Waves in Cubic Ferrite Films

V. V. Shagaev
Institute of Materials for Electronic Technologies, Kaluga, Russia

Received October 16, 2001

Abstract—A new method for the thermal stabilization of parameters of devices employing magnetostatic waves (MSWs) in ferrite films is proposed. The method is based on the dependence of the temperature coefficient of frequency on the magnetizing field orientation relative to the crystallographic axes of the film. Possibilities of the new method are demonstrated for the iron yttrium garnet films, the properties of which allow the thermal stability of frequency-selective MSW devices to be significantly improved. © *2002 MAIK "Nauka/Interperiodica".*

The most effective methods for the thermal stabilization of parameters of devices employing magnetostatic waves (MSWs) in ferrite films are based on the temperature-induced variations of the demagnetizing field in the film [1, 2]. These methods pose significant restrictions on the design of MSW devices, requiring either sloped orientation of the film in the magnetic field or specially selected ("thermostable") dimensions of the film.

The purpose of this study was to develop a method for the thermal stabilization of the frequency of backward volume magnetostatic waves (BVMSWs) in a tangentially magnetized cubic ferrite film. It was assumed that the film size allows the effect of demagnetizing field on the temperature-induced frequency variations of BVMSWs to be ignored. According to [2], the temperature-compensating effect of the demagnetizing field is pronounced when the ratio of film thickness to lateral size in the magnetization direction is greater than 0.1. When this ratio is on the order of 0.01, the temperature-induced frequency shift is close to the values characteristic of a film with infinite lateral dimensions.

The proposed method is based on the dependence of the temperature coefficient of frequency (TCF) on the magnetizing field orientation relative to the crystallographic axes of the film.

The main source of thermal instability of the MSW characteristics is the temperature dependence of the saturation magnetization of ferrite. At first glance, it appears that the proposed method can be realized only in strongly anisotropic materials where the magnetic anisotropy field is on the same order of magnitude as the saturation magnetization. However, at present, the main material for the spin-wave electronics is yttrium iron garnet (YIG) belonging to weakly anisotropic ferrites. Possibilities of the new method will be demonstrated in application to the YIG films.

Let us consider the factors influencing the temperature-induced shift of the BVMSW frequency in anisotropic ferrite films. In constructing a theoretical model, we will proceed from the dispersion equation in a zero-exchange approximation derived in a traditional way [3]. In the case of $\mathbf{M} \perp \mathbf{n}$ and $\mathbf{k} \parallel \mathbf{M}$, where $\mathbf{M}$ is the magnetization vector, $\mathbf{n}$ is the film normal, and $\mathbf{k}$ is the wave vector, the MSW dispersion equation can be written as [4]

$$\tan\left(\frac{kd}{\sqrt{-\mu_{xx}}}\right) = \frac{2\sqrt{-\mu_{xx}}}{1+\mu_{xx}}, \tag{1}$$

where d is the film thickness and μ_{xx} is the magnetic permeability tensor component in the coordinate system (x, y, z) with the axes $x \parallel \mathbf{n}$ and $z \parallel \mathbf{M}$. The latter quantity is given by the formula

$$\mu_{xx} = \frac{f_l^2 - f^2}{f_s^2 - f^2}, \tag{2}$$

where f is the variable frequency, f_l and f_s are the long-wave and shortwave boundary frequencies of the BVMSW spectrum

$$\left(\frac{f_l}{g}\right)^2 = [H_z + M(N_{yy}^c - N_{zz}^c)]$$
$$\times [H_z + M(N_{xx}^c - N_{zz}^c) + 4\pi M - H_u] - (MN_{xy})^2,$$
$$\left(\frac{f_s}{g}\right)^2 = [H_z + M(N_{yy}^c - N_{zz}^c)]$$
$$\times [H_z + M(N_{xx}^c - N_{zz}^c) - H_u] - (MN_{xy})^2,$$

$g = 2.8$ MHz/Oe is the gyromagnetic ratio, H_z is the projection of the external magnetic field onto the direction

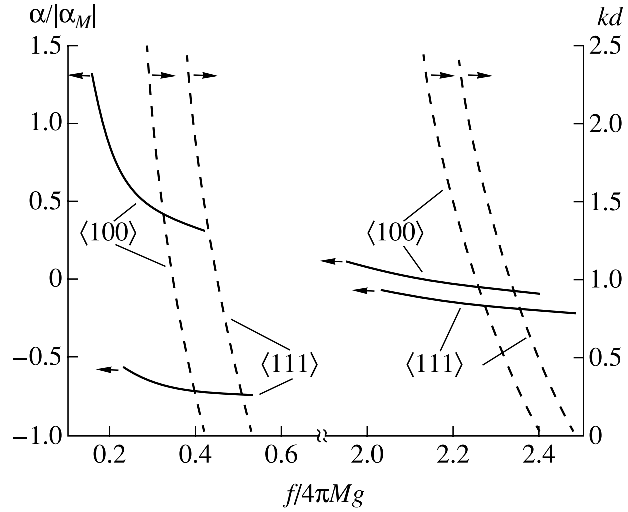

Fig. 1. The temperature coefficient of frequency (solid curves) and the principal mode dispersion (dashed curves) of BVMSWs in ferrite films calculated for $4\pi M = 1750$ G, $H_c = -42$ Oe, $d(4\pi M)/dT = -4.0$ G/K, and $dH_c/dT = 0.4$ Oe/K; $\alpha_M \equiv (1/4\pi M)[d(4\pi M)/dT]$; magnetization directions indicated at the curves.

of vector **M**, N_{ij}^c are the effective demagnetizing factors of the crystallographic magnetic anisotropy, $H_u = 2K_u/M$ is the uniaxial normal anisotropy field with the first constant K_u [3], and $4\pi M$ is the saturation magnetization of the ferrite crystal.

Let us simplify description of the crystallographic orientation of **M** by considering the magnetization directions coinciding with the third- and fourth-order symmetry axes of the ferrite crystal. In this context, further analysis refers to the films of cubic ferrites with a surface oriented in the {110} direction. In this case, the film plane contains the symmetry axes ⟨111⟩ and ⟨100⟩. The effective demagnetizing factors for these directions are described by the relationships

$$M(N_{xx}^c - N_{zz}^c) = M(N_{yy}^c - N_{zz}^c) = H_c N_{\langle pqr\rangle},$$
$$N_{xy} = 0,$$

where $H_c = K_c/M$ is the cubic anisotropy field with the first constant K_c, $N_{\langle 111\rangle} = -4/3$, and $N_{\langle 100\rangle} = 2$; note also that $H_z = H$.

An expression for the temperature derivative df/dT can be obtained from formulas (1) and (2), taking into account that kd = const and, hence, $d\mu_{xx}/dT = 0$. After simple transformations, we obtain the following expression for the TCF:

$$\alpha \equiv \frac{1}{f}\frac{df}{dT} = \frac{1}{2}\left[\left(1-\frac{g^2H_{\text{in}}^2}{f^2}\right)\frac{1}{4\pi M}\frac{d(4\pi M)}{dT} + \left(1+\frac{g^2H_{\text{in}}^2}{f^2}\right)\frac{N_{\langle pqr\rangle}}{H_{\text{in}}}\frac{dH_c}{dT} - \frac{4\pi M H_{\text{in}}g^2}{f^2}\frac{d(H_u/4\pi M)}{dT}\right], \qquad (3)$$

where $H_{\text{in}} = H + N_{\langle pqr\rangle}H_c$ is the internal effective field strength.

Figure 1 shows the plots of $\alpha(f)$ and $kd(f)$ calculated using the parameters of YIG single crystals [5, 6]. Note that the effect of the crystallographic magnetic anisotropy on the TCF is related both the product $N_{\langle pqr\rangle}H_c$ and to the temperature derivative. The contribution to α due to the term $N_{\langle pqr\rangle}dH_c/dT$ increases with decreasing H_{in}. From this it follows, in particular, that the difference between $\alpha_{\langle 111\rangle}$ and $\alpha_{\langle 100\rangle}$ (the subscript refers to the orientation of **M**) increases with decreasing magnetization field strength. This feature is confirmed by analysis of the data in Fig. 1.

The most interesting situation takes place for $\alpha_{\langle 111\rangle}$ and $\alpha_{\langle 100\rangle}$ possessing the opposite signs. In this case, there is a "thermostable" crystallographic direction between the tangent axes ⟨111⟩ and ⟨100⟩, for which $df/dT = 0$. It should be noted that we assume a continuous dependence of α on the angles determining the orientation of vector **M**. An analysis based on the laws of dispersion describing the general case with an arbitrary crystallographic orientation of **M** [7, 8] confirms the absence of discontinuities in the angular dependence of α. Using the method described in [7], it is also possible to calculate the external field **H** proceeding from the given "thermostable" direction **M** and the internal field strength.

Let us analyze the signs of $\alpha_{\langle 111\rangle}$ and $\alpha_{\langle 100\rangle}$. For YIG, the condition $\alpha_{\langle 111\rangle} < 0$ is valid for any H in the entire frequency spectrum of BVMSW frequencies. On the contrary, the condition $\alpha_{\langle 100\rangle} \geq 0$ leads to restrictions with respect to H and f values. In particular, the TCF values will be nonnegative in the entire BVMSW frequency spectrum provided that the minimum $\alpha_{\langle 100\rangle}$ value attained at the longwave boundary ($f = f_l$) is nonnegative:

$$(df_l/dT)_{\langle 100\rangle} \geq 0.$$

Using the expressions derived above and accomplishing the necessary transformations, we obtain

$$H \leq H_0,$$

$$H_0 = -2\left[\frac{4\pi M_{\text{eff}}(dH_c/dT)}{d(4\pi M_{\text{eff}})/dT + 4(dH_c/dT)} + H_c\right],$$
$$4\pi M_{\text{eff}} = 4\pi M - H_u.$$

Thus, the theoretical analysis predicts the existence of a threshold field strength $H = H_0$ below which $\alpha_{\langle 100\rangle}$ is positive in the entire BVMSW frequency spectrum ($f_s < f \leq f_l$). In particular, for YIG this value is $H_0 \approx$ 670 Oe.

The experiments were performed with a 10.6-μm-thick YIG film possessing the lateral dimensions 15 × 15 mm grown on a gadolinium gallium garnet substrate oriented in the {110} direction. Note that the ratio of

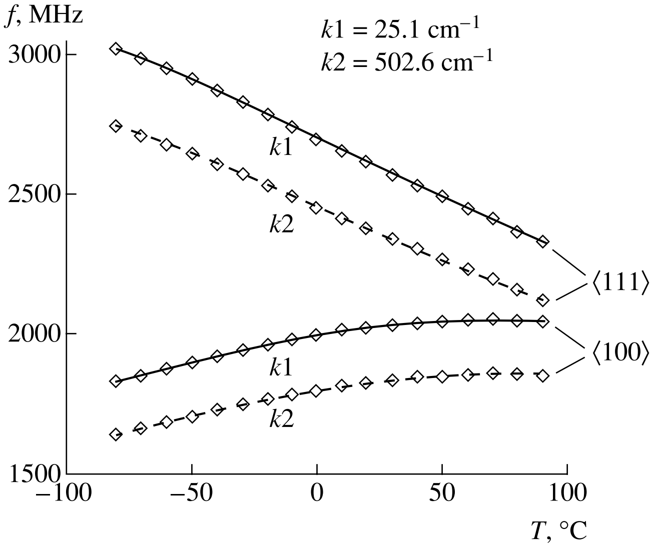

Fig. 2. Experimental plots of the principal mode frequency versus temperature for BVMSWs with two wave vectors in a YIG film magnetized along the tangent axes ⟨111⟩ and ⟨100⟩ in the external magnetic field with a strength of H = 350 Oe.

film thickness to lateral size is two orders of magnitude smaller than the value [2] for which the demagnetizing field effect is significant. The results of measurements are presented in Fig. 2. The character of the experimental curves is consistent with the concepts developed above: the sign of TCF exhibits inversion in a small magnetization field, when the field orientation changes between the tangent axes ⟨111⟩ and ⟨100⟩.

Using the properties of ferrite films described above, it is possible to improve the thermal stability of frequency-selective MSW devices. In addition, by properly selecting the crystallographic orientation of the film surface and the magnetization direction, it is possible to provide for the mutual compensation of both positive and negative variations of the parameters of other elements of MSW devices.

REFERENCES

1. Yu. K. Fetisov, Zh. Tekh. Fiz. **57** (12), 2393 (1987) [Sov. Phys. Tech. Phys. **32**, 1451 (1987)].
2. M. G. Balinskiĭ, A. S. Beregov, I. N. Ereshchenko, and I. A. Nechaev, Élektron. Tekh., Ser. 1: Élektron. SVCh, No. 2 (446), 8 (1992).
3. A. G. Gurevich, *Magnetic Resonance in Ferrites and Antiferromagnets* (Nauka, Moscow, 1973).
4. V. V. Shagaev, Fiz. Tverd. Tela (St. Petersburg) **40** (11), 2089 (1998) [Phys. Solid State **40**, 1892 (1998)].
5. P. Hansen, P. Röschmann, and W. Tolksdorf, J. Appl. Phys. **45** (6), 2728 (1974).
6. P. Hansen, J. Appl. Phys. **45** (8), 3638 (1974).
7. A. S. Beregov and E. V. Kudinov, Élektron. Tekh., Ser. 1: Élektron. SVCh, No. 6 (390), 41 (1986).
8. A. S. Beregov and E. V. Kudinov, Élektron. Tekh., Ser. 1: Élektron. SVCh, No. 6 (400), 8 (1987).

Translated by P. Pozdeev

Technical Physics Letters, Vol. 28, No. 6, 2002, pp. 504–506. Translated from Pis'ma v Zhurnal Tekhnicheskoĭ Fiziki, Vol. 28, No. 12, 2002, pp. 33–39.
Original Russian Text Copyright © 2002 by Kozyrev, Shishkov.

Two Regimes of Heat Exchange between a Metal Particle and a Nonequilibrium Plasma

A. V. Kozyrev* and A. N. Shishkov
Institute of High-Current Electronics, Siberian Division, Russian Academy of Sciences, Tomsk, Russia
** e-mail: kozyrev@to.hcei.tsc.ru*

Received January 23, 2002

Abstract—A theoretical model is developed for the process of energy exchange between a spherical drop and a nonequilibrium plasma. It is demonstrated that, in a certain range of the plasma parameters, a quasistationary temperature of the drop can be maintained in two different heat exchange regimes. In one of these, the energy flux from plasma to drop is compensated by cooling due to the thermal emission of electrons; in the other, the energy supply is equilibrated by intensive evaporation of the drop material. The two regimes, characterized by certain quasistationary temperatures, are separated by a temperature interval featuring unstable states of the system. The particular realization of one or another quasistationary regime is determined by the initial temperature of the drop. *© 2002 MAIK "Nauka/Interperiodica".*

The problem of determining the temperature of macroscopic particles occurring in a plasma, which is very important for numerous applications, has been repeatedly discussed in the literature. Boxman and Goldsmith [1] calculated the temperature of macroparticles in a nonequilibrium vacuum arc plasma without an allowance for the process of thermionic emission and obtained understated values of the temperature. The later theories [2, 3] took into account the thermionic processes on the particle surface, but the equilibrium argon plasma had a relatively low degree of ionization and the temperatures were not high enough to produce intensive evaporation of the particle material.

Recently, Batrakov *et al.* [4] experimentally established for the first time that metal drops leaving a cathode spot of the vacuum arc exhibit intensive evaporation and convert into plasma bunches in the immediate vicinity of the cathode surface. The purpose of this study was to provide for a preliminary theoretical analysis of the possibility of such phenomena.

We will consider the process of heat exchange between a macroparticle occurring in a nonequilibrium near-cathode metal plasma of the vacuum arc, where the density of charged particles is significantly greater than 10^{15} cm^{-3}. It was demonstrated [2] that an important factor in the heat exchange between metal drops and surrounding plasma is that the hot drop can emit thermoelectrons. Being sufficiently intense, this process can significantly influence the potential of the drop relative to the plasma. The flow of electrons and, hence, the flux of thermal energy from plasma to the metal drop is exponentially dependent on this potential. As a result, the drop emitting electrons can heat to a higher temperature than the same drop not involved in the thermionic emission. The thermionic cooling becomes, together with the cooling due to evaporation of atoms from the drop surface, the main channel of heat removal from the drop. Thus, we can suggest that there are two possible regimes of heat exchange between a metal drop and plasma: (i) the usual regime with a relatively large negative floating potential, whereby the main channel of energy removal from the drop is thermal radiation, and (ii) an emission regime with a relatively low (compared to the thermal electron energy kT_e) floating potential, whereby the main channel of heat exchange is related to the flow of evaporated atoms and emitted electrons.

It will be specially indicated that the transition from the usual to emission regime takes place in a certain interval of plasma densities and possesses a hysteresis character.

Let us consider an immobile spherical drop occurring in a sufficiently dense nonequilibrium plasma with the known ion density n_0, average ion charge Z, and the electron and ion temperatures $T_e > T_i$. The drop radius is assumed to be sufficiently small compared to the mean free path of the plasma particles, but still much greater than the field screening radius $r_D = \sqrt{\epsilon_0 k T_e / q^2 n_0}$ (where ϵ_0 is the dielectric constant and q is the elementary charge). Under these conditions, the drop can be considered a Langmuir probe, the stationary parameters of which will be independent of the radius [3].

Within the framework of this model, we have calculated a dimensionless stationary floating potential of the drop $\psi_d = q|\phi_d|/kT_e$, which is determined by the balance of charged particle flows, and a stationary temperature of the drop T_d determined by the balance of energy fluxes. The calculation was performed with an allowance for the thermal energy fluxes from plasma to particles, the thermal effects related to the evaporation of atoms and the emission of electrons, the liberation of energy due to the recombination of ions on the drop surface, and the radiative energy losses.

Expressions for the flows of electrons (Γ_e^{pl}) and ions (Γ_i^{pl}) from the plasma to a wall are well known [5]. In the general case, these quantities are complicated functions of the drop potential and the plasma parameters. In the limiting cases, the system is well described by the simple approximated relationships

$$\begin{aligned}\Gamma_e^{pl} &= 4\pi R^2 Z n_0 \sqrt{8kT_e/\pi m}\, f_e(\psi_d),\\ \Gamma_i^{pl} &= 4\pi R^2 n_0 \sqrt{8kT_i/\pi M}\, f_i(\psi_d).\end{aligned} \tag{1}$$

Here, m and M are the masses of electrons and ions, respectively; $f_e = \exp(-\psi_d)/4$ and $f_i \approx 0.3\sqrt{T_e/T_i}$ for $\psi_d \gg 1$; $f_e \approx \exp(-\psi_d)/2$ and $f_i \approx 1/2$ for $0 < \psi_d < 1$. An analysis showed that the floating potential of the emitting drop in a nonequilibrium plasma does not change sign; this conclusion was confirmed by the results reported in [2].

In contrast to the approach employed in [2], we have calculated the flow of thermoelectrons Γ_e^{em} with an allowance for the Schottky effect (a decrease in the electron work function of a material exposed to a strong electric field) and a virtual cathode effect, whereby the thermionic current is limited by the space charge field. In the latter case, we also took into account the effect of the virtual cathode upon the flow of electrons from plasma (Γ_e^{pl}). At high temperatures of the drop, when the current of thermoelectrons is effectively limited by the space charge, an electric double layer is formed at the drop surface. The calculation showed that the electron current density is completely determined by the ion current from plasma and can be calculated by a simple formula:

$$\Gamma_e^{em} \approx \sqrt{M/m}\,\Gamma_i^{pl}. \tag{2}$$

Thus, at low temperatures T_d, the drop possesses a relatively large potential ψ_d and the emission flow Γ_e^{em} obeys the Richardson–Dushman law. At high temperatures, the potential ψ_d sharply decreases and the thermionic flow is determined by relationship (2). It is this limitation of the emission current that renders the thermionic cooling mechanism incapable of stabilizing the drop temperature, so that the effective heat removal is provided by evaporation of the drop material. It should be noted that the presence of the virtual cathode may explain the difference of the effective electron work function of tungsten (≈6 eV), observed for a sample placed in a dense plasma [3], from the commonly accepted value (4.5 eV).

Let us write approximate expressions for the energy fluxes considered in the proposed model, comprising the thermal energy flux W^{in} supplied from plasma (heating the drop) and the flux of removed energy W^{out} (cooling the drop):

$$\begin{aligned} W^{in} &\approx \Gamma_e^{pl}(\psi_d)(\varphi_e + 2kT_e)\\ &+ \Gamma_i^{pl}(\psi_d)(\varphi_a + I_Z - Z\varphi_e + Zq\phi_d + 2kT_i),\end{aligned} \tag{3}$$

$$\begin{aligned} W^{out} &\approx \Gamma_e^{em}(T_d)(\varphi_e + 2kT_d)\\ &+ \Gamma_a^{ev}(T_d)(\varphi_a + 2kT_d) + W^{rad}(T_d).\end{aligned} \tag{4}$$

Here, φ_e is the effective electron work function calculated with an allowance for the Schottky effect, φ_a is the energy of evaporation per atom, and I_Z is the energy of the Z-fold ionization of an atom. The flow of evaporated atoms $\Gamma_a^{ev}(T_d)$ was calculated proceeding from the known temperature dependence of the saturated vapor pressure, while the radiative energy flux $W^{rad}(T_d)$ was assumed to be proportional to T_d^4.

We have analyzed a solution of the combined system of equations describing the balance of charge and energy of the drop with unknown ψ_d and T_d values:

$$\begin{aligned}\Gamma_e^{pl}(\psi_d) &= \Gamma_i^{pl}(\psi_d) + \Gamma_e^{em}(T_d),\\ W^{in}(\psi_d) &= W^{out}(\psi_d, T_d).\end{aligned} \tag{5}$$

This system always possesses at least one solution. The solutions for low and high temperatures of the drop correspond to the well-known regimes [2]. A new type of possible solutions appears in the region of intermediate temperatures T_d, where the floating potential of the drop exhibits a smooth decrease. In this region, system (5) usually admits three possible solutions.

This can be illustrated by an example of calculation of the temperature of a tungsten drop in a plasma with parameters close to those in a vacuum arc. Figure 1 shows the temperature variation of the energy fluxes and the floating potential of the drop. As can be seen, there are three points of intersection of the curves $W^{in}(T_d)$ and $W^{out}(T_d)$, which correspond to a certain "equilibrium" temperature of the drop. The middle point corresponds to an unstable equilibrium. At a small deviation from the middle equilibrium point, the energy balance is broken in an irreversible manner. Upon a spontaneous decrease in the temperature, the energy $W^{in}(T_d)$ supplied from plasma becomes smaller than the energy $W^{out}(T_d)$ removed from the drop, so that the cooling will continue. Upon a spontaneous increase in the temperature, $W^{in}(T_d) > W^{out}(T_d)$ and the temperature would grow further. The two other equilibrium points are stable with respect to the temperature fluctuations and, hence, may correspond to physically realizable states.

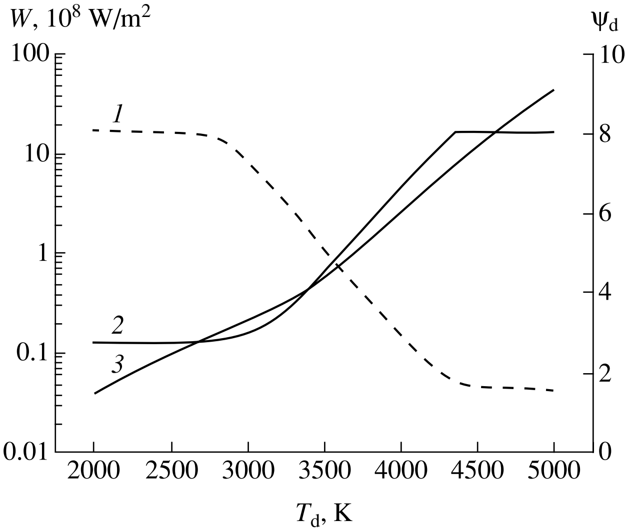

Fig. 1. The plots of (*1*) the floating potential ψ_d and the quasistationary energy fluxes (*2*) W^{in} and (*3*) W^{out} versus temperature T_d calculated for a spherical tungsten drop in a vacuum arc plasma with the parameters $n_0 = 3.5 \times 10^{15}$ cm^{-3}, $Z = 2$, and $kT_e = 4$ eV.

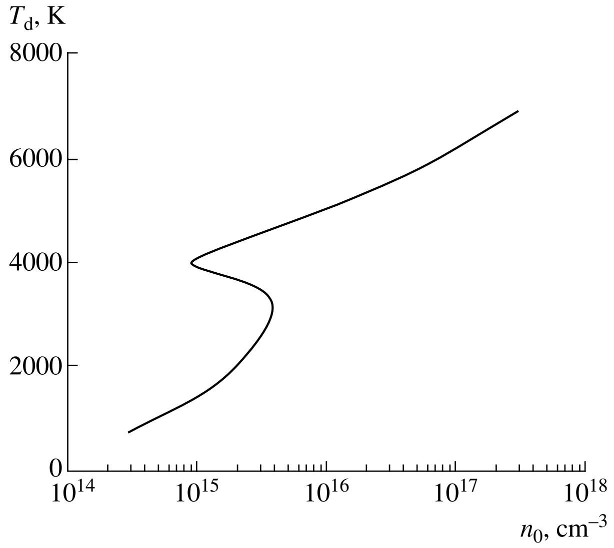

Fig. 2. The plot of a quasistationary temperature of a tungsten drop T_d versus plasma density n_0.

Figure 2 shows the plots of equilibrium temperature of the tungsten drop calculated as a function of the plasma density. The middle region of the $T_d(n_0)$ curve corresponds to unstable states, while the upper and lower branches of the curve represent stable solutions. As can be seen from this figure, ambiguity of the stationary temperature of the drop may take place only in a limited interval of the plasma densities. The formal selection of a particular stationary solution of the system (5) is determined by the initial temperature: should this temperature be above the “unstable” point, the stationary temperature is determined on the upper branch; for an initial temperature below the “unstable” point, the stable temperature is found on the lower branch. From the standpoint of physics, the curve in Fig. 2 is of large value for estimating the rate of material evaporation from microscopic drops ejected from a cathode spot of the vacuum arc.

Since the drops are ejected from a region of high plasma density, the drop temperature (at a sufficiently small velocity) must tend to stationary solutions in the vicinity of the upper branch of the $T_d(n_0)$ curve, up to relatively low plasma densities ($n_0 \simeq 10^{15}$ cm^{-3}). Even if the initial temperature was not very large, a slowly moving drop will be heated up to $T_d > 4000$ K and this high temperature will be maintained during a sufficiently long time. As a result, slowly moving drops far from the cathode spot may be significantly smaller in size as compared to the initial particles.

On the contrary, relatively fast drops flying across a region of high plasma density may be not strongly heated and possess a quasistationary temperature in the vicinity of the lower stable branch of the $T_d(n_0)$ curve. The rate of evaporation of such (relatively cold) drops will be significantly lower as compared to the case of slow drops considered above, and their dimensions will not change significantly as compared to the initial values.

We have used system (5) to calculate the temperatures of drops of various materials. It was found that most metals, including copper, and carbon (graphite) show qualitatively the same behavior of $T_d(n_0)$ as does tungsten. Only readily evaporated metals such as gallium exhibited no region featuring ambiguous solutions for the temperature. This is quite clear since the heat exchange by evaporation in such metals would stabilize the drop temperature before a flow of thermoelectrons will arise capable of decreasing the floating potential and increasing the thermal energy flux from the plasma.

Acknowledgments. This study was supported by the Russian Foundation for Basic Research, project no. 99-02-18163.

REFERENCES

1. R. Boxman and S. Goldsmith, J. Appl. Phys. **52** (1), 151 (1981).
2. A. G. Gnedovets and A. A. Uglov, Teplofiz. Vys. Temp. **29** (6), 1184 (1991).
3. Xi Chen, Ji Chen, and Yandan Wang, J. Phys. D **27**, 1637 (1994).
4. A. V. Batrakov, N. I. Vogel, S. A. Popov, *et al.*, IEEE Trans. Plasma Sci. **30** (1) (2002).
5. *Thermionic Converters and Low Temperature Plasma*, Ed. by B. Ya. Moĭzhes and G. E. Pikus (Nauka, Moscow, 1973), Chap. 6.

Translated by P. Pozdeev

Technical Physics Letters, Vol. 28, No. 6, 2002, pp. 507–509. Translated from Pis'ma v Zhurnal Tekhnicheskoĭ Fiziki, Vol. 28, No. 12, 2002, pp. 40–47.
Original Russian Text Copyright © 2002 by Shevyakhov.

A Noncollinear TM Surface Wave Propagating at the Moving Plasma–Vacuum Interface

N. S. Shevyakhov

Ul'yanovsk Branch, Institute of Radio Engineering and Electronics, Russian Academy of Sciences,
Ul'yanovsk, 432000 Russia
e-mail: ufire@mv.ru

Received January 18, 2002

Abstract—The conditions of existence and the dispersion properties of a noncollinear TM electromagnetic surface wave propagating at the moving interface between a low-temperature isotropic collisionless plasma and vacuum are studied. It is found that the boundary motion shifts the surface wave normal out of the interface and inclines it toward the direction of motion. The possibility of using the moving interface for a substantial transformation of the TM surface wave spectrum in the cutoff frequency region is pointed out. *© 2002 MAIK "Nauka/Interperiodica".*

Recent studies [1–6] showed that moving solid phase boundaries are capable of guiding specific noncollinear acoustic modes. The noncollinearity of these modes is manifested by the wave normal being shifted out of the interface plane and forming an acute angle with the direction of motion. The well-known and repeatedly confirmed concept of L.I. Mandel'shtam that oscillatory and wave processes are similarly manifested in different physical systems [7] allows us to assume that this property is inherent not only in acoustic waves. We expect that, under proper conditions, electromagnetic, plasma, and other surface waves will demonstrate similar behavior.

This communication shows for the first time the possibility for noncollinear electromagnetic surface waves to exist at the plasma–vacuum interface moving with a nonrelativistic velocity. Note that we consider TM electromagnetic surface waves whose behavior at the stationary (immobile) interfaces between plasma and dielectric media was studied in sufficient detail [8].

The sharp plasma–vacuum interface can roughly be treated as a geometrical model of the photoionization front traveling in a rarefied interstellar medium at the boundary of the shadow formed behind a moving atmosphereless cosmic body.[1] In the absence of an external magnetic field, the illuminated region can be treated as a low-temperature isotropic plasma [9] and the shadow zone, as a vacuum.

The collisionless cold isotropic plasma occupying the region $y > V_s t$ in the laboratory frame of reference $x0yz$ (where $V_s = \beta c$, V_s is the velocity of the interface, c is the speed of light, and t is time) has the current density $\mathbf{j} \simeq -en_0\mathbf{v}$, where the electron velocity $\mathbf{v}$ is determined from the equation of motion $\partial\mathbf{v}/\partial t \simeq -e\mathbf{E}/m_e$. From the Maxwell equations, we obtain that the electric field $\mathbf{E}$ in the plasma satisfies the equation

$$\frac{1}{c^2}\frac{\partial^2\mathbf{E}}{\partial t^2} + \mathrm{curl}(\mathrm{curl}\mathbf{E}) + \frac{\Omega_e^2}{c^2}\mathbf{E} = 0. \qquad (1)$$

Here, $\Omega_e = (4\pi e^2 n_0/m_e)^{1/2}$ is the plasma frequency, n_0 is the electron density, e is the electron charge, and m_e is the electron mass. The field $\mathbf{E}_0$ in vacuum (at $y < V_s t$) is the solution to Eq. (1) with $\Omega_e = 0$.

It is convenient to consider a TM surface wave with fields $\mathbf{E} = (E_x, E_y)$ and $\mathbf{E}_0 = (E_x^{(0)}, E_y^{(0)})$ using the rest frame $\tilde{x}O\tilde{y}\tilde{z}$ with the $\tilde{z}$ axis situated in the interface plane and the $\tilde{y}$ axis normal to the interface. For $\beta \ll 1$, we can assume without loss of accuracy that the frames $xOyz$ and $\tilde{x}O\tilde{y}\tilde{z}$ are related by the Galilean transformation: $x = \tilde{x}$, $z = \tilde{z}$, $t = \tilde{t}$, and $y = \tilde{y} + V_s\tilde{t}$. Then it follows that, after passing to the rest frame, we should change only the time variable: $\partial/\partial t \longrightarrow \partial/\partial\tilde{t} - V_s\partial/\partial\tilde{y}$. In view of this change and the fact that fields $\mathbf{E}$ and $\mathbf{E}_0$ are finite ($\mathbf{E}$, $\mathbf{E}_0 \sim \exp(i\phi_\parallel)$, where $\phi_\parallel = k_\parallel\tilde{x} - \Omega\tilde{t}$), we obtain from (1) that

$$E_x = E_0\exp(i\phi)\exp(-s\tilde{y}),$$
$$E_y = -\frac{ik_\parallel}{ip - s}E_x \quad (\tilde{y} > 0), \qquad (2)$$

$$E_x^{(0)} = E_0^{(0)}\exp(i\phi)\exp(s_0\tilde{y}),$$
$$E_y^{(0)} = -\frac{ik_\parallel}{ip + s_0}E_x \quad (\tilde{y} < 0). \qquad (3)$$

---

[1] Another example of this kind is the ionized gas behind the front of a shock wave.

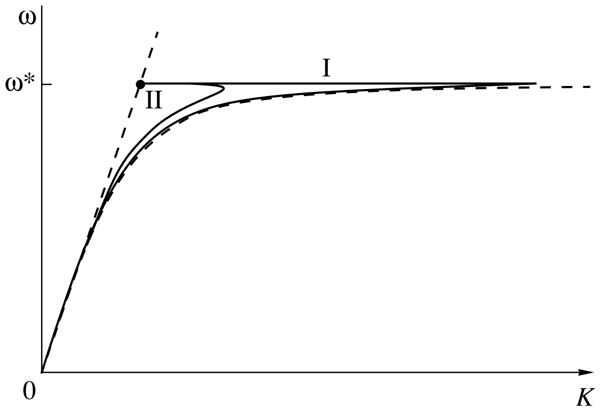

Fig. 1. General pattern of the spectrum of a TM surface wave propagating at the moving plasma–vacuum interface.

Here, $\phi = \phi_\parallel + p\tilde{y}$ is the phase of the TM wave written taking into account the noncollinearity of its wave normal; $k_\parallel$ and $p = k_\perp$ are the longitudinal and transverse components of the wave vector, respectively; and Ω is the oscillation frequency measured in the interface rest frame.

The degree of noncollinearity is determined by the parameter p defined as

$$p = \frac{\Omega}{c}\frac{\beta}{1-\beta^2}. \qquad (4)$$

Formula (4), together with Eqs. (2) and (3) and the relations

$$s^2 - s_0^2 = \frac{\Omega_e^2}{c^2(1-\beta^2)}, \quad s_0 = \frac{1}{1-\beta^2}\sqrt{(1-\beta^2)k_\parallel^2 - \frac{\Omega^2}{c^2}}, \qquad (5)$$

provide for the description of changes in the dispersion properties and structure of a TM surface wave (perceived by an observer situated in the interface rest frame as an “incursion” of plasma) that is adequate for the adopted nonrelativistic relation between the inertial frames of reference. Expressions for the magnetic field components which are involved in the standard boundary conditions of continuity at $\tilde{y} = 0$ are given by

$$H_z = c\frac{k_\parallel^2 - (ip - s)^2}{(ip - s)[i(\Omega + pV_s) - sV_s]}E_x, \quad \tilde{y} > 0, \qquad (6)$$

$$H_z^{(0)} = c\frac{k_\parallel^2 - (ip + s_0)^2}{(ip + s_0)[i(\Omega + pV_s) + s_0V_s]}E_x^{(0)}, \quad \tilde{y} < 0. \qquad (7)$$

These formulas were derived from the Maxwell equations curl$\mathbf{E} = -\partial\mathbf{H}/\partial t$ and curl$\mathbf{E}^{(0)} = -\partial\mathbf{H}^{(0)}/\partial t$ with account for Eqs. (2) and (3). Matching the magnetic field components (6) and (7) at $\tilde{y} = 0$ and using the equality $E_x|_{\tilde{y}=0} = E_x^{(0)}|_{\tilde{y}=0} \equiv E_0$, we arrive (after splitting the obtained dispersion relation into the real and imaginary parts) at the following equations:

$$\frac{\Omega_e^2}{\omega^2 + s^2V_s^2} = s_0(1-\beta^2)\frac{s + s_0}{p^2 + s_0^2}, \qquad (8)$$

$$s\beta\frac{\Omega_e^2}{\omega^2 + s^2V_s^2} = \frac{\omega^2}{c^2}\beta(1-\beta^2)\frac{s + s_0}{p^2 + s_0^2}, \qquad (9)$$

where $\omega = \Omega + pV_s \equiv \Omega/(1-\beta^2)$ is the oscillation frequency in the laboratory frame of reference.

Equations (8) and (9) give no way of deriving a standard dispersion relation $\omega = \omega(K)$ for a fixed $\beta \neq 0$. The reason is that the system obtained is overdetermined because we neglected electron collisions in the plasma. For the collisionless plasma, a relationship between the total wave number $K = (k_\parallel^2 + p^2)^{1/2}$ and ω can be obtained assuming applicability of the nonrelativistic approximation in the asymptotic limit $\beta \longrightarrow 0$. Then (9) is identically satisfied and (8) yields, in the first approximation to $\tilde{s}_0 = s_0|_{\beta=0}$ and $\tilde{s} = s|_{\beta=0}$ (with account for the equality $(s + s_0)/(p^2 + s_0^2) \approx \Omega_e^2/\omega^2\tilde{s}_0$), the following formula:

$$s_0 \approx \tilde{s}_0\frac{\omega^2(1-\beta^2)^{-1}}{\omega^2 + \tilde{s}^2\beta^2c^2}.$$

As a result, the frequency dependence of the amplitude decay factor for the TM wave in vacuum can be written as

$$s_0 \approx \frac{\Omega_e}{c(1-\beta^2)}\frac{\xi^4(1-2\xi^2)^{1/2}}{\xi^2(1-2\xi^2) + \beta^2(1-\xi^2)^2}, \qquad (10)$$

where $\xi = \omega/\Omega_e$. Using (10) and (5), we can readily determine all remaining characteristics of the TM wave, including the relationship $\omega = \omega(K)$.

Solid lines in Fig. 1 depict typical spectra of the TM surface wave for slowly (curve II) and very slowly (curve I) moving plasma boundary. The upper limit of these curves is the cutoff frequency $\omega^* = \Omega_e/\sqrt{2}$; the lower limit is the dashed curve representing the spectrum of a TM surface wave propagating at the static boundary (in the shortwave limit, it approaches the cutoff frequency [8]). From the left, these curves are bounded by the dashed straight line $\omega = Kc$ depicting the spectrum of volume electromagnetic waves in vacuum. The motion of the plasma boundary causes a looplike turn of the dispersion branches, which is a characteristic of the doubly degenerate modes. In this case, as can be seen from Fig. 2, it is the turning point of the loop at which we observe the maximum localization of the field oscillations in the TM surface wave. Similar features were observed in the spectrum of a magnetoelastic surface wave propagating at the moving domain wall of a ferromagnetic material studied in [4, 5], where these effects were explained by degeneracy of

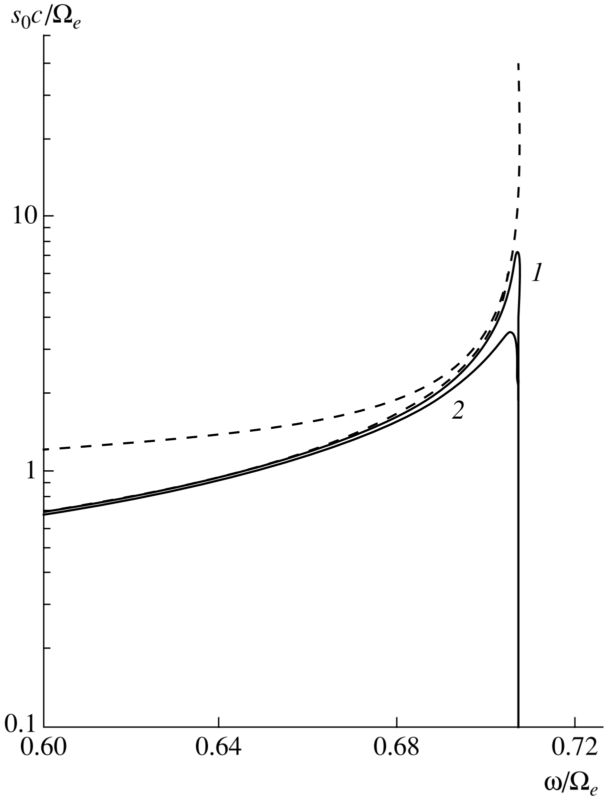

Fig. 2. Frequency characteristics of the localization coefficient s_0 of the TM surface wave propagating at the plasma–vacuum interface, calculated for $\beta = 0.05$ (*1*) and 0.1 (*2*). The upper and lower dashed curves depict functions $s(\omega)$ and $s_0(\omega)$ for the motionless interface, respectively.

the spectral doublet formed by the line of the ferromagnetic resonance (FMR) for near-boundary magnetostatic oscillations and the shortwave edge (separated due to the magnetostriction) of the spectrum of a magnetoelastic surface wave propagating at the stationary domain wall.

For the TM surface wave, the FMR line is replaced with the cutoff frequency. Since the region $\omega < \omega^*$ contains only the branch corresponding to the TM surface wave, the nature of the second degenerate mode is unclear. Let us consider now the frequency range $\omega > \omega^*$. Equation (8) with $\beta = 0$ has a formal solution in the band $\omega^* < \omega < \Omega_e$. This solution has the form of nonpropagating TM oscillations with amplitudes increasing along the plasma boundary (the case of purely imaginary $k_{\parallel}$). Obviously, this solution does not meet the requirement of finite amplitudes of the fields (2), (3), (6), and (7) and must be ignored as nonphysical. At the same time, this solution has an important feature: its cutoff frequency, like that of the TM surface wave, is a limiting frequency; the only difference is that it represents the lower (rather than the upper) edge of the spectrum. Thus, these solutions have a singular relation on the line $\omega = \omega^*$. Because of the mode conversion caused by the boundary motion, this fact is of basic importance.

This circumstance allows us to treat the increasing TM oscillations as a missing (virtual) oscillation mode which degenerates with the TM surface wave at $\beta \neq 0$. Due to the Doppler frequency lowering and the tilt of the wave normal, a segment of the branch near ω^* enters the physically allowed spectral region ($\omega < \omega^*$), where it forms the return (upper) part of the turning loop in the dispersion curve.

In conclusion, we should note that the TM surface waves propagating at the moving plasma boundary also possess some other features typical of noncollinear surface waves [1–6]. These waves demonstrate the relativity of spectral representation depending on the observer position and have a common upper spectrum edge point in the plane ω–K (the bold point in Fig. 1) at which the oscillations become totally delocalized. When the velocity of the supporting boundary increases, the degree of delocalization grows along with the phase velocity, i.e., the spectral characteristics of these oscillations approach those of the volume waves. In addition, the motion of the supporting boundary causes an increase in the specific (calculated per unit area of the boundary) mean energy of the TM surface wave. There are certain differences as well: for example, because of the absence of the partial components similar to near-boundary electric [1–3] or magnetostatic [4, 5] oscillations, fields of the TM surface wave do not exhibit Doppler frequency shifts; as a result, no beats in the oscillation fields can be observed.

Acknowledgments. This work was supported by the “Integration” Special Federal Program, code A 0066.

REFERENCES

1. N. S. Shevyakhov, Akust. Zh. **45** (4), 570 (1999) [Acoust. Phys. **45**, 509 (1999)].
2. Yu. V. Gulyaev, O. Yu. El’meshkin, and N. S. Shevyakhov, Radiotekh. Élektron. (Moscow) **45** (3), 351 (2000).
3. O. Yu. El’meshkin and N. S. Shevyakhov, Zh. Tekh. Fiz. **71** (5), 35 (2001) [Tech. Phys. **46**, 540 (2001)].
4. E. A. Vilkov, V. G. Shavrov, and N. S. Shevyakhov, Pis’ma Zh. Tekh. Fiz. **27** (17), 40 (2001) [Tech. Phys. Lett. **27**, 728 (2001)].
5. E. A. Vilkov, V. G. Shavrov, and N. S. Shevyakhov, Izv. Vyssh. Uchebn. Zaved., Radiofiz. **44** (8), 712 (2001).
6. Yu. V. Gulyaev and N. S. Shevyakhov, Akust. Zh. **47** (5), 637 (2001) [Acoust. Phys. **47**, 552 (2001)].
7. L. I. Mandel’shtam, *Lectures on the Theory of Oscillations* (Nauka, Moscow, 1972).
8. A. N. Kondratenko, *Surface and Volume Waves in Bounded Plasma* (Énergoatomizdat, Moscow, 1985).
9. V. V. Zheleznyakov, *Electromagnetic Waves in Cosmic Plasma* (Nauka, Moscow, 1977).

Translated by A. Kondrat’ev

Technical Physics Letters, Vol. 28, No. 6, 2002, pp. 510–514. Translated from Pis'ma v Zhurnal Tekhnicheskoĭ Fiziki, Vol. 28, No. 12, 2002, pp. 48–56.
Original Russian Text Copyright © 2002 by Avetisyan.

On the Stability of Synchronization of Counterpropagating Superfluorescence Pulses

Yu. A. Avetisyan
Institute for Problems in High-Precision Mechanics and Control, Russian Academy of Sciences, Saratov, Russia
e-mail: AvetisyanYuA@info.sgu.ru

Received October 22, 2001

Abstract—Correlation of the parameters (delay times, peak intensities) of counterpropagating superfluorescence pulses is studied within the framework of a one-dimensional theoretical model depending on the sharpness of boundaries of the excitation region. The concentration N_0 of the initially excited active centers is described by a smoothed profile (decaying to zero within the h_- and h_+ wide intervals at the left- and right-hand ends of the sample, respectively), rather than by a rectangular profile. It is established that variation of the excitation region boundary widths $h_\pm$ does not eliminate the observed correlations. Moreover, the correlations can significantly increase for the samples with a length of $L = n\lambda/2$, where n is any natural number and λ is the resonance light wavelength. The oscillating dependence of the parameters of counterpropagating superfluorescence pulses on the $h_\pm$ values and a significant asymmetry of these pulses for $h_- \neq h_+$ are discussed. *© 2002 MAIK "Nauka/Interperiodica".*

A thorough investigation of the mechanisms involved in reflected radiation field formation is important for better understanding and application of some phenomena known in coherent and nonlinear optics. One of such phenomena is the superfluorescence (SF) effect representing two light pulses emitted in the opposite directions from an extended inverted region (sample) possessing an elongated shape. The counterpropagating SF pulses exhibit correlation (experimentally observed, e.g., in [1, 2]) explained by a resonance reflection of the light field from the sample boundaries, where the inversion varies in a jumplike manner [3–7]. Previous investigations based on this concept [8–11] revealed a strong dependence of the coefficient of correlation between the delay times of counterpropagating SF pulses on the sample length L, being a multiple of the resonance radiation wavelength $\lambda/2$: the correlation was maximum for L equal to an odd number of $\lambda/4$ and was virtually absent for L proportional to $\lambda/2$.

A close problem [7, 12–18] is related to the phenomenon of induced SF initiated by an external pulse with an intensity exceeding the level of quantum noise in the system [19]. It was demonstrated [13–18] that a pulse of sufficiently small area can predominantly induce emission either in the forward or in the backward direction relative to that of the initiating pulse propagation. This is valid for a sample length close to $L = n\lambda/2$, while even small deviations from this relation lead to nearly complete symmetry of the counterpropagating SF pulses.

In this context, it was of interest to study the role of sharpness of the boundary of the excitation region on the degree of synchronization of the counterpropagating SF pulses.

The SF from an ensemble of two-level active centers (atoms) was described using a system of one-dimensional semiclassical equations for the locally averaged Bloch vector components $Z(x, \tau)$ and $R(x, \tau)$ of an atomic system,

$$\frac{\partial Z}{\partial \tau} = -\frac{1}{2}ER^* + \text{c.c.}, \quad \frac{\partial R}{\partial \tau} = EZ, \tag{1}$$

and the integral form of the wave equation for a dimensionless complex electric field amplitude,

$$E(x, \tau) = L^{-1}\int_{-L/2}^{L/2} dy \exp(-ik|x-y|)R\left(y, \tau - \frac{|x-y|}{ct_c}\right), \tag{2}$$

where $\tau = t/t_c$ is the current time normalized to a characteristic time scale of the pulse $t_c = \hbar c/(2\pi\omega_{12}d_{12}^2\bar{N}_0 L)$; $\hbar$ and c are the Planck constant and the speed of light, respectively; ω_{12} and d_{12} are the frequency and dipole moment of the optical transition between the working levels $|1\rangle$ and $|2\rangle$; $\bar{N}_0 = N/(S_\perp L)$ is the average concentration of initially excited atoms; N is the total number of atoms; $S_\perp$ is the sample cross section; $k = \omega_{12}/c = 2\pi/\lambda$ is the wave number; and λ is the resonance light wavelength. The Bloch vector components are expressed as

$$Z(x, \tau) = \frac{1}{\bar{N}_0 \Delta V(x)} \sum_{j \in \Delta V(x)} [\rho_{22}^{(j)}(\tau) - \rho_{11}^{(j)}(\tau)],$$
$$R(x, \tau) = \frac{2\exp(-i\omega_{12}t)}{N_0 \Delta V(x)} \sum_{j \in \Delta V(x)} \rho_{12}^{(j)}(\tau), \qquad (3)$$

where $\rho_{mn}^{(j)}(\tau)$ are elements of the density matrix of the jth atom at the time τ; $\Delta V(x) = \Delta x S_\perp$ is the macroscopic averaging volume centered at the point x; and $\varepsilon(x, t) = h/(i2d_{12}t_c)\exp(i\omega_{12}t)E(x, \tau)$ + c.c. is the electric field.

Note that Eqs. (1) and (2) correspond to the rotating wave approximation, whereby the amplitudes $E(x, \tau)$, $R(x, \tau)$, and the inversion $Z(x, \tau)$ are considered as slowly varying over the period of field oscillation $2\pi/\omega_{12}$. The concept of splitting of the polarization and field into waves with smoothly varying amplitudes [20–22] propagating in opposite directions (along the sample) is not employed. The proposed approach allows the resonance reflection of the field from the sample ends [4] to be adequately described without recourse to phenomenological reflection coefficients [20–22].

Using the method of Haake *et al.* [23] generalized to the case of variable N_0, we obtain the following initial conditions for the dynamic quantities involved in the semiclassical approach:

$$E(x, 0) = 0, \quad Z(x, 0) = C(x),$$
$$\langle R^*(x_1, 0)R^*(x_2, 0)\ldots R^*(x_n, 0)R(y_1, 0)R(y_2, 0)\ldots R(y_n, 0)\rangle$$
$$= \left[\frac{4L}{N}\right]^n \sum_{\{y_1, y_2 \ldots y_n\}} C(x_1)\delta(x_1 - y_1)C(x_2) \qquad (4)$$
$$\times \delta(x_2 - y_2)\ldots C(x_n)\delta(x_n - y_n),$$
$$n = 1, 2, \ldots,$$

which correspond to the deterministic character of the electric field and inversion and to stochastic polarization. The angle brackets denote averaging over to the ensemble of realizations of the initial polarization; the sum contains $n!$ permutations of the coordinates $\{y_1, y_2 \ldots y_n\}$ [23]; $C(x) = N_0(x)/\bar{N}_0$; and $\delta(\xi)$ is the Dirac delta. For a homogeneous initial inversion, $C(x) \equiv 1$ and Eqs. (4) coincide with the corresponding expressions in [23].

Below we describe the results obtained using the simplest way of varying the sharpness of boundaries of the excitation region. According to this, $N_0(x)$ was taken constant in the central part of the sample and it linearly decayed to zero within the "smoothing" intervals h_- and h_+ at the left- and right-hand ends of the sample, respectively. In other words, the profile $C(x)$ of the initial inversion density possessed a trapezoidal shape.

Based on the numerical solution of Eqs. (1) and (2) with the initial condition (4) in the approximation of $L/(ct_c) \ll 1$ (valid for not too long samples [20]), we have calculated an ensemble of the SF pulse realizations and determined the correlation coefficients for the normalized delay times $\tau_\pm$ and the peak intensities $I_\pm = |E(\pm L/2, \tau_\pm)|^2/2$ of the right-hand (+) and left-hand (–) pulses,

$$K_\tau \equiv K(\tau_+, \tau_-) \qquad (5)$$
$$= \langle(\tau - \langle\tau_+\rangle)(\tau - \langle\tau_-\rangle)\rangle / [\langle(\tau - \langle\tau_+\rangle)^2\rangle\langle(\tau - \langle\tau_-\rangle)^2\rangle]^{1/2},$$

and the analogous correlation coefficients for the intensities, $K_I \equiv K(I_+, I_-)$.

The results presented in Fig. 1 for a symmetric initial inversion profile $C(x)$ show that the delay times (and peak intensities) of the counterpropagating SF pulses exhibit correlation (anticorrelation) possessing an oscillating character depending on the length of the "smoothing" intervals $h_- = h_+$. The minima of correlation and anticorrelation are observed at $h_\pm = m\lambda/2$ (Fig. 1a, $L = 22\lambda$, m being an integer) and at $h_\pm = n\lambda/4$ (Fig. 1b, $L = 21.75\lambda$, n being a natural number), respectively. It is obviously important to take this circumstance into account in the experiment, since the results of observations for the synchronism of the counterpropagating SF pulses may be significantly dissimilar for the intervals $h_\pm$ differing (under otherwise equal conditions) by $\lambda/4$ in the former case (Fig. 1a) and by $\lambda/8$ in the second case (Fig. 1b).

The observed characteristic features in behavior of the numerically determined correlation coefficients (the positions of extrema, doubling of the modulation frequency, and more rapid decrease in this frequency for a sample with $L = 21.75\lambda$ as compared to that with $L = 22\lambda$) are explained by the enhancing or compensating effect of the interference of secondary waves. This interference can be characterized (as it was done in [9] for the case of $h_\pm = 0$) by the correlation coefficient K_0 for intensities I_+, I_- at the beginning of the process:

$$K_0 = |J|^2,$$
$$J = \frac{1}{DU^2}\left\{\frac{\exp[U(h_-/L - 1/2)] - \exp[-U/2]}{h_-/L}\right. \qquad (6)$$
$$\left. + \frac{\exp[U(1/2 - h_+/L)] - \exp[U/2]}{h_+/L}\right\},$$

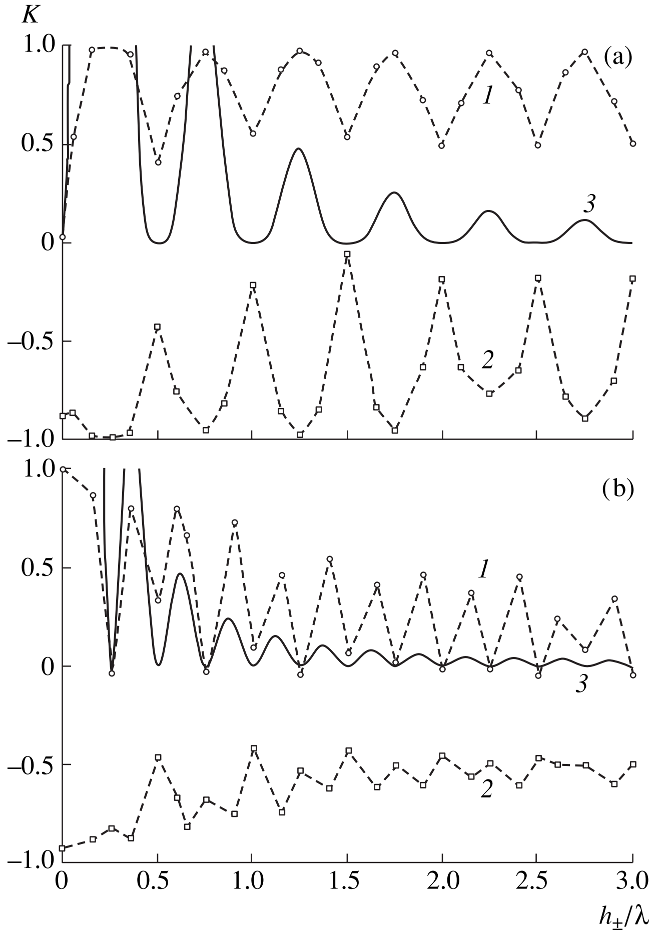

Fig. 1. Dependence of the correlation between the counterpropagating SF pulses on the width $h_- = h_+$ of the "smoothing" intervals in the initial inversion density profile for samples with the total number of initially excited atoms $N = 10^{20}$ and the lengths $L = 22\lambda$ (a) and 21.75λ (b): (*1*) correlation coefficients of delay times $K(\tau_+, \tau_-)$; (*2*) correlation coefficients of peak intensities $K(I_+, I_-)$; (*3*) scaled intensity correlation coefficients AK_0 at the beginning of the process calculated by formula (6) for $A = 5 \times 10^5$.

where $D \equiv 1 - 0.5(h_-/L) - 0.5(h_+/L)$ and $U = i2kL$ (Figs. 1 and 2). This expression was derived using two- and four-point correlators ($n = 1, 2$) in Eq. (4). Note that the "smoothing" for $L = 22\lambda$ increases the correlation of delay times K_τ (compared to the case of $h_{\pm = 0}$), which is significant ($K_\tau \approx 0.5$) even for $h_- = h_+ = L/2 = 11\lambda$.

The results presented in Fig. 2 for a nonsymmetric profile $C(x)$ indicate that a change in the "smoothing" interval at the left-hand end of the sample ($h_- \neq 0$, $h_+ \equiv 0$) leads to asymmetry and oscillations in parameters of the counterpropagating SF pulses. The right-hand pulse possesses, on the average, a greater delay time and a smaller peak intensity (Figs. 2a and 2b). The average time delays (and peak intensities) are maximum (minimum) for $h_- = n\lambda/2$ (Figs. 2a and 2b). Dependence of the correlation coefficients on h_- (Fig. 2c) is qualitatively the same as in Fig. 1a and remains just as significant for the experimental results.

The calculations showed that the influence of the initial inversion density profile upon synchronization of the counterpropagating SF pulses is insignificant for small N and becomes important when N exceeds a certain threshold value of $\tilde{N}$ (this is reflected by Fig. 2d, where we can take $\tilde{N} \sim 10^8$). This behavior can be explained as follows. At a small N, reflection of the field from the sample ends (more precisely, from the boundary intervals of length $h_\pm$ near the corresponding ends) are almost insignificant. For the initial stage of the process ($Z(x, \tau) \approx Z(x, 0) \equiv C(x)$), we obtain a solution

$$I_\pm(\tau) = \frac{|E_\pm(\tau)|^2}{2}, \qquad (7)$$

$$E_\pm(\tau) = L^{-1}\int_{-L/2}^{L/2} dy R_\pm(y, 0) I_0\left\{2\left[\pm\frac{\tau}{L}\int_{y}^{\pm L/2} dx C(x)\right]^{1/2}\right\},$$

which proves to be relatively weakly dependent on the shape of the $C(x)$ profile (the initial polarization is represented as $R(y, \tau) = R_+(y, \tau)\exp(-iky) + R_-(y, \tau)\exp(iky)$ in the approximation of slowly varying amplitudes; $I_0\{\xi\}$ is the modified zero-order Bessel function of ξ). Should N exceed the threshold $\tilde{N}$ (roughly estimated as $N \sim (kL)^4$ for $h_\pm = 0$, see [10, 11]), the system features a multipath field amplification regime in which the reflections become important. In this case, the process dynamics is determined to a considerable extent by interference of the secondary waves and significantly depends (as considered above) on the intervals $h_\pm$.

The asymmetry of the counterpropagating SF pulses can be explained as follows. As the h_- value increases, the efficacy of the field reflection from the left-hand end of the sample drops, while that from the right-hand end (where $r_{\mathrm{eff}} \sim (kL)^{-1}$, see [10,11]) remains unchanged. As a result, the intensity of emission for $N > \tilde{N}$ and $h \gg \lambda$ is determined by the field amplification in the single-path regime at the right-hand end and in the double-path regime at the left-hand end [10, 11]. This difference accounts for the accelerated development of the left-hand SF pulse.

In concluding, it should be noted that the results of calculations confirmed a significant effect of the spatial inhomogeneity in the initial inversion on the induced SF regime. This phenomenon offers additional possibilities for controlling the parameters of SF pulses. In particular, for initiating pulses of small area, it is possible to modify the $C(x)$ profile so as to obtain significantly asymmetric counterpropagating SF pulses in a sample of length $L = (2n + 1)\lambda/4$.

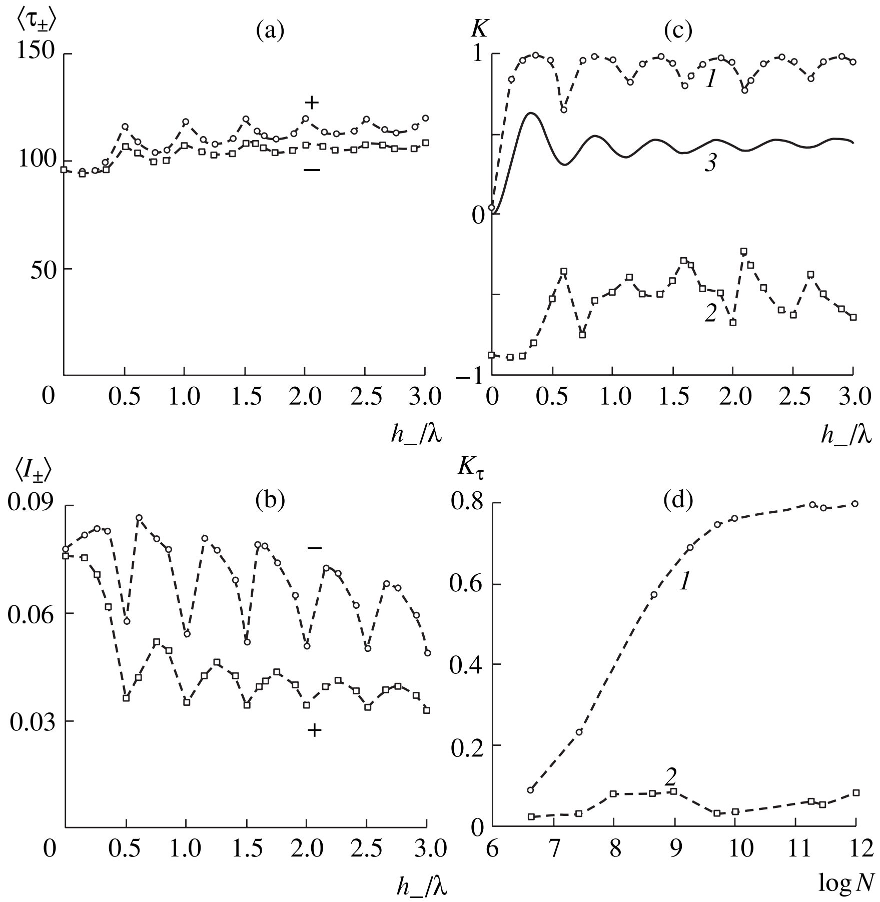

Fig. 2. Effect of the width of the left-hand "smoothing" interval h_- (for $h_+ = 0$) on the (a) average delay time $\langle\tau_\pm\rangle$, (b) peak intensities $\langle I_\pm\rangle$, and (c) correlation coefficients of counterpropagating SF pulses (notation and parameters are the same as in Fig. 1, except for the scaling factor $A = 3 \times 10^4$); (d) plot of the delay time correlation coefficient K_τ versus the total number of initially excited atoms N for $h_- = 2.25\lambda$ (*1*) and 0 (*2*).

Thus, it was demonstrated that the degree of autosynchronization of the counterpropagating SF pulses can be significant for a high density of the initial inversion with "smoothed" boundaries of the excitation region. The nontrivial dependence of the parameters of counterpropagating SF pulses on the sample length, as well as on the magnitude and distribution of the initial inversion density, should be taken into account during the experimental investigations of both the SF proper and the induced SF phenomena.

Acknowledgments. This study was supported by the "Leading Scientific Schools" Program of the Russian Foundation for Basic Research, project no. 00-15-96667.

REFERENCES

1. R. Florian, L. O. Schwan, and D. Schmid, Phys. Rev. A **29**, 2709 (1984).
2. S. N. Andrianov, P. V. Zinov'ev, Yu. V. Malyukin, *et al.*, Zh. Éksp. Teor. Fiz. **91** (6), 1990 (1986) [Sov. Phys. JETP **64**, 1180 (1986)].
3. M. Lewenstein and K. Rzazewski, Phys. Rev. A **26** (3), 1510 (1982).
4. M. G. Benedict and E. D. Trifonov, Phys. Rev. A **38**, 2854 (1988).
5. V. A. Malyshev, E. D. Trifonov, and L. O. Shvan, Opt. Spektrosk. **76** (3), 524 (1994) [Opt. Spectrosc. **76**, 470 (1994)].
6. E. D. Trifonov, Opt. Spektrosk. **77** (1), 61 (1994) [Opt. Spectrosc. **77**, 51 (1994)].
7. I. V. Mel'nikov, Phys. Rev. Lett. **77**, 842 (1996).
8. Yu. A. Avetisyan and E. D. Trifonov, Opt. Spektrosk. **82** (3), 357 (1997) [Opt. Spectrosc. **82**, 323 (1997)].
9. Yu. A. Avetisyan and E. D. Trifonov, Proc. SPIE **2778**, 727 (1996).
10. Yu. A. Avetisyan, Pis'ma Zh. Tekh. Fiz. **25** (19), 24 (1999) [Tech. Phys. Lett. **25**, 769 (1999)].
11. Yu. A. Avetisyan, Proc. SPIE **3609**, 245 (1999).
12. J. T. Manassah and B. Gross, Opt. Commun. **148**, 404 (1998).
13. J. T. Manassah and B. Gross, Opt. Commun. **150**, 189 (1998).

14. A. I. Zaĭtsev, D. A. Mosunov, and E. D. Trifonov, Opt. Spektrosk. **88** (5), 821 (2000) [Opt. Spectrosc. **88**, 743 (2000)].
15. A. A. Bogdanov and A. I. Zaĭtsev, Opt. Spektrosk. **90** (2), 315 (2001) [Opt. Spectrosc. **90**, 269 (2001)].
16. A. A. Bogdanov and A. I. Zaĭtsev, Opt. Spektrosk. **90** (5), 796 (2001) [Opt. Spectrosc. **90**, 715 (2001)].
17. A. A. Bogdanov and A. I. Zaĭtsev, Opt. Spektrosk. **90** (5), 806 (2001) [Opt. Spectrosc. **90**, 725 (2001)].
18. A. A. Bogdanov and A. I. Zaĭtsev, Opt. Spektrosk. **90** (6), 935 (2001) [Opt. Spectrosc. **90**, 842 (2001)].
19. R. F. Malikov and E. D. Trifonov, Opt. Commun. **52**, 74 (1984).
20. V. V. Zheleznyakov, V. V. Kocharovskiĭ, and Vl. V. Kocharovskiĭ, Usp. Fiz. Nauk **159** (2), 193 (1989) [Sov. Phys. Usp. **32**, 835 (1989)].
21. F. Haake, M. I. Kolobov, and H. Steudel, Opt. Commun. **92**, 385 (1992).
22. E. N. Kaneva and E. D. Trifonov, Opt. Spektrosk. **79** (2), 293 (1995) [Opt. Spectrosc. **79**, 270 (1995)].
23. F. Haake, H. King, G. Schroder, *et al.*, Phys. Rev. A **20**, 2047 (1979).

Translated by P. Pozdeev

Technical Physics Letters, Vol. 28, No. 6, 2002, pp. 515–516. Translated from Pis'ma v Zhurnal Tekhnicheskoĭ Fiziki, Vol. 28, No. 12, 2002, pp. 57–61.
Original Russian Text Copyright © 2002 by Kanchukoev, Kashezhev, Mambetov, Sozaev.

The Effect of an Electric Field on the Surface Energy and Electron Work Function of Thin Films of Alkali Metal Alloys

V. Z. Kanchukoev, A. Z. Kashezhev, A. Kh. Mambetov, and V. A. Sozaev*
Kabardino-Balkarian State University, Nal'chik, Kabardino-Balkaria, Russia
** e-mail: sozaevv@kbsu.ru*

Received January 9, 2002

Abstract—The surface energy and the electron work function are calculated for thin films of alkali metal alloys within the framework of the electron gas model using the electron distribution function at the film–vacuum interface. *© 2002 MAIK "Nauka/Interperiodica".*

The results of investigations of the surface properties of thin films of metal alloys [1–6] show evidence for the presence of the size effects in the surface composition, surface energy, and electron work function of the films. It was of interest to study the influence of an external electric field on the manifestations of these size effects in the surface properties of thin films of metal alloys. To our knowledge, such data were never reported in the literature.

Let us consider the film of a binary substitution alloy of the A_xB_{1-x} type with a thickness L, within the framework of the virtual crystal method [7]. According to this model, the surface segregation at the alloy–vacuum interface leads to the formation of a modified surface layer of thickness D with a positive charge density $n_s = [x_s\Omega_A + (1-x_s)\Omega_B]^{-1}$ (Fig. 1), where x_s is the surface concentration of the alloy component A; Ω_A and Ω_B are the Wigner–Seitz cell volumes of the alloy components A and B, respectively. Denoting a positive charge density inside the film by n_0, we can describe the electron density distribution at the interface by the function

$$n_-(z) = \begin{cases} n_0(1-\exp(-\beta Z_G)\cosh(\beta z)), & z < Z_G, \\ n_0\sinh(\beta Z_G)\exp(-\beta z), & z > Z_G, \end{cases} \tag{1}$$

where β is the variation parameters determined from the condition of minimum surface energy $\sigma = \min\limits_{\beta,\, n_s}\sigma(\beta, n_s)$; z is the coordinate along the normal to the sample surface, measured from the middle of the film; and Z_G is the coordinate of the Gibbs interface determined from the condition of electroneutrality of the system:

$$\int_0^\infty [n_-(z) + n_+(z)]dz = E/4\pi n_0 \tag{2}$$

$$Z_G = L/2 - (1 - n_s/n_0)D \pm E/4\pi n_0. \tag{3}$$

The electrostatic potential $\varphi(z)$ on the alloy–vacuum interface is determined from the Poisson equation, which can be written as

$$d^2\varphi/dz^2 = \begin{cases} -4\pi[n(z)-n_0], & 0 < z < L/2 - D, \\ -4\pi[n(z)-n_s], & L/2 - D < z < Z_G, \\ -4\pi[n(z)-n_s], & Z_G < z < L/2, \\ -4\pi n(z), & z > L/2 \end{cases} \tag{4}$$

for $Z_G < L/2$, and as

$$d^2\varphi/dz^2 = \begin{cases} -4\pi[n(z)-n_0], & 0 < z < L/2 - D, \\ -4\pi[n(z)-n_s], & L/2 - D < z < L/2, \\ -4\pi n(z), & L/2 < z < Z_G, \\ -4\pi n(z), & z > Z_G \end{cases} \tag{5}$$

for $Z_G > L/2$. The Poisson equations (3) and (4) have to be solved with the boundary conditions for φ and φ' at the film–vacuum interface.

The total surface energy of the film can be calculated in the homogeneous background approximation by the formula

$$\sigma_j = 2\int_0^\infty \{w[n_-(z)] - w[n_+(z)]\}dz + \int_0^\infty \varphi(z)[n_-(z) - n_+(z)]dz, \tag{6}$$

where $w[n(z)]$ is the kinetic energy density of a noninteracting gas (with a correction for the field inhomoge-

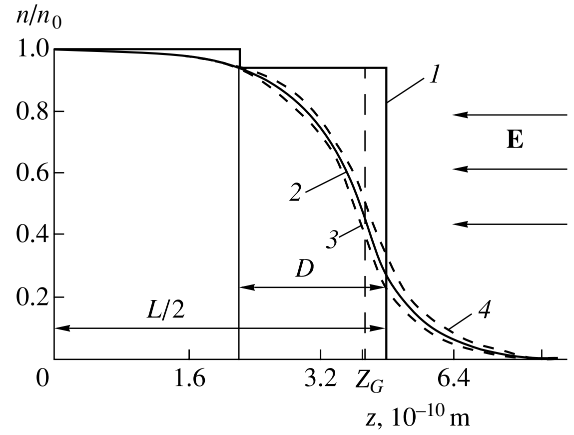

Fig. 1. The distributions of (*1*) ion and (*2*–*4*) electron charges at the film–vacuum interface for the $Na_{0.5}K_{0.5}$ alloy film with a thickness of $L = 7.935 \times 10^{-10}$ m in an external field with the strength $E = 0$ (*2*), 2.6×10^7 (*3*), and -2.6×10^7 V/cm (*4*).

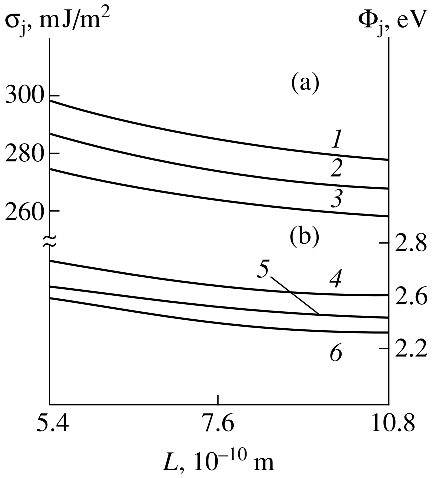

Fig. 2. Plots of (a) the surface energy σ_j calculated by formula (6) and (b) electron work function Φ_j calculated by formula (7) versus the $Na_{0.5}K_{0.5}$ alloy film thickness for the field strength $E = -2.6 \times 10^7$ (*1*, *6*), 0 (*2*, *5*), 2.6×10^7 V/cm (*3*, *4*).

neity) and the exchange–correlation interaction energy (with a nonlocal correction).

The electron work function is calculated by a formula derived using the sum rule

$$\begin{aligned}\Phi_j &= -\varphi(L/2-D)-(n_s/n_0)\\ &\times[\varphi(L/2)-\varphi(L/2-D)]+E/(8\pi n_0)-\epsilon(n_0),\end{aligned} \qquad (7)$$

where $\epsilon(n_0)$ is the density of the kinetic, exchange, and correlation energies; $\varphi(L/2 - D)$ and $\varphi(L/2)$ are the electrostatic potential $\varphi(z)$ on the boundary planes $z = L/2 - D$ and $z = L/2$.

Figure 2 presents the results of calculations using formulas (6) and (7). The data in Fig. 2a show that the surface energy of the film decreases with increasing film thickness both in the presence and in the absence of an external field. A field directed toward the film ($E > 0$) decreases the surface energy since the fraction of the electron distribution outside the film grows; for $E < 0$, the surface energy of the film increases.

Figure 2b shows the electron work function of a film of the $Na_{0.5}K_{0.5}$ alloy. As can be seen from this figure, the size dependence of the work function is the same in the presence and in the absence of the film. The electron work function increases for $E > 0$ and decreases for $E < 0$, which is explained by the interplay of two factors. On the one hand, the field with $E > 0$ favors a decrease in the work function; on the other hand, this field reduces the surface segregation of potassium, which is the alloy component possessing a lower work function. It is the latter factor that produces a net increase in the work function for $E > 0$ and a decrease for $E < 0$ [7].

REFERENCES

1. J. L. Moran-Lopez, G. Kerker, and K. H. Benneman, Surf. Sci. **66** (2), 641 (1977).
2. A. M. Llois and C. R. Mirasso, Phys. Rev. B **41** (12), 8112 (1990).
3. H. Bogdanov and K. F. Wojciechovski, J. Phys. D **29**, 1310 (1996).
4. V. A. Sozaev, V. V. Chernov, R. A. Chernyshova, and D. V. Yaganov, Vestn. Kabard.-Balkar. Gos. Univ., Ser. Fiz. Nauki, No. 4, 20 (2000).
5. S. Swaminarayan and D. Srolovitz, Acta Metall. Mater. **44**, 2067 (1996).
6. R. M. Digilov and V. A. Sozaev, Poverkhnost, No. 10, 138 (1990).
7. V. Z. Kanchukoev, A. Z. Kashezhev, A. Kh. Mambetov, and V. A. Sozaev, Pis'ma Zh. Tekh. Fiz. **27** (20), 89 (2001) [Tech. Phys. Lett. **27**, 886 (2001)].

Translated by P. Pozdeev

Technical Physics Letters, Vol. 28, No. 6, 2002, pp. 517–520. Translated from Pis'ma v Zhurnal Tekhnicheskoĭ Fiziki, Vol. 28, No. 12, 2002, pp. 62–71.
Original Russian Text Copyright © 2002 by Odnoblyudov, Kovsh, Zhukov, Egorov, Maleev, Mikhrin, Ustinov.

Molecular Beam Epitaxy of (Al)GaAsN Using Ammonia as a Source of Nitrogen

V. A. Odnoblyudov, A. R. Kovsh, A. E. Zhukov, A. Yu. Egorov, N. A. Maleev, S. S. Mikhrin, and V. M. Ustinov

Ioffe Physicotechnical Institute, Russian Academy of Sciences, St. Petersburg, 194021 Russia

Received December 6, 2001

Abstract—The possibility of using ammonia as a source of nitrogen for the molecular beam epitaxy (MBE) of AlGaAsN/GaAs layers was studied. It is shown that nitrogen is not incorporated into the GaAs layers in a broad range of the MBE conditions studied. The incorporation of nitrogen is possible in the presence of aluminum in the growing film. The molar fraction of nitrogen in the growing material is equal to that of aluminum, provided that the supply rate of ammonium is sufficiently high. Theoretical estimates are confirmed by the experimental data. *© 2002 MAIK “Nauka/Interperiodica”.*

Introduction. One of the currently important problems in the technology of $A^{III}B^{V}$ semiconductor compounds is to develop GaAs-based device structures capable of emitting in the 1.3-μm wavelength range. Recent progress in providing for highly effective radiative recombination and high material gain in such structures shows good prospects for creating vertical-cavity surface-emitting lasers meeting all requirements to radiation sources for local fiber optic communication lines.

One of the promising ways to solve the above problem is the use of heterostructures with InGaAsN quantum wells [1], which is related to an anomalously sharp decrease in the bandgap of (In)GaAs upon introducing a few percent of nitrogen into this composition. To the present, the best characteristics of surface-emitting lasers with both strip and vertical-cavity geometry employing InGaAsN quantum wells were obtained in heterostructures grown by the method of molecular beam epitaxy (MBE) [2, 3].

Traditional sources of nitrogen for MBE growth are offered by plasmas of various types generated in RF discharge, electron cyclotron resonance, and dc plasma sources. Researchers studying the MBE process with these sources frequently pointed out a drop in the photoluminescence intensity observed upon the incorporation of nitrogen into (In)GaAs layers [4–6], which leads to inferior characteristics of such structures as compared to those of lasers with InGaAs quantum wells. One of the main reasons for this fact is the presence of high-energy nitrogen ions bombarding the surface of the growing film, which results in the appearance of nonradiative recombination centers. Using nitrogen-containing gaseous compounds which decompose immediately on the surface can solve this problem since the presence of high-energy particles is eliminated. However, the MBE growth at relatively low temperatures may give rise to problems related to the degree of decomposition of the nitrogen-containing compounds employed.

Therefore, it is important to study the alternative sources of nitrogen for the MBE process. For example, Maclean *et al.* [7] suggested employing 1,1-dimethylhydrazine. Below we report on the results of investigation of the possibility of using ammonia as a source of nitrogen during MBE growth of nitrogen-containing layers on gallium arsenide substrates.

Nitrogen incorporation into Ga(Al)As layers. The greater the amount of energy liberated in the course of a reaction, the more readily and faster the reaction proceeds. In order to elucidate the possibility of incorporating nitrogen into GaAs layers, we have calculated the temperature variation of the Gibbs free energy $\Delta G(T)$ as a result of the formation of GaAs and GaN compounds via reactions

$$\mathrm{Ga} + 1/4\mathrm{As}_4 \Rightarrow \mathrm{GaAs}, \tag{1}$$

$$\mathrm{Ga} + \mathrm{NH}_3 \Rightarrow \mathrm{GaN} + 3/2\mathrm{H}_2. \tag{2}$$

For reaction (1), the $\Delta G(T)$ values were calculated using the temperature dependence of the equilibrium constant K reported in [8]:

$$K = \exp\left(\frac{\Delta G}{RT}\right). \tag{3}$$

For reaction (2), the calculation was performed using the data taken from [9]. The results of these calculations are presented in Fig. 1. As can be seen, the $\Delta G(T)$ plots for the formation of GaN occur above those for GaAs in the whole interval of temperatures typical of the MBE process, which indicates that it is energetically more favorable for gallium to react with arsenic than with nitrogen. Thus, the growth of GaAsN layers with nitrogen supplied from ammonia decomposed on the

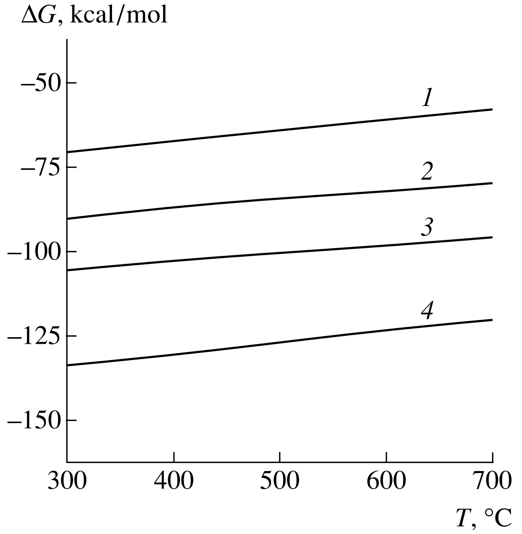

Fig. 1. Plots of the Gibbs free energy versus temperature for the formation of (*1*) GaN (NH_3), (*2*) GaAs, (*3*) AlAs, and (*4*) AlN (NH_3).

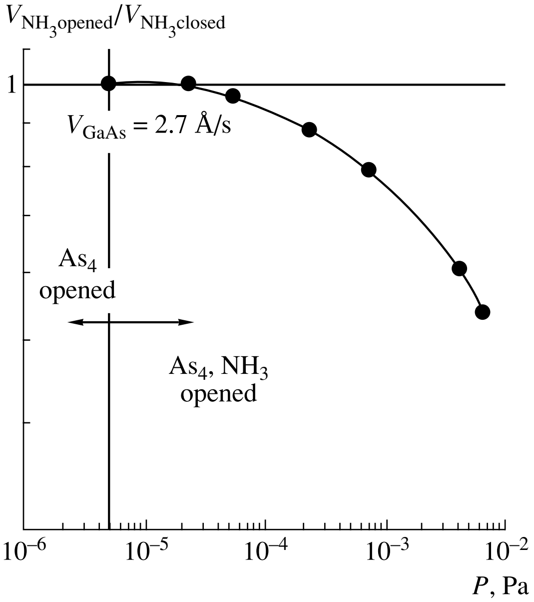

Fig. 2. A plot of the relative growth rate of GaAs versus pressure in the growth chamber (related to the NH_3 flow rate).

surface of the growing material must be complicated as a result of basic limitations concerning interaction between the components under consideration.

One possible way to bypass the basic problem related to the incorporation of nitrogen into GaAs layers consists in introducing aluminum into the growing layer. The $\Delta G(T)$ curve for the formation of AlN via the reaction

$$Al + NH_3 \Rightarrow AlN + 3/2H_2 \qquad (4)$$

calculated using the data from [9] is also presented in Fig. 1. In the temperature interval of interest, the curve of $\Delta G(T)$ for AlN is below the plots corresponding to GaAs and GaN, as well as below the curve for AlAs calculated using relationship (3) and the data from [10]. Therefore, the formation of AlN under these conditions is energetically the most favorable and, hence, aluminum can be used to ensure the incorporation of nitrogen into (Al)GaAs layers.

As noted above, the increased interest in growing GaAsN layers is mostly related to the possibility of providing for a significant longwave shift of the luminescence peak as compared to that in pure GaAs. The layers of GaAs (essentially, AlGaAsN) containing nitrogen incorporated with the aid of aluminum acting as the activator may probably also shift the luminescence peak toward longer wavelengths relative to the GaAs emission. Indeed, a 1% additive of aluminum in GaAs produces a shortwave shift by ~13 meV, while 1% of nitrogen gives a longwave shift of about 170–200 meV.

Thus, the results of calculations show that the incorporation of nitrogen from ammonia into GaAs presents a technically difficult task. However, adding aluminum to the growing layer may facilitate the incorporation of nitrogen into the modified AlGaAs matrix. These theoretical estimates were experimentally confirmed.

Experimental. The samples were grown in an MBE system of the EP-1203 type equipped with solid-state sources of Group III (Al, Ga, In) and Group V (As_4) elements. Nitrogen in the form of ammonium was supplied from a Riber gas inlet system (RGS Model 608 350 82X) connected to the growth chamber by a metal pipe. Gaseous ammonia was purified with a Millipore filter and admitted via a Mass Flow Controller system with a maximum gas flow rate of up to 200 standard cubic centimeter per minute (st cm^3/min).

The substrate temperature T during the growth of Ga(Al)AsN layers could be varied from 400 to 700°C. The growth rate was about $V = 1$ monolayer per second (ML/s). The partial pressure of arsenic in the growth chamber was $P \sim 5 \times 10^{-6}$ Pa. The flow rate F of ammonium could be varied from 0.2 to 200 st cm^3/min. The epitaxial film thicknesses ranged within 0.5–1 μm.

MBE of GaAsN layers. In most cases, the GaAsN layers were grown by simultaneously supplying ammonia and arsenic, with the growth conditions (substrate temperature, ammonia flow rate) varied within broad limits indicated above. The content of nitrogen in the grown layers was determined by methods of X-ray diffraction (rocking curves measured at the (004) reflection), Raman scattering, and electron probe microanalysis (EPMA). None of these techniques showed evidence of nitrogen incorporated into GaAs layers. Since the flux of ammonium molecules was sufficiently large, we have studied the effect of the ammonium flow rate on the GaAs growth. As can be seen from the data presented in Fig. 2, increasing the ammonium flow rate above 20 st cm^3/min leads to a significant decrease in the GaAs flow rate. This is not accompanied by NH_3

decomposition on the crystal surface: ammonium only hinders the access of gallium vapor to the substrate, rather than provides for the incorporation of nitrogen into the growing layer.

In order to decrease the competition between arsenic and nitrogen for the chemical binding to gallium, we studied growth under conditions of intermittent arsenic and gallium flows. It was expected that ammonium would more effectively interact with gallium when the supply of arsenic is suspended. However, the pattern of high-energy electron diffraction observed in the absence of arsenic flow was typical of the growth under metal-stabilized conditions (clear 4×2 structure). This was evidence that ammonium does not interact with gallium and nitrogen is not incorporated into the growing layers. These conclusions were confirmed by measuring the content of nitrogen using the aforementioned methods: nitrogen was not detected.

Thus, the growth of GaAsN layers by MBE using ammonium as a source of nitrogen is an extremely difficult problem. Theoretical predictions are confirmed by the experimental data.

MBE of AlGaAsN layers. A series of AlGaAsN layers was grown at $T = 600°C$, a standard pressure of arsenic in the growth chamber, and a variable flow of ammonia (see above). In most cases, the content of aluminum in the AlGaAs layers was about 20%. We have also studied the effect of ammonia on the growth of AlAs.

The content of nitrogen and aluminum in most of the samples was determined by EPMA. It was found that nitrogen is incorporated into the Al(Ga)As layers. Subsequently, these results were confirmed by the data of other methods (secondary ion mass spectrometry, Auger electron spectroscopy, X-ray diffraction). In addition, it was established that an increase in the ammonium supply rate does not lead to a change in the content of aluminum.

Figure 3 shows a plot of the atomic ratio of nitrogen to aluminum versus the flow rate of ammonium. Black circles represent the experimental data for $Al_{0.2}Ga_{0.8}AsN$, bars indicate the error of measurements, and the curve shows the results of interpolation. As can be seen from these data, the N/Al ratio tends to unity when the ammonium flow rate increases above 10 st cm^3/min (the gas phase pressure in the growth chamber exceeds 10^{-4} Pa). Thus, in a sufficiently large flow of ammonia, each atom of aluminum is capable of trapping one atom of nitrogen. The use of this growth regime provides for the effective incorporation of nitrogen from ammonia into the growing layer. The content of nitrogen in the samples determined by EPMA varied within 18–22%.

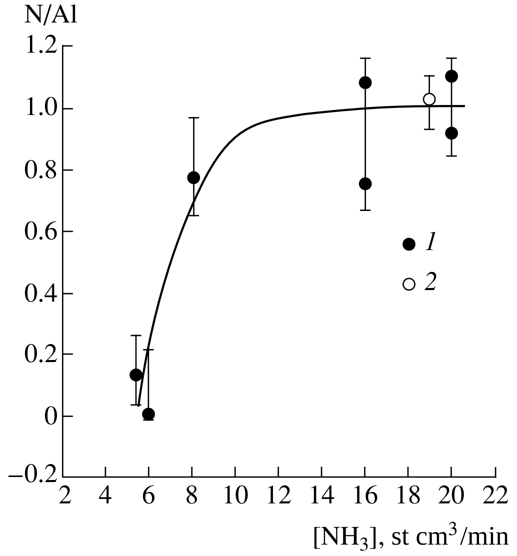

Fig. 3. A plot of the atomic ratio of nitrogen to aluminum versus ammonium flow rate for (*1*) $Al_{0.2}GaAsN$ and (*2*) AlN samples.

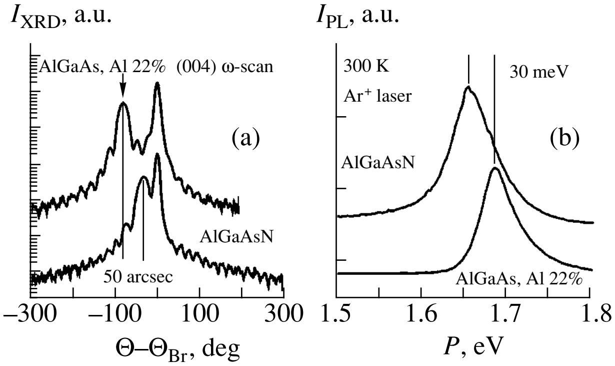

Fig. 4. Comparative data for $Al_{0.22}GaAsN_{0.001}$ and $Al_{0.22}GaAs$: (a) typical X-ray diffraction patterns; (b) photoluminescence spectra.

In order to check whether the results presented in Fig. 3 are characteristic of compounds with other aluminum contents as well, we studied the growth of AlAsN layers. The postgrowth analysis of components in the samples showed an absence of arsenic (point *2* in Fig. 3). Thus, attempts at growing AlAsN lead to the formation of a binary compound with AlN stoichiometry. This result confirms the universal character of the data presented in Fig. 3 and shows agreement between theoretical predictions and the experimental data.

In the case of AlGaAsN layers grown using a large flow of ammonia (>10 st cm^3/min), the growth mechanism changes from two-dimensional (layer growth) to three-dimensional (island growth). Therefore, high-quality epitaxial layers of AlGaAsN can hardly be obtained by MBE with a high flow rate of ammonium (>10 st cm^3/min). The layers of planar morphology were grown using a low ammonium flow rate (below 5 st cm^3/min). Figure 4a shows the typical X-ray diffraction pattern of a sample with the composition $Al_{0.22}GaAsN_{0.001}$. The pattern of thickness oscillations and small width of the diffraction peak are indicative of a high structural perfection of the epitaxial layer. The content of nitrogen was determined by a shift of the X-ray diffraction peak of $Al_{0.22}GaAsN$ relative to that of $Al_{0.22}GaAs$. Figure 4b shows a photoluminescence (PL) spectrum of the same samples. A 30-meV shift of the PL peak of $Al_{0.22}GaAsN$ relative to that of $Al_{0.22}GaAs$ is also indicative of the incorporation of nitrogen into the AlGaAs layer.

We believe that using samples with a low content of aluminum (about 1%) will probably allow one to control the content of incorporated nitrogen on a level of 1%, which is required for the application of a material in the active region of devices emitting in the near IR range. However, growing AlGaAsN compounds with high structural perfection and relatively low aluminum content will require further optimization of the growth regimes. This is related to certain limitations of the accuracy of the composition control in the course of the epitaxial process imposed by technical characteristics of the MBE setup.

Conclusion. We have demonstrated the possibility of incorporating nitrogen into GaAs layers using aluminum as the activator of ammonium decomposition on the surface of the growing layer. Theoretical predictions, according to which GaAlAsN (but not GaAsN) layers can be grown using ammonia as the source of nitrogen, were confirmed by experimental data on the MBE of these compounds. AlGaAsN layers with a high aluminum content (up to 22%), as well as AlN layers, were obtained. It was established that, under certain conditions, the growing layer incorporates one nitrogen atom per aluminum atom. This will probably allow the controlled growth of AlGaAs layers with relatively low (~1%) content of incorporated nitrogen supplied in the form of ammonia. These materials are intended for use in the active regions of lasers emitting in the near IR range.

Acknowledgments. The authors are grateful to V.V. Tret'yakov, V.M. Busov, and D.A. Bedarev for the measurements.

This study was supported by the Federal Program "Physics of Solid State Nanostructures" (project no. 99-2034), the NATO Science for Peace Program (grant no. SfP 972484), and the US Civilian Research and Development Foundation (CRFD grant no. RE1-2221). Special thanks to the Millipore Company (USA) for kindly providing a filter for the purification of ammonia. V.A. Odnoblyudov is grateful to the Leonhard Euler Foundation for support.

REFERENCES

1. M. Kondow, T. Kitatani, S. Nakatsuka, *et al.*, IEEE J. Sel. Top. Quantum Electron. **3**, 719 (1997).
2. B. Borchert, A. Yu. Egorov, S. Illek, *et al.*, Electron. Lett. **35** (25), 2204 (1999).
3. G. Steinle, H. Riechert, and A. Yu. Egorov, Electron. Lett. **37** (2), 93 (2001).
4. T. Kageyama, T. Miyamoto, Sh. Makino, *et al.*, Jpn. J. Appl. Phys. **38**, L298 (1999).
5. D. E. Mars, D. I. Babic, Y. Kaneko, *et al.*, J. Vac. Sci. Technol. B **17** (3), 1272 (1999).
6. A. E. Zhukov, R. Zhao, P. Specht, *et al.*, Semicond. Sci. Technol. **16** (5), 413 (2001).
7. J. O. Maclean, D. J. Wallis, *et al.*, in *Abstract Book of 11th International Conference of Molecular Beam Epitaxy, Beijin, China, 2000*, Tu6.3-1, p. 136.
8. Y. Qiu, S. A. Nikishin, H. Temkin, *et al.*, Appl. Phys. Lett. **70** (21), 2831 (1997).
9. A. Koukitu and H. Seki, Jpn. J. Appl. Phys. **36**, L750 (1997).
10. P. S. Kop'ev and N. N. Ledentsov, Fiz. Tekh. Poluprovodn. (Leningrad) **22**, 1729 (1988) [Sov. Phys. Semicond. **22**, 1093 (1988)].

Translated by P. Pozdeev

Technical Physics Letters, Vol. 28, No. 6, 2002, pp. 521–524. Translated from Pis'ma v Zhurnal Tekhnicheskoĭ Fiziki, Vol. 28, No. 12, 2002, pp. 72–79.
Original Russian Text Copyright © 2002 by L'vov, Svetukhin.

Clusterization in Gases and the Law of Corresponding States

P. E. L'vov* and V. V. Svetukhin
Ul'yanovsk State University, Ul'yanovsk, Russia
** e-mail: pavel@sv.uven.ru*

Received February 5, 2002

Abstract—An equation of state of a real gas, obtained using the principle of minimum Gibbs free energy, agrees with the law of corresponding states. It is shown that this law is valid in systems of particles characterized by equal values of the clusterization energies and the ratios of enthalpy on the surface to that in the bulk. © *2002 MAIK "Nauka/Interperiodica".*

Introduction. The law of corresponding states is a well-known empirical relationship [1,2] indicative of the possibility of writing the equation of state for a gas in terms of the universal dimensionless variables. The necessary condition is that the interactions between gas particles must be described by similar potentials. Based on the dimensionality considerations, Smirnov [3] determined the coefficients (expressed via parameters of the interaction potentials) which allow the state of an inert gas to be described by a single curve on the phase diagram.

Recently [4], we derived an equation of state for a real gas with an allowance for the clusterization process. Using this equation, we described the experimental isotherms of water vapor [4] and some inert gases [5] and determined the parameters of interaction between particles in the clusters. The calculated values showed good agreement with experimental data on the heat of evaporation and with the results of quantum-mechanical calculations.

In this paper, we will consider mutual consistency of the model developed previously and the law of corresponding states and find a criterion for applicability of these relationships to inert gases.

A model of the system of particles with an allowance for the cluster formation. Previously [4], we developed a thermodynamic model describing the process of clusterization in a real gas. Assuming the gas to obey a lattice model and excluding the second phase formation, the Helmholtz free energy can be expressed as follows [4]:

$$F = \sum_{i=1}^{N'} g_i N_i - kT\ln W, \tag{1}$$

where N_1 is the number of monomers, N_i ($i \geq 2$) is the number of clusters composed of i particles, g_1 is the energy of a single particle, g_i ($i \geq 2$) is the energy of a cluster containing i particles, N is the total number of cells in the lattice, N' is the total number of particles in the system, and W is the thermodynamic probability.

Assuming that the number of cells is much greater than the number of particles ($N \gg N'$), one can write the thermodynamic probability as [4]

$$W = \frac{N!}{(N-N')!\prod_i N_i!(i!)^{N_i}}\prod_i\left(\frac{1}{N^{i-1}}\right)^{N_i}. \tag{2}$$

Using the Lagrange method of undetermined multipliers to minimize the Helmholtz free energy (1) with an allowance for the particle number conservation,

$$N' - \sum_{l=1}^{N'} lN_l = 0, \tag{3}$$

we arrive at the following expression for the number of clusters containing an arbitrary number i of particles:

$$N_i = \frac{1}{N^{i-1}i!}\exp\left(-\frac{g(i)-\lambda i}{kT}\right), \quad i > 1, \tag{4}$$

$$N_1 = \exp\left(-\frac{g_1-\lambda}{kT}\right), \tag{5}$$

where λ is the Lagrange factor determined upon solving Eq. (3) related to the particle number conservation condition. Since the initial energy level is arbitrary, the free energy of a single particle g_1 will be taken equal to zero.

An equation of state can be readily obtained within the framework of the above model using the Maxwell relationship between the gas pressure p and the free energy F:

$$p = -\left(\frac{\partial F}{\partial V}\right)_T. \tag{6}$$

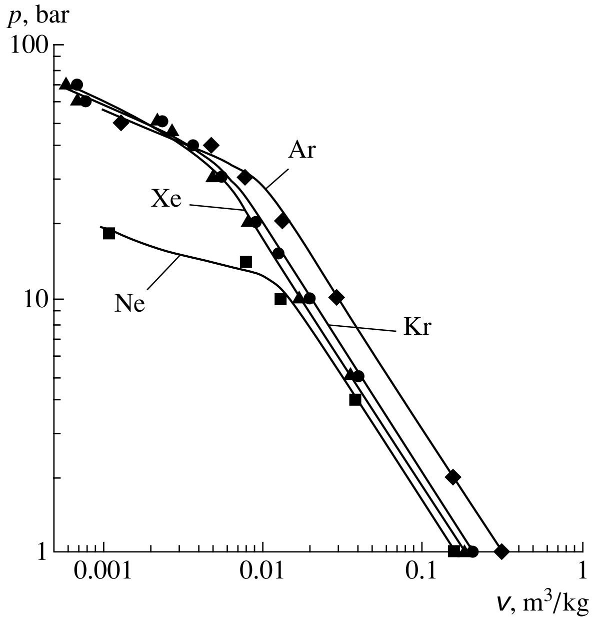

Fig. 1. Isotherms of inert gases: Ne ($T = 40$ K); Ar ($T = 150$ K); Kr ($T = 210$ K); Xe ($T = 290$ K); symbols represent the experimental data [10]; solid curves show the results of calculations [5].

In the case under consideration, $V = Nv_0$ (where v_0 is the minimum volume accommodating one particle). Differentiating the free energy with respect to N, we obtain

$$pv_0 = kT\frac{\sum N_i}{N}. \quad (7)$$

This equation of state coincides with that obtained by Mayer [2] and agrees with the Dalton law: the partial fractions are independent and inversely proportional to N.

The law of corresponding states. Proceeding from the dimensionality considerations, Smirnov [3] determined the coefficients which allow the pressure versus temperature relationship to be constructed in reduced coordinates. In these coordinates, the P–T curves of various inert gases virtually coincide.

Now we will demonstrate that the equation of state (7) is consistent with the law of corresponding states and the relationships for dimensionless thermodynamic parameters coincide with the results obtained in [3]. Assume that the free energy of a cluster can be expressed as [5]

$$g_i = -(h - sT)i + \sigma i^{2/3}, \quad i \gg 1, \quad (8)$$

where h is the enthalpy of bonds between neighboring particles, s is the vibrational entropy of particles in a cluster, and σ is the cluster surface energy per particle. As was demonstrated in [3], the surface energy parameter in a closely packed cluster is related (irrespective of the lattice type) to the enthalpy of bonds as $\sigma = 1.33h$.

Now let us consider the equation of state (7) for consistency with the law of corresponding states. According to formula (8) for the cluster energy, a relationship between the macroscopic parameters T, p, and v can be described by a system of equations

$$pv_0 = kT\left[\frac{N_1}{N} + \sum_{i \ge 2}\frac{1}{i!N^{i-1}}\exp\left\{-\frac{(h - sT)i - \sigma i^{2/3} + \lambda i}{kT}\right\}\right], \quad (9)$$

$$N_1 + \sum_{i \ge 2} i\frac{1}{i!N^{i-1}}\exp\left\{-\frac{(h - sT)i - \sigma i^{2/3} + \lambda i}{kT}\right\} = N'. \quad (10)$$

Passing from λ to a dimensionless variable y such that

$$y = \frac{1}{N}\exp\left\{-\frac{\lambda - sT}{kT}\right\}, \quad (11)$$

we can transform Eqs. (9) and (10) to

$$pv_0 = kT\left[y\exp\left\{-\frac{s}{k}\right\} + \sum_{i \ge 2}\frac{y^i}{i!}\exp\left\{-\frac{hi - \sigma i^{2/3}}{kT}\right\}\right], \quad (12)$$

$$y\exp\left\{-\frac{s}{k}\right\} + \sum_{i \ge 2}\frac{y^i}{(i-1)!}\exp\left\{-\frac{hi - \sigma i^{2/3}}{kT}\right\} = \frac{N'}{N}. \quad (13)$$

Introducing the parameter α such that $\sigma = \alpha h$ and using the dimensionless parameters $p^* = pv_0/h$, $T^* = kT/h$, and $n^* = N'/N$, we eventually obtain

$$p^* = T^*\left[y\exp\left\{-\frac{s}{k}\right\} + \sum_{i \ge 2}\frac{y^i}{i!}\exp\left\{-\frac{(i - \alpha i^{2/3})}{T^*}\right\}\right], \quad (14)$$

$$y\exp\left\{-\frac{s}{k}\right\} + \sum_{i \ge 2}\frac{y^i}{(i-1)!}\exp\left\{-\frac{(i - \alpha i^{2/3})}{T^*}\right\} = n^*. \quad (15)$$

The dimensionless macroparameters introduced according to the given model are fully analogous to the parameters derived proceeding from the dimensionality considerations in [3].

Thus, the only parameters characterizing a particular system are the entropy s and the ratio $\alpha = \sigma/h$ of the surface energy to the enthalpy of a particle in a cluster. However, as demonstrated in [3], the parameter α is constant and independent of the lattice type for closely packed clusters with the same character of interaction in the bulk and on the surface. As for the entropy s of a particle in the cluster, this parameter must be also identical in systems with a close character of interactions.

The latter conclusion can be illustrated as follows. Figure 1 presents the p–V isotherms calculated [5] using the above model. Data in the table show that the corresponding clusterization parameters agree well with the experimental data on the heat of evaporation (ε_{ev}) and with the results of quantum-mechanical calculations (ε_{quant}). As can be seen, the entropy of clusterization is very close for the four inert gases studied. Deviations from the mean value lead to an uncertainty below 10% in the pressure (for fixed n^* and T^*), which is a quite acceptable result.

It is possible to outline an analogy with the process of melting in solids. As is known, the entropy of melting for metals is virtually independent of the nature of a solid (the Compton–Richards rule) and amounts to approximately two entropy units [8]. Moreover, the entropies of melting S_{melt} for the crystals of elements representing groups possessing like electron structures [8, 9] are also quite close (see table). It is interesting to note that data on the entropy of melting are similar to the results of calculations of the entropy of clusterization (see table). On the one hand, this coincidence is accidental because the two quantities refer to different processes (melting of crystals versus evaporation of liquids) and, hence, cannot be compared. On the other hand, thermodynamic parameters of the crystal melting and liquid evaporation processes are related to the potential of interaction between particles and must reflect certain correlations. These relationships cannot be established within the framework of the model under consideration and we restrict this analysis to pointing out close coincidence of the entropies of clusterization and melting.

The above conclusions were verified in the case of inert gases, for which the p–V isotherms were constructed in dimensionless coordinates at nearly critical temperatures (for inert gases, $T^* \approx 0.167$ [3]). An exact equality is impossible since no detailed experimental data on the equation of state are available. For argon, krypton, and xenon, the experimental isotherms [10] were recalculated (using the parameters and densities in the liquid state from the table) by the formulas

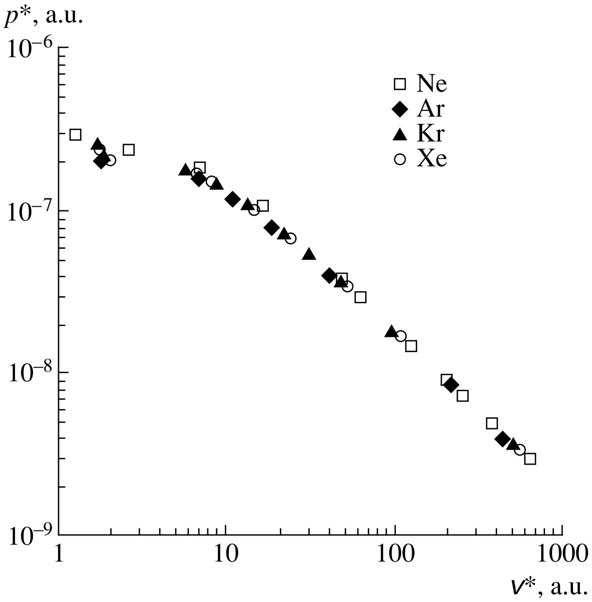

Fig. 2. Reduced logarithmic plots of the pressure p^* versus specific volume $V^* = 1/n^*$ for inert gases at temperatures in the vicinity of the critical point $T^* = 0.149$ (Ne), 0.154 (Ar), 0.161 (Kr), and 0.165 (Xe).

$$p^* = \frac{pA_r m_p}{h\rho_0}, \quad V^* = \rho_0 V, \tag{16}$$

where m_p is the proton mass, A_r is the relative atomic mass, and ρ_0 is the density of substances in the liquid state. For neon, the relationship was calculated using formulas (14) for parameters from the table.

Figure 2 shows the results of calculations plotted in the p^* versus V^* coordinates. As can be seen, the experimental data agree even in the region of small specific volumes, which is evidence of the validity of the conclusions derived in this study.

Thus, based on the above conclusions, we may ascertain that systems featuring the same character of interactions between particles must possess equal parameters s and α. Their states can be described by the same curve on the phase diagram constructed in reduced coordinates.

Calculated and experimental thermodynamic parameters of inert gases

Gas	h, meV	s, k	ε_{ev}, meV [3]	ε_{quant}, meV [6]	ρ_0, kg/m^3 [7]	T_{cr}, K [7]	S_{melt}, K [8]
Ne	23	–1.68	18	–	1247	44.5	1.64
Ar	75	–1.56	68	–	1400	150.7	1.69
Kr	100	–1.81	94	103	2413	209.4	1.70
Xe	135	–1.72	131	145	2987	289.7	1.71

Acknowledgments. This work was supported by the Russian Foundation for Basic Research, project no. 00-01-00209.

REFERENCES

1. L. D. Landau and E. M. Lifshitz, *Course of Theoretical Physics*, Vol. 5: *Statistical Physics* (Nauka, Moscow, 1964; Pergamon, Oxford, 1980).
2. A. Isihara, *Statistical Physics* (Academic, New York, 1971; Mir, Moscow, 1973).
3. B. M. Smirnov, Usp. Fiz. Nauk **162** (12), 97 (1992) [Sov. Phys. Usp. **35**, 1052 (1992)].
4. P. E. L’vov and V. V. Svetukhin, Khim. Fiz. **13** (2), 93 (1999).
5. P. E. L’vov and V. V. Svetukhin, Pis’ma Zh. Tekh. Fiz. **27** (5), 76 (2001) [Tech. Phys. Lett. **27**, 209 (2001)].
6. E. Miyoshi, Y. Sakai, K. Tanaka, and M. Masamura, J. Mol. Struct. **451**, 73 (1998).
7. *Handbook of Physical Quantities*, Ed. by I. S. Grigoriev and E. Z. Meilikhov (Énergoatomizdat, Moscow, 1991; CRC Press, Boca Raton, 1997).
8. A. A. Aĭvazov, V. M. Glazov, and A. R. Regel’, *Entropy of Melting of Metals and Semiconductors* (TsNII “Élektronika,” Moscow, 1978).
9. A. R. Regel’ and V. M. Glazov, *Periodic Regularities in the Physical Properties of Electronic Melts* (Nauka, Moscow, 1978).
10. *Thermal Properties of Neon, Argon, Krypton, and Xenon* (Moscow, 1976).

Translated by P. Pozdeev

Technical Physics Letters, Vol. 28, No. 6, 2002, pp. 525–526. Translated from Pis'ma v Zhurnal Tekhnicheskoĭ Fiziki, Vol. 28, No. 12, 2002, pp. 80–84.
Original Russian Text Copyright © 2002 by Pinchook, Shavrei.

A Correlation between the Microhardness and the Mobility of Twinning Dislocations in Bismuth Crystals Exposed to Constant Magnetic Field and Pulsed Electric Field

A. I. Pinchook* and S. D. Shavrei
Mozyr State Pedagogical Institute, Mozyr, Gomel oblast, Belarus
** e-mail: APinchook@yandex.ru*

Received January 25, 2002

Abstract—It is established that bismuth crystals under the simultaneous action of a constant magnetic field and current pulses exhibit a correlation between the microhardness and the mobility of twinning dislocations. It is shown that application of the external fields favors translation of the twinning dislocations along the twin–matrix boundaries. © *2002 MAIK “Nauka/Interperiodica”.*

Establishing correlations between the microhardness (H) and the mobility of dislocations in crystals under the action of external fields is of interest in the physics of microindentation processes and electroplastic deformation. The formation of an indenter impression is determined by the plastic deformation of a crystal in response to the concentrated load. In the case of bismuth crystals, the work of the load applied to the rod with an indenter is spent for the formation of both a dislocation rosette and a system of wedge-shaped twins around the impression.

Recently we reported [1] that the microhardness of bismuth crystals decreases under the action of a constant magnetic field and the electric current pulses. Previously [2] it was established that the length of wedge-shaped twins under these conditions significantly increases. Therefore, it was of interest to study a correlation between the microhardness and the mobility of twinning dislocations in bismuth.

It is known that the samples of bismuth with high hardness are characterized by a low mobility of dislocations [3]. However, in some cases, the decrease in microhardness is related to broadening of the dislocation rosette arms (i.e., to the dislocation spreading away from the narrow rows), rather than to an increase in the mobility of dislocations. The wedge-shaped twins formed in crystals of the bismuth type under the action of a concentrated load offer a good model object for studying this situation. All twinning dislocations in this system are localized at the twin–matrix interface.

The crystals of bismuth were grown by the Bridgman technique using a reagent grade initial material. The samples in the form of rectangular prisms with dimensions 10 × 5 × 5 mm were obtained by cleavage of the ingot. The wedge-shaped twins of the $\{110\}\langle 001\rangle$ system were produced by pressing with a standard diamond indenter on the (111) cleavage plane of the bismuth crystal sample. The microhardness was measured with the aid of a PMT-3 instrument equipped with a special device that ensured fixation of the sample in an external field. The experimental setup was described in detail elsewhere [4].

The configuration of external applied fields and concentrated load was as follows. First, the sample was exposed to a constant magnetic field ($B = 0.2$ T) and a concentrated load of $P = 0.14$ N was applied for 20 s. Then the current pulse was passed with a duration of $t_p = 4 \times 10^{-4}$ s and an amplitude of $j_p = 0$–50 A/mm^2. The vectors of load $\mathbf{P}$, current density $\mathbf{j}$, and magnetic induction $\mathbf{B}$ were mutually perpendicular. The $\mathbf{j}$ and $\mathbf{B}$ vectors lay in the (111) cleavage plane. The points on the experimental curves were obtained by averaging over the results of measurements of the dimensions of wedge-shaped twins formed around 20 impressions. The relative experimental error did not exceed 3%.

It was demonstrated in [3] that an adequate characteristic of mobility for the ensembles of dislocations is

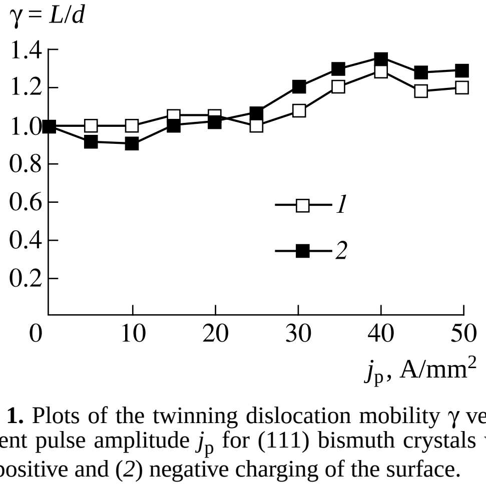

Fig. 1. Plots of the twinning dislocation mobility γ versus current pulse amplitude j_p for (111) bismuth crystals with (*1*) positive and (*2*) negative charging of the surface.

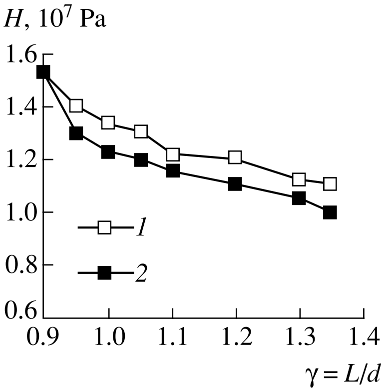

Fig. 2. Plots of the microhardness H versus mobility γ for (111) bismuth crystals with (*1*) positive and (*2*) negative charging of the surface.

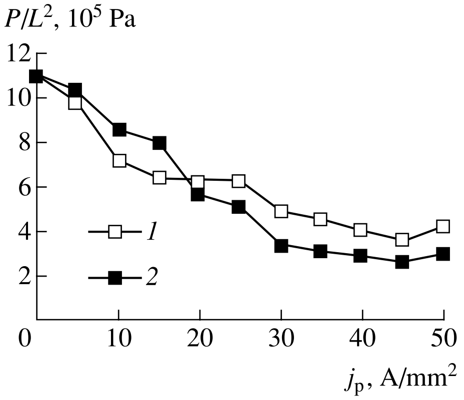

Fig. 3. Plots of the twinning dislocation start stress P/L^2 versus current pulse amplitude j_p for (111) bismuth crystals with (*1*) positive and (*2*) negative charging of the surface.

provided by the parameter $\gamma = L/d$, where L is the dislocation rosette arm length and d is the indenter impression size (rather than by the absolute L value). In our study, L is the wedge-shaped twin length.

As can be seen from the data presented in Fig. 1, the action of a constant magnetic field and pulsed current on the bismuth crystals increase mobility of the ensembles of twinning dislocations (in all figures, the open squares refer to the positive charge appearing on the (111) plane as a result of the Hall polarization, while black squares correspond to negative charging of the same crystal face).

In order to check for the existence of a correlation between H and γ values, we plotted the $H(\gamma)$ curves (Fig. 2). As can be seen from this figure, the increase in γ is accompanied by a significant decrease in the microhardness. An increase in the indenter impression size is probably related to the field-stimulated twinning effect.

The observed increase in plasticity of the bismuth crystals is accompanied by decreasing stresses corresponding to the start of twinning dislocations. It was pointed out [5] that the parameter P/L^2 has a dimension of stress and agrees in the order of magnitude with the twinning dislocation start stress. As can be seen from the behavior of curves presented in Fig. 3, the value of P/L^2 decreases with increasing amplitude of the current pulse j_p.

Thus, the results of our investigation showed that simultaneous action of the constant magnetic field and current pulses favors translation of the twinning dislocations along the twin–matrix boundary. This is accompanied by a correlation between microhardness and mobility of the twinning dislocations.

REFERENCES

1. A. I. Pinchuk and S. D. Shavrei, Fiz. Tverd. Tela (St. Petersburg) **43** (8), 1416 (2001) [Phys. Solid State **43**, 1476 (2001)].
2. V. S. Savenko, A. I. Pinchuk, V. V. Ponaryadov, and V. B. Zlotnik, Vestn. Beloruss. Gos. Univ., Ser. 1, No. 2, 27 (1995).
3. D. Z. Grabko, Yu. S. Boyarskaya, and M. P. Dyntu, *Mechanical Properties of Bismuth-Like Semimetals* (Shtiintsa, Kishinev, 1982).
4. A. I. Pinchook and V. S. Savenko, J. Appl. Phys. **86** (5), 2479 (1999).
5. V. I. Bashmakov and V. S. Savenko, Izv. Vyssh. Uchebn. Zaved., Fiz., No. 7, 29 (1980).

Translated by P. Pozdeev

Technical Physics Letters, Vol. 28, No. 6, 2002, pp. 527–529. Translated from Pis’ma v Zhurnal Tekhnicheskoĭ Fiziki, Vol. 28, No. 12, 2002, pp. 85–90.
Original Russian Text Copyright © 2002 by Kraak, Minina, Savin, Ilievsky, Sorenson.

Positive Delayed Photoconductivity in Double Heterostructures $Al_{0.5}Ga_{0.5}As/GaAs/Al_{0.5}Ga_{0.5}As$ of the *p*-Type

W. Kraak, N. Ya. Minina*, A. M. Savin, A. A. Ilievsky, and K. B. Sorenson
Moscow State University, Moscow, 119899 Russia
** e-mail: min@mig.phys.msu.su*

Received November 8, 2001

Abstract—Positive delayed photoconductivity was observed for the first time in double *p*-type heterostructures $Al_{0.5}Ga_{0.5}As/GaAs/Al_{0.5}Ga_{0.5}As$ upon exposure to the radiation of a red light-emitting diode. In this state, the concentration and mobility of two-dimensional holes are increased 1.5 and 1.7 times, respectively, as compared to the initial dark values. The delayed photoconductivity can be explained by the presence of deep electron traps located above the Fermi level at the inverted heterointerface. © *2002 MAIK “Nauka/Interperiodica”.*

Previously, Chou *et al.* [1] reported that exposure of a single *p*-type heterojunction $GaAs/Al_{0.5}Ga_{0.5}As$ to the radiation of a red light-emitting diode (LED) at liquid helium temperature gives rise to a negative photoconductivity (NPC), which exhibited a slow relaxation to the initial dark level upon switching off the LED.

Here we report for the first time on the phenomenon of positive delayed photoconductivity (PPC) observed in double *p*-type heterostructures $Al_{0.5}Ga_{0.5}As/GaAs/Al_{0.5}Ga_{0.5}As$, which differ from the structure described in [1] by the presence of a second (inverse) heterojunction. Investigations of the GaAs/AlAs superlattices revealed intriguing differences between the electronic properties of normal (AlGaAs on GaAs) and inverse (GaAs on AlGaAs) heterojunctions. This difference is attributed to the segregation of impurities at the interface and to the appearance of intrinsic defects during growth near the inverted heterointerface [2, 3]. To our knowledge, the possible influence of such defects on the photoconductivity and related transient processes was not studied so far.

The samples of a double *p*-type heterostructure $Al_{0.5}Ga_{0.5}As/GaAs/Al_{0.5}Ga_{0.5}As$ were grown by MBE in the [001] direction and modulation doped with Be to a concentration of 2×10^{24} m^{-3} in a 100-Å-thick active AlGaAs layers on both sides of the GaAs quantum well. The samples had a rectangular shape with a surface mesastructure of the Hall bar configuration formed by photolithography. The dark concentration of two-dimensional (2D) holes at $T = 1.5$ K was $N = 2.7 \times 10^{15}$ m^{-2}, and the dark carrier mobility was $\mu = 7.0$ m^2/(V s). The photoconductivity was excited by a red LED with a photon energy of $h\nu = 1.9$ eV.

The 2D hole concentration during the transient process was calculated using the results of measurements of the Hall effect. In addition, the hole concentration in both initial (dark) and PPC states was determined by measuring the Shubnikov–de Haas oscillations and the quantum Hall effect. Coincidence (to within 2%) of the data obtained from measurements of the Hall effect and from observations of the quantum effects indicates that the PPC is not related to the parallel conductivity reported in [4].

Upon illumination with a red LED (Fig. 1, point *1*), the samples of $Al_{0.5}Ga_{0.5}As/GaAs/Al_{0.5}Ga_{0.5}As$ passed into an NPC state analogous to that described in [1] for a single normal heterointerface. However, a transient process observed after switching off the LED (point *2*) converted the double heterostructure into a PPC state, rather than into the initial dark state as in [1]. In the PPC state, the 2D hole concentration and mobility were greater by factors of 1.5 and 1.7, respectively, than the corresponding dark values. The initial state could be restored by heating the samples from liquid helium to room temperature, followed by cooling to 1.5 K.

The transient process from NPC to PPC state is nonexponential and well obeys the logarithmic relationship [1]:

$$\frac{1}{R} = \frac{1}{R_0} + \Delta\sigma\left[\ln\left(\frac{t-t_0}{\tau}+1\right)\right]^{\gamma}, \qquad (1)$$

where R is a current resistance of the sample, R_0 is the resistance at the time instant ($t = t_0$) of switching off the LED, $\Delta\sigma$ is the amplitude factor, and τ is the relaxation time constant. In Fig. 1, the open circles show the results of fitting with the parameters $1/R_0 = 0.495$ kΩ^{-1}, $\Delta\sigma = 0.509$ kΩ^{-1}, $\tau = 6$ s, and $\gamma = 0.51$.

Since the energy of the LED radiation quantum is 1.9 eV, while the bandgap of $Al_{0.5}Ga_{0.5}As$ at 4.2 K is 2.14 eV, direct transitions from the valence to conduction band are impossible. Following [1], we suggest

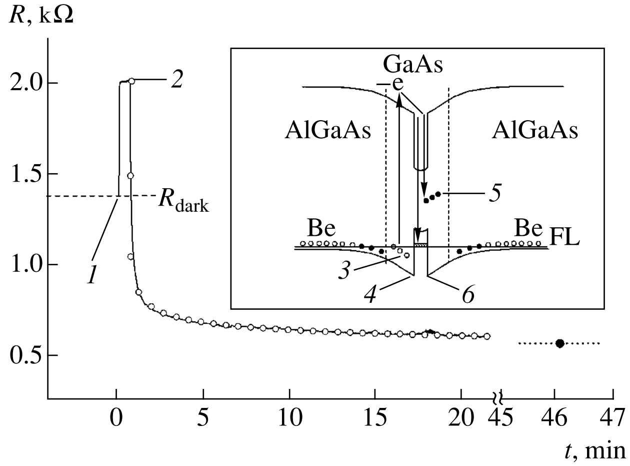

Fig. 1. NPC and PPC effects (solid curve) in a double *p*-type heterostructure $Al_{0.5}Ga_{0.5}As/GaAs/Al_{0.5}Ga_{0.5}As$ upon exposure to the radiation of a red LED; dashed line shows the dark resistance level; open circles show the results of fitting theory to experiment; the black point shows the resistance 45 min after switching off the LED. The inset shows a schematic energy level diagram illustrating the course of processes under illumination (see the text for explanations).

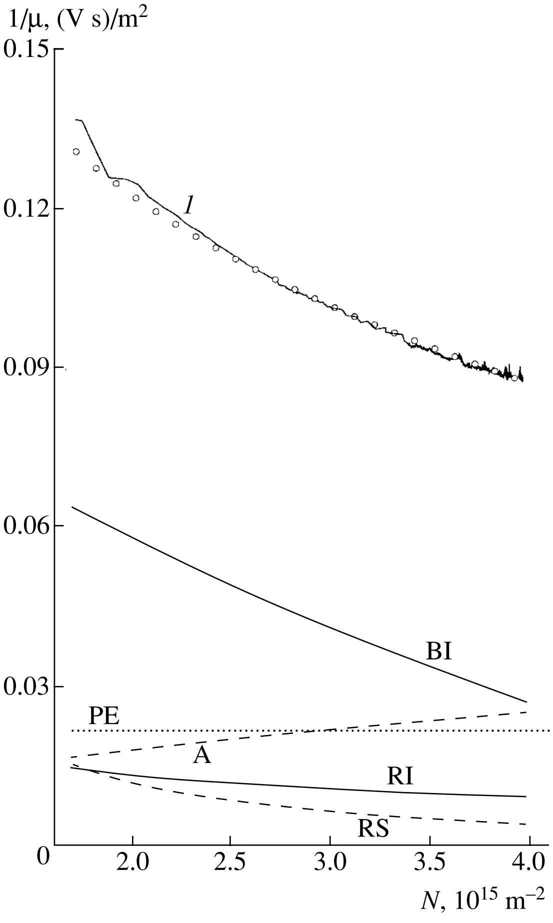

Fig. 2. The contributions of various scattering mechanisms (indicated by arrows) to the experimental inverse mobility $1/\mu(N)$ (curve *1*) measured during the transition from NPC to PPC state. Open circles show the results of calculations (see the text for explanations).

that neutral donorlike levels (*3* on the inset in Fig. 1) can exist slightly above the Fermi level (FL) at the normal heterointerface *4* of the system studied. Excited from these levels to the conduction band under the action of the electric field operating at the heterojunction, electrons fall into the GaAs quantum well and recombine with 2D holes, thus decreasing the hole concentration. When the LED is switched off, a relaxation process takes place due to the holes tunneling back to the quantum well from excited donorlike levels at the normal heterointerface.

As noted above, the PPC state in the double heterostructure studied is characterized by a greater 2D hole concentration as compared to that in the initial (dark) state. Since the double *p*-type heterostructures $Al_{0.5}Ga_{0.5}As/GaAs/Al_{0.5}Ga_{0.5}As$ differ from a single p-$GaAs/Al_{0.5}Ga_{0.5}As$ interface by the presence of the inverted junction, we may suggest that a certain amount of electrons are captured by the traps (*5* on the inset in Fig. 1) localized at the inverted heterointerface *6* situated above the Fermi level. Assuming (as in [1]) that all holes from the excited donorlike levels return to the quantum well and adopting the charge conservation condition, we conclude that the total concentration of 2D holes in the PPC state must be higher as compared to the dark level.

According to the deep-level transient spectroscopy data of Krispin *et al.* [3], there is a series of four deep levels acting as electron traps in the inverted *n*-type heterointerface $GaAs/Al_xGa_{1-x}As$ grown by MBE. Since the appearance of electron traps described in [3] is not related to the presence or absence of impurities in AlGaAs (the concentration of traps depends only on the concentration of aluminum and on the growth conditions), we may suggest that such defects exist in p-$Al_xGa_{1-x}As$ as well and account for the PPC effect.

Once the 2D hole concentration and mobility in the quantum well at any time instant are known, we can estimate the contributions of various scattering mechanisms to the mobility. According to the Matthiessen rule, the total mobility is

$$1/\mu = 1/\mu_{\text{RI}} + 1/\mu_{\text{BI}} + 1/\mu_{\text{A}} + 1/\mu_{\text{RS}} + 1/\mu_{\text{PE}}, \qquad (2)$$

where μ_{RI}, μ_{BI}, μ_{A}, μ_{RS}, and μ_{PE} are the mobility contributions related to the scattering on remote impurities, background impurities, acoustic phonons, and surface roughness and to the piezoelectric scattering, respectively. The μ_{RS} value was calculated according to [5], while the other scattering mechanisms were described using the approach developed in [6] for a 2D electron gas at low temperatures.

It was found that variation of the hole concentration *N* and mobility μ during the transition from an NPC to PPC state (Fig. 2) can be adequately described assuming that (i) a certain amount of electrons are captured during exposure to the LED radiation by the traps localized at the inverted heterointerface and (ii) the concentration of 2D carriers in the quantum well increases during the transient process due to the holes tunneling from donorlike levels at the normal heterointerface. The results of calculation of the total inverse mobility $1/\mu(N)$ for the transient process are depicted in Fig. 2 (open circles) together with contributions of the partial scattering mechanisms to the total experimental $1/\mu$ value. As can be seen, the background impurity (surface charge) is the main scattering factor at the heterojunction.

It should be noted that the background impurity (surface charge) concentration N_{BI} in the PPC state is 2.4 times as small as the dark value, which qualitatively agrees with the assumption concerning the capture of electrons by deep traps during exposure to the LED radiation.

Acknowledgments. The authors are grateful to Dr. H. Kostial for his interest in this study and useful remarks.

The study was supported by the Russian foundation for Basic Research, project nos. 01-02-17786 and 00-15-96784.

REFERENCES

1. M. J. Chou, D. C. Tsui, and G. Weimann, Appl. Phys. Lett. **47**, 609 (1985).
2. L. Pfeiffer, E. F. Schubert, K. W. West, *et al.*, Appl. Phys. Lett. **58** (20), 2258 (1991).
3. P. Krispin, R. Hey, and H. Kostial, J. Appl. Phys. **77**, 5773 (1995).
4. R. M. Kusters, T. J. B. M. Janssen, C. G. M. Langerak, *et al.*, Semicond. Sci. Technol. **7**, 961 (1992).
5. H. Sakaki, T. Noda, K. Hirakawa, *et al.*, Appl. Phys. Lett. **51**, 1934 (1987).
6. K. Lee, M. S. Shur, T. J. Drummond, *et al.*, J. Appl. Phys. **54**, 6432 (1983).

Translated by P. Pozdeev

Technical Physics Letters, Vol. 28, No. 6, 2002, pp. 530–531. Translated from Pis'ma v Zhurnal Tekhnicheskoĭ Fiziki, Vol. 28, No. 12, 2002, pp. 91–94.
Original Russian Text Copyright © 2002 by Grigor'ev.

The Equilibrium Shape of a Charged Drop in Parallel Electrostatic and Aerodynamic Fields

A. I. Grigor'ev
Yaroslavl State University, Yaroslavl, Russia
e-mail: grig@uniyar.ac.ru

Received February 1, 2002

Abstract—An analytical expression describing equilibrium spheroidal deformation of a charged drop exposed to parallel aerodynamic and electrostatic fields is derived based on the principle of minimum potential energy of a closed system in the equilibrium state. The expression relates eccentricity of the spheroid to the electrostatic field strength and the streamlining flow velocity. © *2002 MAIK "Nauka/Interperiodica".*

The study of deformation and stability of liquid drops in external fields (electric, gravitational, aerodynamic) is of considerable interest from the standpoint of numerous applications in geophysics, technical physics, scientific instrument building, and various technologies (see, e.g. [1] and references therein). As is known [1–3], a liquid drop exposed to a homogeneous electrostatic field deforms so that its shape resembles a spheroid elongated in the field direction. At the same time, a laminar gas flow streamlining such a drop would make it oblate in the flow direction. Indeed, according to the Bernoulli equation, the pressure drop caused by the flow streamlining a spherical surface is maximum near the equatorial cross section.

Not dwelling on the interplay of the two opposite trends, let us consider the role of intrinsic charge of a liquid drop in the process of deformation in electrostatic and aerodynamic fields. In the presence of an electrostatic field only, the charge enhances deformation of the drop [3]. The effect of a charge on the drop deformation in a streamlining flow has not been studied so far.

Formulation and solution of the problem. Let a spherical drop of incompressible liquid with a radius R possessing a charge Q and a surface tension σ be exposed to a homogeneous electrostatic field $\mathbf{E}_0$ and streamlined by the laminar flow of a gas with a density ρ and a velocity $\mathbf{U} \parallel \mathbf{E}_0$. The field deforms the drop into an elongated spheroid, whereas the gas flow tends to render the spheroid oblate. We assume that the ratio of the E_0 and U values is such that the former trend dominates and the drop has the shape of an elongated spheroid with an eccentricity e. Let us evaluate the contributions of E_0, U, and Q to the equilibrium eccentricity value. The analysis will be performed in a spherical coordinate system with the origin at the drop center.

An expression for the total potential energy of the drop includes contributions due to the surface tension [3]

$$U_\sigma = 2\pi R^2 \sigma (1-e^2)^{1/3}\left(1 + e^{-1}(1-e^2)^{-1/2}\arcsin e\right);$$

the intrinsic charge energy [4]

$$U_q = \frac{Q^2}{2R} e^{-1}(1-e^2)^{1/3}\operatorname{arctanh} e;$$

the energy of polarization in the field $\mathbf{E}_0$ [4]

$$U_E = -\frac{1}{6}E_0^2 R^3 \frac{e^3}{(1-e^2)(\operatorname{arctanh} e - e)};$$

and the energy in the aerodynamic flow

$$U_U = -\int p_U(\theta) r^2 \cos^{-2}\gamma \sin\theta \, d\theta \, d\varphi \, dr,$$

where p_U is the aerodynamic pressure on the surface of the elongated spheroid [5]:

$$p_U = \frac{\rho U^2}{2}(1-0.5C_0)^{-2}\frac{\sin^2\theta}{[1-e^2(2-e^2)\cos^2\theta]};$$

$$C_0 \equiv 2e^{-3}(1-e^2)(\operatorname{arctanh} e - e).$$

In the above equations, the angle θ is measured relative to the $\mathbf{E}_0$ direction; $\cos\gamma$ is the cosine of the angle between the normal to the drop surface and the radial unity vector $\mathbf{n}_r$ of the spherical coordinate system; the integration with respect to R is performed from zero to the surface of the elongated spheroid:

$$r(\theta) = R(1-e^2)^{1/3}(1-e^2\sin^2\theta)^{-1/2}.$$

The expression for U_U is obtained by integrating (over the same spheroidal surface) the work of the force $p_U dS$ acting upon the elementary surface area $dS \equiv r^2 \sin\theta \, d\theta \, d\varphi / \cos\gamma$ and shifting this area along the normal by $dn \equiv dr/\cos\gamma$.

1063-7850/02/2806-0530$22.00 © 2002 MAIK "Nauka/Interperiodica"

Using the principle of minimum potential energy of a closed system in the equilibrium state (the system under consideration is closed at a large distance from the drop) and equating to zero the derivative of the total potential energy with respect to eccentricity, we obtain an expression for the square eccentricity minimizing the potential energy:

$$e^2 = \frac{9}{16}\frac{(w\pi^{-1} - We)}{(1 - W)};$$

$$w \equiv E_0^2 R\sigma^{-1}; \quad We \equiv \rho U^2 R\sigma^{-1}; \quad W \equiv Q^2/16\pi\sigma R^3.$$

As can be seen, the square of the eccentricity is negative for $E_0 = 0$. This corresponds to the drop being oblate in the flow direction. In this situation, as well as in the case of $U = 0$ and $E_0 \neq 0$, the intrinsic charge increases the degree of deformation. For $U = 0$, $E_0 = 0$, and $Q \neq 0$, the drop is undeformed. Thus, the intrinsic charge of a liquid drop, while not inducing deformation of the drop by itself, enhances equilibrium deformation of the drop in an external force field.

In the general case of $Q \neq 0$, $E_0 \neq 0$, and $U \neq 0$, when a drop with nonzero charge moves in an external electric field at a finite velocity (sufficiently small to ensure a laminar character of the gas flow streamlining the drop surface), the drop can retain a spherical shape for $w/\pi = We$ and an arbitrary charge (below the critical Rayleigh charge [1]). For $w/\pi > We$, the drop deforms to acquire an elongated shape, while for $w/\pi < We$ the spheroid becomes oblate. Observations under the conditions of a stormy cloud reveal drops of all the three possible types, including spheres and elongated and oblate spheroids [6].

Conclusion. A liquid drop in a laminar flow of an ideal incompressible fluid streamlining the surface tends to become an oblate spheroid with the symmetry axis parallel to the flow direction. The presence of an intrinsic electric charge renders the drop more oblate (increases the eccentricity). Exposed to a homogeneous electrostatic field (without a streamlining fluid flow), the liquid drop deforms to become the elongated spheroid and the intrinsic charge increases the degree of elongation as well. In the presence of both external factors, there is a competition between the trends of flattening in the hydrodynamic flow and elongating in the electrostatic field. At a certain ratio of the electrostatic field strength and flow velocity, the drop may retain a spherical shape.

REFERENCES

1. A. I. Grigor’ev and S. O. Shiryaeva, Izv. Akad. Nauk, Mekh. Zhidk. Gaza, No. 3, 3 (1994).
2. G. Taylor, Proc. R. Soc. London, Ser. A **280**, 383 (1964).
3. A. I. Grigor’ev, S. O. Shiryaeva, and E. I. Belavina, Zh. Tekh. Fiz. **59** (6), 27 (1989) [Sov. Phys. Tech. Phys. **34**, 602 (1989)].
4. L. D. Landau and E. M. Lifshitz, *Course of Theoretical Physics*, Vol. 8: *Electrodynamics of Continuous Media* (Nauka, Moscow, 1982; Pergamon, New York, 1984).
5. N. E. Kochin, I. A. Kibel’, and N. V. Roze, *Theoretical Hydromechanics* (Fizmatgiz, Moscow, 1963), Part 1.
6. D. M. Jones, J. Meteorol. **16** (5), 504 (1959).

Translated by P. Pozdeev